Ion Transport Properties in Novel and Traditional Liquid Electrolytes for Lithium-Based Batteries

By

Deep B. Shah

A dissertation submitted in partial satisfaction of the

requirements for the degree of

Doctor of Philosophy

in

Chemical Engineering

in the

Graduate Division

of the

University of California, Berkeley

Committee in charge:

Professor Nitash P. Balsara, Chair
Professor Bryan D. McCloskey
Professor Gerbrand Ceder

Summer 2020

Ion Transport Properties in Novel and Traditional Liquid Electrolytes for Lithium-Based Batteries

Abstract

Ion Transport Properties in Novel and Traditional Liquid Electrolytes for Lithium-Based Batteries

By

Deep B. Shah

Doctor of Philosophy in Chemical Engineering

University of California, Berkeley

Professor Nitash P. Balsara, Chair

Enabling next-generation lithium-based batteries is of paramount importance for the transportation sector. The energy density, cycle life, and safety are all prime considerations for electric vehicles. In addition, these batteries must be able to operate in a wide variety of temperatures and a range of power requirements. The electrolyte is fundamental to the ion transport within a battery, is a constraint on the operational voltage of a cell, and is integral to the safety of a device. Limitations on power delivered by a battery are specifically due to ion transport within the electrolyte and these properties are often not well understood within conventional and novel electrolytes. In this work, we measure ion transport properties in a variety of nonaqueous liquid electrolytes utilizing Newman's concentrated solution theory. We then use these properties to predict lithium-symmetric cell behavior and compare theoretical predictions to experimental results without the use of any adjustable parameters.

Mixtures of perfluoropolyethers (PFPE) and lithium salts with fluorinated anions are a new class of electrolytes for lithium batteries. Unlike conventional electrolytes wherein electron-donating oxygen groups interact primarily with the lithium cations, the properties of PFPE-based electrolytes appear to be dependent on interactions between the fluorinated anions and the fluorinated backbones. We study these interactions by examining a family of lithium salts wherein the size of the fluorinated anion is systematically increased: lithium bis(fluorosulfonyl)imide (LiFSI), bis(trifluoromethanesulfonyl)imide (LiTFSI) salts and lithium bis(pentafluoroethanesulfonyl)imide (LiBETI). Two short chain perfluoroethers (PFE), one with three repeat units, C6-DMC, and another with four repeat units, C8-DMC were studied; both systems have dimethyl carbonate end groups. We find that LiFSI provides the highest conductivity in both C6-DMC and C8-DMC. These systems also present the lowest interfacial resistance against lithium metal electrodes. The ideal transference number ($t_{+,id}$) was above 0.6 for all of the electrolytes and was an increasing function of anion size. The product of conductivity and the steady-state transference number is a convenient measure of the efficacy of the electrolytes for lithium battery applications. Amongst the systems studied, LiFSI/PFE mixtures were the most efficacious electrolytes.

The performance of binary electrolytes is governed by three transport properties: conductivity, salt diffusion coefficient, and transference number. Rigorous methods for measuring conductivity and the salt diffusion coefficient are well established and used routinely in the literature. The commonly used methods for measuring transference number are the steady-state current method, $t_{+,id}$, and pulsed field gradient NMR, $t_{+,NMR}$. These methods yield the transference number only if the electrolyte is ideal, i.e., the salt dissociates completely into non-interacting anions and cations. In this work, we present a complete set of ion transport properties for mixtures of a functionalized perfluoroether, dimethyl carbonate terminated perfluorinated tetraethylene ether, and lithium bis(fluorosulfonyl)imide (LiFSI). The equations used to determine these properties from experimental data are based on Newman's concentrated solution theory. The concentrated-solution-theory-based transference number, t_+^0, is negative across all salt concentrations, and it increases with increasing salt concentration. In contrast, the ideal transference number, $t_{+,id}$, is positive across all salt concentrations and it decreases with salt concentration. The NMR-based transference number, $t_{+,NMR}$, is approximately 0.5, independent of salt concentration. The disparity between the three transference numbers, which indicates the dominance of ion clustering, is resolved by the use of Newman's concentrated solution theory.

Imposing a steady ionic current through an electrolyte results in the formation of salt concentration gradients that compromise battery performance. The limiting current is usually defined as the current at which the salt concentration at the cathode approaches zero. Higher currents cannot be imposed on the cell as larger concentration gradients are unsustainable. We study the limiting current in electrolytes comprising a perfluorinated oligomer, C8-DMC, and lithium bis(fluorosulfonyl)imide salt in symmetric lithium cells. The time-dependence of the potential, which increases as salt concentration gradients develop, was also measured. Both steady-state and transient behaviors are modeled using Newman's concentrated solution theory; transport and thermodynamic parameters needed to perform the calculations were measured independently. The limiting current is a non-monotonic function of salt concentration in both theory and experiment. The model shows that at low salt concentrations (below 0.88 mol/kg solvent), the concentration at the cathode approaches zero at limiting current. In contrast, at high salt concentrations (above 0.88 mol/kg solvent), the concentration at the anode approaches the solubility limit (2.03 mol/kg solvent). The experimentally determined salt concentration at which the limiting current is maximized is in excellent agreement with theoretical predictions made without resorting to any adjustable parameters.

We apply concentrated solution theory to measure a complete set of ion transport properties to mixtures of low molecular weight poly(ethylene oxide), tetraglyme, and LiTFSI at T = 30 °C and 90 °C. We found that while conductivity and the salt diffusion coefficient are lower at 30 °C compared to 90 °C, the ideal transference number is greater at all salt concentrations. The rigorously defined transference number is lower at 90 °C than at 30 °C for most concentrations, except for in the limit of large concentrations. We use the measured properties at 90 °C to predict the limiting current of mixtures of LiTFSI/tetraglyme and compare those results to experimental behavior in lithium symmetric cells. We posit that the lack of qualitative agreement at high starting salt concentrations is due to solubility constraints at the anode surface.

Carbonate electrolytes are often used in commercial lithium-ion batteries, however their transport properties are not well understood. We apply concentrated solution theory to study

mixtures of LiFSI/PC and lithium hexafluorophosphate ($LiPF_6$)/PC over a wide range of salt concentrations at room temperature. We find that while the conductivity and salt diffusion coefficient for both mixtures are similar for all salt concentration, the ideal transference number is greater for mixtures of LiFSI/PC compared to mixtures of $LiPF_6$/PC at all concentrations. The rigorously defined transference number for mixtures of LiFSI/PC is also found to be greater than that of mixtures of $LiPF_6$/PC at all salt concentrations. We use the measured transport properties for mixtures of LiFSI/PC and use them to predict the electrolyte potential drop within a lithium symmetric cell. We find that there is good qualitative agreement between the measured experimental drop and theoretical predictions as a function of applied current density and salt concentration. Both the model and experimental results predict that the largest potential drop within mixtures of LiFSI/PC occurs at a concentration of 1 M, which is when conductivity is also maximized.

“Preserve and cherish the pale blue dot, the only home we’ve ever known.”

- Carl Sagan

Table of Contents

List of Figures

List of Schemes

List of Tables

Acknowledgements

First and foremost, I want to thank my fantastic advisor, Nitash Balsara. This dissertation would not have been possible without your guidance and optimism. Your drive to fundamentally understand science, and particularly ion transport and polymer thermodynamics, is incredibly contagious. Your continuous support, and sometimes gentle nudges, have given me all the tools I have needed to learn and to grow into an independent researcher. You have created a research group that is tightknit, productive, and fun, and I am eternally grateful to you for bringing me into your group. I cannot imagine a better place to have spent these last five years as a graduate student.

I am grateful to my dissertation committee, Bryan McCloskey and Gerd Ceder, for reading through this work and for providing crucial feedback during my candidacy exam. Thank you to Kranthi Mandadapu for allowing me to GSI for your transport phenomena class. I learned a great deal working with you; your love for teaching is evident in the way you hold lectures, and it pushed me to be a better teacher.

The Balsara Lab was integral to my growth as a graduate student. I am especially indebted to the senior post-docs and graduate students that taught me how to be successful in graduate school. Dr. Didier Devaux was a font of battery knowledge and I am incredibly grateful that he took me under his wing and taught me battery basics my first year. Your incredible passion for electrochemistry was contagious, and I know you will continue to inspire students in your own research group. Dr. Irune Villaluenga is one of the most creative people I know when it comes to chemical synthesis. Thank you for helping me synthesize the materials that were used in Chapters 2 – 4 of this work, even while doing a million other things. I am thankful to Dr. Mahesh Bhatt for acting as a sounding board for scientific ideas. Dr. Chelsea Chen always asked great scientific questions, and I am thankful to her for providing good feedback on my early work. Dr. Hee Jeung Oh, the work ethic that you display is unparalleled and I am continuously in awe of you. You are always willing to learn something new, to share your knowledge, and to help anyone within the group, thank you. I know you will lead your own research group at Penn State phenomenally.

The older graduate students set an example for how to conduct stellar work as well as have fun in graduate school. Jacob Thelen's photography skills are sorely missed, and the number of projects he affected was impressive. Kevin Wujick, you were a pioneer in the group in terms of XAS. I have always been impressed with the level of rigor you were able to bring to understanding lithium-sulfur battery chemistry. Your softball abilities were impressive and I wish I could hit a home run like you. Thank you for all of the career advice you have provided over the past year as I transition to the working world. Katherine Harry, your ability to communicate science and the systematic way in which you approached your work was impressive. Once you graduated, our lab's musical group took a turn for the worse as no one could sing quite like you. Chaeyoung Shin is a brilliant researcher and has an incredibly warm personality. Thank you for helping me feel at home in the Balsara Lab when I first joined and for providing career and life advice in the years that followed. Mahati Chintapalli inspired me with her work on fluorinated electrolytes and ultimately led me to following in her footsteps. She always asked critical questions, never wavered in her support of us younger students, and was quite the mycophile.

Adriana Rojas delved into the realm of single-ion conductors, synthesized an impressive library of materials, and set a lab safety standard that carries on to this day. Her freshly baked goodies are missed at group meetings. Alex Wang was steadfast in his work on pervaporation and I will always remember building dozens of snowmen to block in a driveway during our lab ski trip. Doug Greer is forever an enigma in the best possible way. You are a great scientist, musician, water polo athlete, swimmer, and board game player.

I learned a great deal from the graduate students right above me. Danielle Pesko set the groundwork on full ion transport characterization within our lab. Danielle, your competitive attitude in all things is something I miss dearly, almost as much as my footraces with your dog, Piper. While I do not mention my work with Rita Wang on XAS of lithium polysulfides in this dissertation, I spent a great deal of time working with her at various beamlines. I always appreciated her company and fun loving attitude. The more I learn about Ksenia Timachova, the more blown away I am as to the kind of person she is. Not only did you, Ksenia, add a research direction to our group in the form of NMR, you are a phenomenal skier, an avid backpacker, a fantastic teacher, a budding beer brewer and beer lover, and an even better friend. I really enjoyed my time working with Dr. Kim Mongcopa, who was as easy talking to about life as she was discussing neutrons. Every boba tea trip was an adventure with you.

I cannot begin to express my gratitude for working with Jackie Maslyn and Whitney Loo over the last five years. While our projects were quite different, the two of you were a perennial source of support and inspiration. I am so thankful that we have only gotten closer over the course of graduate school. Jackie, you are amongst the most careful of researchers and writers that I have ever had the pleasure of meeting. I adore our various competitive endeavors, including Insanity at 8 am at LBL, a ridiculously difficult core training class, and snowball fights during a hike. I still maintain that you started most of those snowball fights and I was pulled in as an innocent bystander… Whitney, you are a go-getter when it comes to research, EDM, and biking. While I do not share the same level of love for polymer thermodynamics as you do, I do enjoy the non-stop and quality suggestions for new EDM artists and exploring the Bay on our bikes. Also, please stop falling off your bike – I would like to see you for years to come… I cannot wait to watch both of your careers blossom and am ecstatic to celebrate every moment along the way. Let us never lose touch and I know we will continue to push each other to be better scientists and, more importantly, friends.

Mike Galluzo and Gumi Sethi both reinvigorated our lab upon their arrival. Mike has an unstoppable drive to answer unsolved research questions and is a brilliant skier (sometimes to his own detriment). Gumi has made amazing progress on her PEO-POSS project and is a perennial source of energy. Both Mike and Gumi are great supports with whom I could always depend on to talk about the ups and downs of both research and life. Dr. Louise Frenck is a constant source of optimism, delicious baked goods, and dendrite knowledge. Louise, you have done an amazing job in reinstating lab happy hours, which I can never turn down. Drs. David Halat and Youngwoo Choo have a love for science that is contagious, and I am looking forward to the level of insight they are bringing to the electrolyte community. Dr. Saheli Chakraborty is a magician when it comes to polymer synthesis and I am constantly in awe with the speed at which she solves synthesis problems.

Working, running, exercising, and talking science with Kevin Gao has always been an adventure, Kevin, you have been a good friend over the past three years. You approach all things in life with a level of intensity that I hope to emulate in my own endeavors. I am incredibly happy that Lorena Grundy choose to join our lab, but that may be due to her being the only other person in the Balsara Lab to love the Buckeyes as much as I do. I admire the way in which you teach, both our lab about NMR (because quantum physics is hard) and the students in your classes.

Zach Hoffman, Alec Ho, and Neel Shah have all made amazing progress on their respective projects. Zach, you have become a great concentration cell maker, an even better friend, and have a laugh that may rival my own. Alec, you are quickly becoming a tomogram expert, mediocre at beach volleyball, and you have a voice that is indistinguishable from sarcasm (color me impressed for the latter). I am looking forward to watching our unique relationship evolve. The tenacity with which Neel has approached his PMMA project has been impressive. I know you will approach your new hobby, biking, in a similar manner.

The way in which our newest members, Darby Hickson, Morgan Seidler, and Dr. Xiaopeng Yu have handled joining our group, in the midst of a global pandemic, has been truly extraordinary. All three of you have found ways to stay engaged, even in the absence of a physical lab, and that is to be commended.

I have had the pleasure of mentoring two undergraduate students, Adar Karny, and Hien Nguyen. Adar was instrumental to Chapter 2 of this dissertation and Hien was to Chapters 3 – 5. I am grateful to all the time both of you spent with me, and I learned a great deal from the both of you. Adar, you approached your project with a great deal of enthusiasm and always asked critical questions in and out of group meetings. Hien, you have one of the best work ethics I have ever been privy to, and made an amazing amount of progress on your independent project. I look forward to witnessing the growth of your careers.

My collaborators have taught me a great deal. Thank you to Dr. Kevin Olson, Dr. Sue Mecham, and Prof. Joseph DeSimmone for providing me the fluorinated materials to get started. Kevin, you are insightful and a great teacher. Thank you for being so patient and detailed with me as I learned the fluorinated synthesis from you. Without Dr. Hong Keun Kim and Dr. Venkat Srinivasan, we would not have been able to predict the transient potential behavior shown in Chapter 4.

My time at Berkeley would have been much less exciting and less thought-provoking if it were not for the graduate student organization, Berkeley Energy and Resources Collaborative. I am especially grateful to the team I had a chance to work with over the last year, Joyce Yao, Amaani Hamid, Alex Brown, Tommy Larson, Paula Moren, Kate Tomlinson, and David Nenon. I admire the level of intensity and passion each of you bring to the energy and resources space.

Graduate school can be grueling, and for that, I am thankful to have had roommates, and now close friends, outside the program that made it all the more enjoyable. Abraham Benguigui, I have lived with you for almost four years, and over that time, you have inspired me to learn to dance and to not take myself too seriously. Doug Stiegler, you are a finance guru and a biking

aficionado, thank you for sharing your interests, and always pushing me to do better in my own work. Fernando Fuentes is the definition of suave and a can-do attitude, we have yet to hang out without it turning into a story. Schuyler Stoller is easily the most kind-hearted, yet witty, person I have had the pleasure of meeting. I hope to, one day, cook nearly as well as you do. Austin Shopbell is the personification of a work ethic (maybe that was a byproduct of law school), but always manages to make time for a cold beer with a friend. Nissim Darwiche, you bring the perfect balance between poking fun and being genuinely warm, both of which are traits that I genuinely appreciate.

Some friendships extend a lifetime. To Yusef Al-Jarani, Alan Huels, Raja Gupa, and Alec McGail – thank you. There are too many things to be said about each one of you, but to put it succinctly, each of you inspire me to be my best and I look forward to many more experiences and antics together. Seth Ringel and Paul Peters have been rocks upon which I could rely on for support whenever and wherever, and always know how to get the party started. Amanda Botha, you are wiser beyond your years and have always been someone I could rely on for just about anything (and it helps that you've always been a short distance away since the day we met). Sabine Loos, you are the most fun loving and quirky (in the best possible way) person I know; I cherish every conversation with you and am in constant awe of your insight. Markus Harrigan, I am deeply appreciative of the numerous backpacking trips you have organized and for always letting me come along. I will always have a couch for you to crash on. Jasmine Moshiri, you are one of the most genuine people I have ever met and I only wish we had become friends earlier. I am a better person because of each and every single one of you. Please never stop humbling me.

Last but not least, thank you to my parents and sister. My mom and dad sacrificed a great deal to bring my sister and I to the States in search of a better life. Both of you have been incredibly supportive of my continuing education. Without your early encouragement of my education, I would not be here. Nilam, you have been a role model to me; you are both fierce and independent, and I admire you more than you may know.

Financial Acknowledgement

None of this work would have been possible without the generous support of multiple funding sources. The National Science Foundation, grant number 1505669, under the SusChEM initiative, funded portions of chapter 2, chapter 3, and chapter 4. Portions of the work in chapter 3 and chapter 4 was intellectually led by the Joint Center for Energy Storage Research (JCESR), an Energy Innovation Hub funded by the U.S. Department of Energy (DOE), Office of Science, Basic Energy Sciences (BES), under contract No. DEAC02-06CH11357. Chapter 5 was intellectually led by the Joint Center for Energy Storage Research (JCESR), an Energy Innovation Hub funded by the U.S. Department of Energy (DOE), Office of Science, Basic Energy Sciences (BES), under contract No. DEAC02-06CH11357. The work in chapter 6 was sponsored in part by Robert Bosch LLC through Bosch Energy Research Network Grant no. 12.1 0.BS.15.

1 Introduction

1.1 Conventional lithium-ion batteries

Global greenhouse gas (GHG) emissions have been on the rise and are directly related to global warming.[1] In the United States, the largest contributors to GHG emissions are the transportation and energy production sectors, respectively.[2] Energy storage has become an integral component to reducing GHGs in both industries. The leading energy storage device in both industries is the lithium-ion battery due to its promising cycle life, round trip efficiency, manufacturability, and decreasing costs.[3–5] The energy density of a battery is especially paramount for the transportation sector, and Li-ion technology has become the industry standard for vehicle electrification.

The Li-ion battery is composed of three main components: a porous graphite anode, a transition-metal oxide cathode, and an electrolyte. The electrodes house lithium and determine the total battery potential while the electrolyte facilitates ion transport between the two electrodes during charge and discharge. Conventional electrolytes are mixtures of nonaqueous liquid carbonates and lithium-based salts that fill porous separators and electrodes. An electrolyte must fulfill multiple requirements: 1) be able to form a stable solid-electrolyte interphase (SEI), 2) have a high voltage stability window, 3) be able to transport lithium cations with minimal ohmic loss, 4) be able to support large power draws (and thus current), 5) be able to be operated in a wide range of temperatures, and 6) be safe.[6–8] Traditional carbonate electrolytes fulfil most of these criteria, but an increasingly electric transportation industry will require electrolytes that can improve energy density, capacity, and safety.

1.2 Enabling next-generation lithium-based technology

Commercial Li-ion batteries are quickly approaching the theoretical gravimetric and volumetric energy density of 385 Wh/kg and ca. 770 Wh/L.[9,10] Consumers view range anxiety as a significant barrier to adopting electric vehicles, and thus new battery chemistries that enable higher energy densities are a necessity.[11] Conventional Li-ion batteries also face trade-offs between high power and energy, which hinders their ability to be charged and discharged quickly.[12–15] In order to surpass these limitations, considerable research is focused on developing next generation electrode materials that can increase nominal battery voltages.[16–19] Focus has also been drawn to developing electrolytes with improved ion transport properties are also being to facilitate higher current draws without sacrificing the energy within a cell.[20–22] In Fig. 1.1, an example of a Li-ion battery with an NMC cathode undergoing charging at different c-rates is shown.[23] It is evident that as the battery is charged faster, less capacity, and therefore energy, is available within the battery.

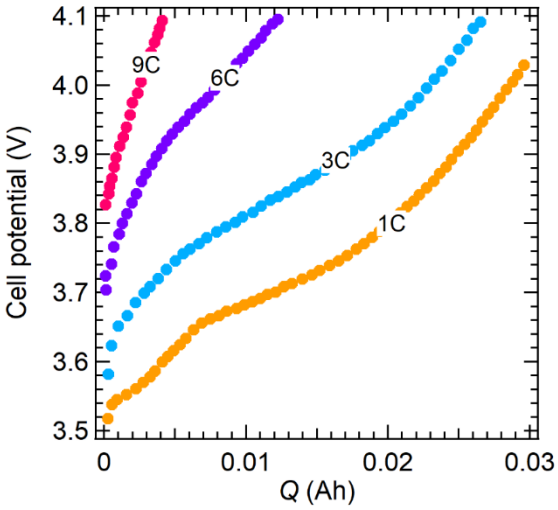

Figure 1.1 Cell potential vs. capacity for an NMC Li-ion cell undergoing charging at different c-rates.[23]

Fluorinated electrolytes have come to the forefront for enabling higher voltage cathode materials. They have been shown to increase the electrolyte stability window and allow for the formation of a stable SEI layer.[24–30] Fluorinated electrolytes have also been shown to be less volatile compared to traditional electrolytes.[29–33] Recent, attention has also turned to solvent-in-salt electrolytes, which are composed, primarily (by weight %), of a lithium salt with a minority solvent component. While these systems have shown lower conductivity values compared to traditional liquid electrolytes, they have been shown to increase the electrolyte electrochemical stability window and to stabilize lithium metal anodes.[34–37] However, the ion transport properties of many electrolytes, both traditional and novel, are not well understood.

1.3 Transport phenomena in liquid electrolytes

In order to completely characterize and model an electrolyte, Onsager reciprocal relations require $n(n\text{-}1)/2$ transport parameters, where n is the number of independent species.[38,39] In addition, m-1 activity coefficients are required due to the Gibbs-Duhem relation, where m is the number of electronically neutral species. For a binary electrolyte (solvent, single anion, single cation), the three transport parameters take the form of conductivity, salt diffusion coefficient, and the transference number. The thermodynamic factor is also required and describes the thermodynamic ideality of the salt and solvent mixture.

Conductivity is a measure of the ohmic ionic resistance of the electrolytes. The salt diffusion coefficient determines the speed at which a salt concentration gradient relaxes. The transference number describes the severity of the salt concentration gradients that build up within an electrolyte. Under a given dc potential, for electrolytes in lithium-based batteries whose Li^+ transference number is not one, concentration gradients develop. These gradients are a product of the net flux of the anion and cation at steady-state. Under steady-state conditions, the net flux of the anion is zero due to the lack of redox reactions at either electrode surface, whereas the cation net flux is towards the reducing electrode.

The thermodynamic factor and all three transport properties are crucial for understanding mass transport within a binary electrolyte. Characterizing each of these parameters for a wide range of salt concentrations allows for accurate modeling within a battery. Salt concentration gradients can be modeled, and in doing so, the maximum current draw that is allowable by the electrolyte can be predicted. Knowing the limiting current of an electrolyte would be highly beneficial in determining the application of said electrolyte. The overpolarization in a battery due to a concentration gradient can also be predicted. If the overpolarization is large enough, a battery can be prevented from fully charging or discharging due to the limitations placed on the cell to prevent degradation of the electrolyte.

1.4 Structure of the dissertation

The goal of this work is fundamentally understand ion transport properties in nonaqueous liquid electrolytes. This work is split into two broad categories, where chapters 2 – 4 focus on novel liquid perfluoroether electrolytes and chapters 5 and 6 focus on more traditional nonaqueous liquid electrolytes.

Chapter 2 studies the effect of molecular weight and anion size on conductivity and the ideal transference number. The efficacy of an electrolyte is realized by the product of conductivity and the ideal transference number, and it is found that mixtures of LiFSI with C8-DMC exhibit the most promising transport properties. Chapter 3 delves into complete characterization of ion transport properties for mixtures of LiFSI and C8-DMC using Newman's concentrated solution theory. It is found that the transference number obtained using dilute solution theory is qualitatively and quantitatively different from that obtained using concentrated solution theory. Chapter 4 uses the transport properties obtained in chapter 3 to model the limiting current of LiFSI/C8-DMC and compare those results with experiments. Both salt solubility limitations and salt depletion are found to be causes for the limiting current, and hence, cell failure. Chapter 5 measures a full set of transport properties for mixtures of low molecular weight poly(ethylene oxide), tetraethylene glycol dimethyl ether (tetraglyme), and LiTFSI for both T = 30 °C and 90 °C. The measured transport properties are used to predict the limiting current and compared to experimental results. We hypothesize that salt solubility limits are a cause for cell failure in the limit of high salt concentrations. In chapter 6, transport properties for mixtures of LiFSI and propylene carbonate (PC) and $LiPF_6$ and PC are measured using concentrated solution theory. LiFSI/PC mixtures exhibit larger transference numbers compared to $LiPF_6$/PC mixtures. Experimental electrolytic potential drops for LiFSI/PC are compared to those predicted by theory and qualitative agreement is found as a function of the applied steady-state current density and starting salt concentration.

2 Effect of Anion Size on Conductivity and Transference Number on Perfluoroether Electrolytes with Lithium Salts[†]

2.1 Introduction

As applications for rechargeable lithium batteries continue to increase in number, there are added demands for improving the safety and performance. One way of increasing safety is by replacing the flammable electrolytes used in current batteries with nonflammable materials. Current electrolytes comprise mixtures of alkyl carbonates and lithium hexafluorophosphate.[40–42] The alkyl carbonates contain electronegative oxygen atoms that solvate lithium ions. The use of fluorinated anions such as hexafluorophosphate stems from the electronegativity of fluorine, which enhances charge delocalization and ion dissociation. Mixtures of oligomeric and long chain polyethylene oxide and lithium bis(trifluoromethanesulfonyl)imide (LiTFSI) have also been studied for lithium battery applications. These electrolytes also contain electronegative oxygen atoms and lithium salts with fluorinated anions. In order to increase performance and energy capacity of Li-ion systems, cathodes with high operating potentials (5 V vs. Li^+/Li) have been proposed.[43] However, common battery electrolytes, like ethylene carbonate and dimethyl carbonate, decompose above 4.5 V vs. Li^+/Li.[44] Fluorinated compounds have been shown to have larger stability windows, thereby allowing the use of high operating potential cathodes.[45]

This paper is part of a series wherein we examine the possibility of using fluorinated oligomers to dissolve lithium salts with fluorinated anions.[31,46–49] Our hypothesis is that salt solubility in these systems stems from interactions between the oligomers and the anion. It is known that fluorinated compounds are often only miscible in each other; this is often referred to as the fluorous effect.[50] While the fluorous effect is usually used to describe the mixing of neutral species, there is evidence of similar effects in mixtures of fluorinated ionic compounds and fluorinated polymers.[51] Our work is a departure from the traditional approach of exploiting interactions between the solvent and the cation. The oligomers used in this study are perfluoroethers (PFE) with dimethyl carbonate end groups. The chemical formulae are given in Figure 2.1 and we refer to them as C6-DMC and C8-DMC. Our electrolytes comprise mixtures of these PFEs and three lithium salts. In addition to LiTFSI, we have also used lithium bis(fluorosulfonyl)imide (LiFSI) and lithium bis(pentafluoroethanesulfonyl)imide (LiBETI). The chemical formulae of the salts used in this study are also given in Figure 2.1. Our study thus examines the effect of PFE chain length and anion size on ion transport. We characterize ion transport by measuring conductivity using ac impedance and the approximate cation transference number using the steady-state current method.[52–54] We also report on the interfacial impedance between PFE electrolytes and lithium metal electrodes.

A large majority of studies on PEO-based electrolytes use LiTFSI as the salt.[55–57] While these electrolytes exhibit reasonable conductivity at room temperature and lithium salts can be dissolved at high concentrations, the transference number based on the steady-state current method can be as low as 0.05.[58] This is due to specific interactions between the solvent and the cation. A consequence of our hypothesis that the properties of PFE electrolytes are governed by

[†] This chapter is reported in Shah, D. B., *et al*. Effect of Anion Size on Conductivity and Transference number of Perfluoroether Electrolytes with Lithium Salts. *J. Electrochem. Soc.* **2017**, *164*, A3511 – A3517.

interactions between the solvent and the anion is the expectation that these systems should exhibit significantly higher transference numbers. In this work, we compare ion transport properties of PFE-based electrolytes with literature values of PEO-based electrolytes.

As can be seen in Fig. 2.1, the PFEs used in this study are fluorinated analogs of oligomeric PEOs, triglyme and tetraglyme. The properties of these two classes of electrolytes will differ dramatically for several reasons: (1) The fluorine atoms in PFE, which replace hydrogens in PEO, are actually similar to oxygen atoms in terms of size and electronegativity. (2) Steric effects will differ because C-F bonds are longer and occupy significantly more space than C-H bonds.[59] (3) Interfacial impedance will be impacted by differences in the spontaneous reactions between the electrolytes and lithium metal, and the fact that the C-F bond is stronger than the C-H bond. Our study sheds some light on the effect of these differences on ion transport.

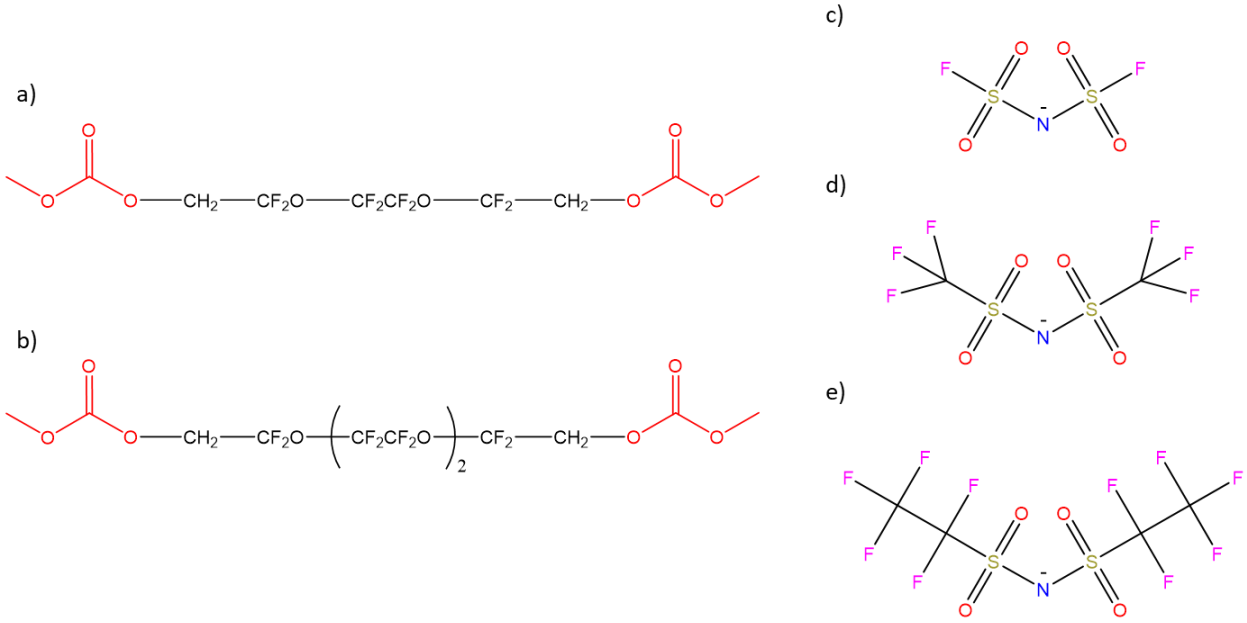

Figure 2.1 a) C6-DMC, b) C8-DMC, c) FSI anion, d) TFSI anion, and e) BETI anion.

2.2 Experimental Details

2.2.1 PFE Synthesis

The PFEs were synthesized from diol terminated precursors following procedures described in Wong, D. *et al.* and Olson, K. *et al.*[31,49] Scheme 2.1 shows our approach to synthesize C6-DMC (the approach for synthesizing C8-DMC is essentially identical). 0.10 mol of the perfluorinated glycol precursor (0.20 mol -OH end groups) and three molar equivalents triethylamine (84 mL, 0.60 mol) were dissolved in 400 mL of 1,1,1,3,3-pentafluorobutane in a 1 L 3-neck round-bottom flask. The solution was cooled to 0°C under nitrogen atmosphere. Methyl chloroformate (46 mL, 0.60 mol) was added dropwise over the course of two hours with rapid stirring, resulting in significant gas evolution and formation of the white triethylamine hydrochloride (TEA HCl)

precipitate. The reaction was stirred overnight under nitrogen atmosphere at ambient temperature, and reaction completion was confirmed by Fourier-transform infrared spectroscopy.

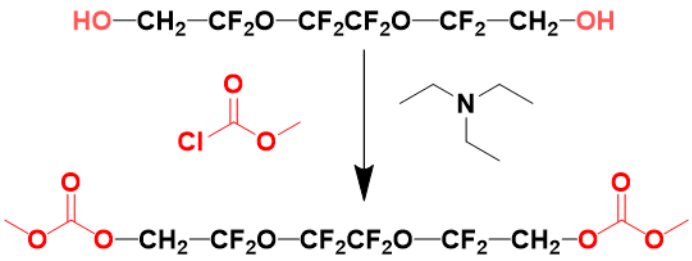

Scheme 2.1 Reaction to produce C6-DMC form the commercial C6-Diol analog. Conversion of the C8-Diol analog proceeds through the same reaction scheme to produce C8-DMC.

The TEA HCl salt was removed by gravity filtration, yielding a pale-yellow solution. The salt was washed 3x with 50 mL 1,1,1,3,3-pentafluorobutane to remove residual product. The combined pentafluorobutane solution was then washed 3x with 500 mL water and 1x with 500 mL brine using a separatory funnel. The solution was stirred with activated carbon to remove coloration and dried with magnesium sulfate. After filtering the solids, pentafluorobutane was removed under reduced pressure, yielding a clear, faintly yellow oil. The dimethyl carbonate terminated perfluorinated triethylene- and tetraethylene ethers (C6-DMC and C8-DMC, respectively) were dried under vacuum at 50°C for 2 days. The molecular weight (MW) for C6-DMC is 410 g/mol and that of C8-DMC is 526 g/mol. Figs. 2.S1 and 2.S2 in the supplemental information shows the NMR spectra of the final products dissolved in deuterated acetone.

Thermogravimetric analysis (TGA) was used to determine the volatility of C6-DMC and C8-DMC using a TA Instruments Q5000 TGA under nitrogen flow (10 mL/min) from 25 °C to 500 °C at a heating rate of 10 °C/min. The temperatures at which a 5% mass loss were recorded from the TGA curves were 126 and 129 °C for C6-DMC and C8-DMC. Closed-cup flash point measurements were performed using an Erdco Rapid Tester small-scale apparatus following ASTM D 3278. No flash point was detected for C6-DMC or C8-DMC within the experimental window (up to 250°C).

2.2.2 Salts

Lithium bis(fluorosulfonyl)imide (cat. no. 097602) and lithium bis(pentafluoroethanesulfonyl)imide (cat. no. 080110) were purchased from Oakwood Products, Inc. Both salts were ≥ 99% pure, as confirmed by a Certificate of Analysis form. Lithium bis(trifluoromethanesulfonyl)imide was purchased from Novolyte and was also reported to be ≥ 99% pure. All three salts were dried at 120 °C under dynamic vacuum for three days inside a glovebox antechamber. All salts, oligomers, and electrolytes were stored within an argon filled Vac glovebox with H_2O and O_2 concentrations kept below 1 ppm.

2.2.3 Electrolyte Preparation

Prior to being brought into the glovebox, the oligomers were dried under active vacuum inside the glovebox antechamber at 50 °C for 72 hours. In order to form electrolytes, a predetermined amount of Li salt was added to a known mass of either oligomer. Once the salt was added, the electrolytes were placed on a stir plate and were allowed to mix for 12 hours or more using a magnetic stir bar.

2.2.4 Experimental Characterization

Conductivity samples were prepared by sandwiching an electrolyte soaked separator, Celgard 2500 (Celgard Company), with a stainless steel shim (MTI Corporation) on either side. The stainless steel shims were 15.5 mm in diameter and 0.2 mm in thickness; Celgard 2500 was cut to 19 mm in diameter and had an average thickness of 25.4 ± 0.6 μm. The thickness of the separator was measured for each sample. The stack was placed into CR2032 coin cells (Pred Materials) that were than hermetically sealed. Three replicate cells were produced and measured for each electrolyte. Conductivity data was collected through ac impedance spectroscopy performed on a Bio-Logic VMP3 potentiostat. The frequency range analyzed was between 1MHz and 100 mHz at an amplitude of 60 mV. Fig. 2.2a shows typical impedance data collected in coin cells and the equivalent circuit is shown in the inset. R is the resistance of the electrolyte/separator composite, Q and Q_{int} are the constant phase elements associated with the electrolyte/separator and interface, respectively, and R_c and L_c are the resistance and inductance, respectively, associated with the VMP3 cables. The conductivity of the electrolyte was calculate using Eq. 2.1

$$\kappa = c\frac{l}{RA} \tag{2.1}$$

where A is the electrode area of the coin cells in cm^2, l is the thickness of the separator in cm, and c is an empirically determined constant to account for the presence of the separator. The constant c was determined by measuring the conductivity of four electrolytes in a liquid cell described in reference 60: C6-DMC with 3 wt % LiTFSI and C8-DMC with 3 wt % LiTFSI, C6-DMC with 20 wt % LiFSI , and C6-DMC with 15 wt % LiBETI at 30 °C. The ratio of the measured conductivity in the liquid cell to that measured in the coin cell with the separator was 8.70 ± 0.06 for the four electrolytes.

Transference number cells were similar to the conductivity cells. However, instead of using stainless steel shims, lithium discs, cut from lithium chips (MTI Corp.), were used on either side of the electrolyte soaked Celgard. The diameter of the 150 μm thick Li disc was 12.7 mm. Three replicate cells were produced for each electrolyte. Data were collected on a Bio-Logic VMP3 potentiostat. Each sample cell was subjected to a conditioning treatment, which consisted of charge and discharge cycles at 0.02 mA/cm^2 in order to help stabilize the interfacial layer. The sequence performed was a 4 hour charge, 30 minutes rest, a 4 hour discharge, 30 minutes rest, and repeated for a total of 6 times. Ac impedance was carried out before the beginning of conditioning, after each rest step, and at the end of conditioning. Each sample was then polarized

at ΔV = +/- 40 mV and +/- 80 mV for 1 hour in order to ensure that the steady state transference number collected was independent of the applied potential. During chronopotentiometry, current was measured at 1 second intervals in order to capture the full current response. Ac impedance data were collected every 20 minutes with an ac amplitude of 20 mV and 40 mV for the dc applied potentials of +/- 40 mV and +/- 80 mV, respectively. The data obtained for all of these cases were similar. We report data acquired using ac impedance spectroscopy with an amplitude of 20 mV during dc polarization of 40 mV. Data were modeled to the equivalent circuit shown in the inset of Fig. 2.2b, where R_{int} was the interfacial resistance. Fig. 2.2b represents the typical data seen for Li symmetric cells.

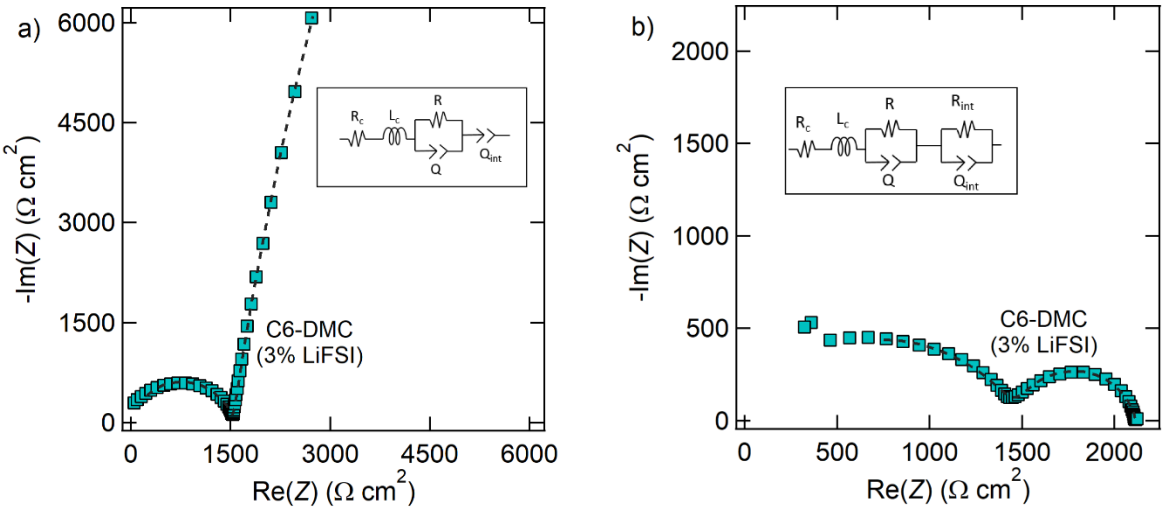

Figure 2.2 Typical impedance profiles and equivalent circuits for a) conductivity and b) Li symmetric samples. The dashed black lines are the fits to the equivalent circuits shown. Data collected at 30 °C.

Assuming Ohm's law, which is a reasonable assumption prior to cell polarization due to a lack of concentration gradients, an initial current, I_Ω, is given by Eq. 2.2:

$$I_\Omega = \frac{\Delta V}{R_T} \tag{2.2}$$

where ΔV is the applied polarization potential and R_T is the total initial cell resistance as measured by ac impedance spectroscopy. Eq. 2.3 was then used to calculate the ideal transference number:

$$t_{+,id} = \frac{I_{ss}}{I_\Omega}\left(\frac{\Delta V - I_\Omega R_{i,0}}{\Delta V - I_{ss} R_{i,ss}}\right) \tag{2.3}$$

where I_{ss} is the steady state current, $R_{i,0}$ is the initial interfacial resistance, and $R_{i,ss}$ is the interfacial resistance when I_{ss} is reached. The transference number alludes to how polarizable an electrolyte is, thus a transference number near unity suggests that concentration gradients do not build up within the electrolyte.

All electrochemical characterization experiments were conducted at 30 °C.

2.3 Results and Discussion

The solubility limits for LiFSI, LiTFSI, and LiBETI in C6-DMC and C8-DMC are shown in Fig. 2.3. The salts were added in 5 wt% increments until the solubility limit was reached. The solubility limit for each electrolyte was determined visually. Salts were assumed fully dissolved if the electrolyte was transparent, and phase separated if it was opaque. The solubility limit is taken as the average of the solution's salt concentration just below the solubility limit (transparent) and just above the solubility limit (opaque). Fig. 2.3 shows the salt wt % for the six PFE/salt combinations. The solubility limit is a weak function of anion size for C8-DMC, increasing monotonically from 27.5 to 37.5 wt % in our experimental window. In uncharged systems, the entropy of mixing decreases with increasing molecular size, which, in turn, is expected to result in decreasing solubility limits. The observed trend in C8-DMC is not consistent with this expectation. It is possible that dissociation is favored in salts with large anions due to both lowering of lattice energy and charge delocalization, and that the observed trend in C8-DMC is due to this effect. The dependence of the solubility limit on anion size in C6-DMC is more interesting. The solubility of LiTFSI, the salt with an anion of intermediate size, is only 4.4 wt %, which is about an order of magnitude lower than that of all of the other five systems. This experiment was carried out three times in order to confirm the surprisingly low solubility limit in C6-DMC; all samples with LiTFSI concentrations from 5.3 to 29.9 wt. % were phase-separated and opaque. Perhaps the entropic effects mentioned above are not entirely negligible in PFE electrolytes. The data in Fig. 2.3 indicate that the interactions between the fluorinated lithium salts and perfluorinated electrolyte solvents are complex, and more work is required to establish the underpinnings of solubility.

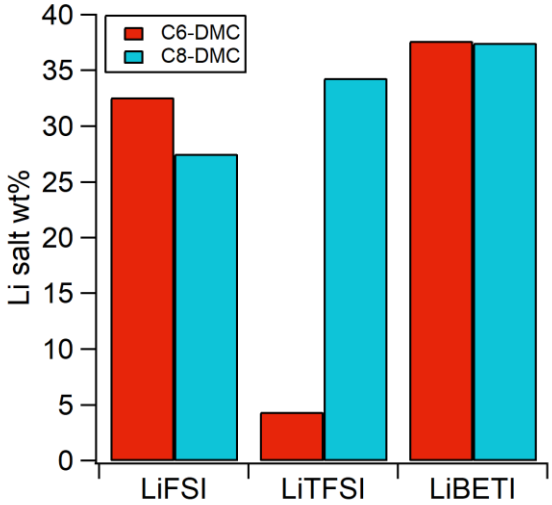

Figure 2.3 Li salt solubility in C6-DMC and C8-DMC as a function of salt wt %

The lithium salt that is predominant in the literature on PEO-based electrolytes, LiTFSI, cannot be used with C6-DMC. This suggests that replacing the hydrogen atom with fluorine has a large

effect on electrolyte properties. All of our previous papers on perfluoropolyether (PFPE) electrolytes[31,46–49] are based on LiTFSI. However, the data in Fig. 2.3 suggests that other salts might be better suited for perfluorinated electrolytes.

The dependence of conductivity, κ, on salt concentration for C6-DMC electrolytes, obtained with blocking electrodes, is shown in Fig. 2.4a. The final datum for each data set represents the solubility limit. For LiFSI and LiBETI electrolytes, conductivity increases rapidly at low salt concentrations, goes through a shallow maximum, and decreases slightly at high salt concentrations. The limited solubility of TFSI- severely limits our measurement window in C6-DMC. Within the measurement window, however, the conductivity of LiTFSI- and LiBETI-based electrolytes are similar. At low salt concentrations, the conductivity of the LiFSI electrolyte is significantly higher than that of the others. The maximum conductivity of LiFSI in C6-DMC is 1 x 10^{-4} S/cm, which is also significantly higher than that of LiBETI in the same solvent. At high concentrations, however, the conductivities of the two systems are similar, see data at 30 wt % salt.

The dependence of conductivity, κ, on salt concentration for C8-DMC electrolytes, obtained with blocking electrodes, is shown in Fig. 2.4b. All three electrolytes exhibit a shallow maximum with LiFSI exhibiting the highest conductivity followed by LiTFSI followed by LiBETI. At many salt concentrations, the conductivity of LiTFSI and LiBETI electrolytes in C8-DMC are within experimental error. This is especially true at salt concentrations ≥ 25 wt %. It appears as if the conductivity of the LiFSI electrolytes in C8-DMC would approach that of the other electrolytes at high salt concentrations (30 – 35 wt %), but a direct comparison is precluded by limited solubility (see Fig. 2.4b).

For the case of amorphous PEO with methyl end groups (250 g/mol) and with 25 wt % LiTFSI, the maximum conductivity at 25 °C is about 2x10^{-3} S/cm.[61] The maximum conductivity of PFE electrolytes is thus a factor of five lower than that of PEO electrolytes.

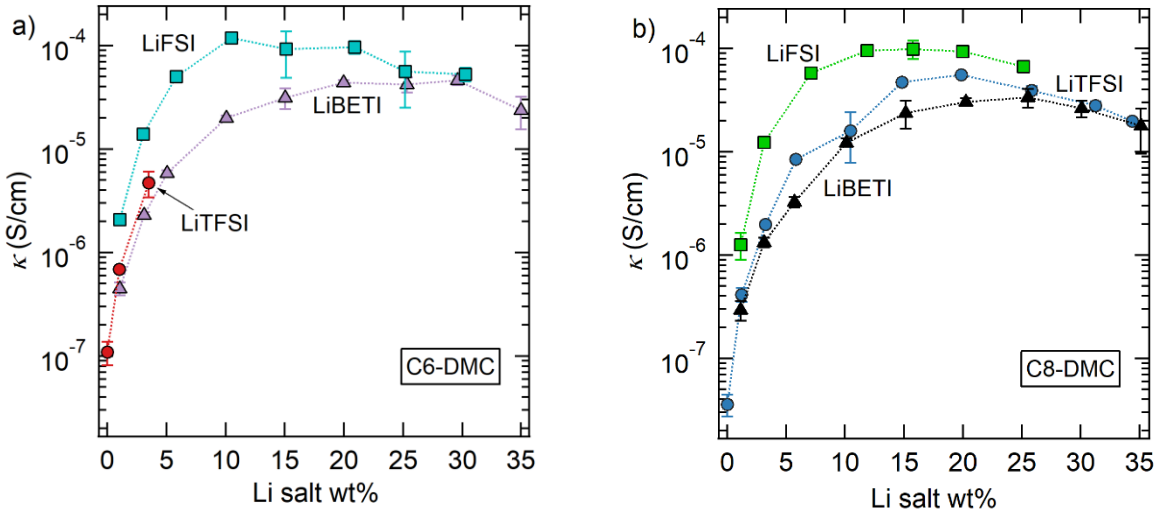

Figure 2.4 Conductivity of LiFSI, LiTFSI, and LiBETI in a) C6-DMC and b) C8-DMC. All data collected at 30 °C.

The symbols in Figs. 2.5a and 2.5b show the dependence of conductivity, κ, on salt concentration for C6-DMC and C8-DMC electrolytes, obtained with non-blocking lithium metal electrodes. The continuous curves in Fig. 2.5 show κ vs salt concentration obtained with blocking electrodes (Fig. 2.4). In most cases, the conductivities determined with either blocking or non-blocking electrodes are similar. In principle, there should be no difference in conductivity values obtained using blocking or non-blocking electrodes. However, one might expect irreversible reactions between the fluorinated electrolytes and lithium metal to interfere with the conductivity measurements. It is evident that this is not the case. The irreversible reactions, however, do result in measurable interfacial resistances (Fig. 2.2b).

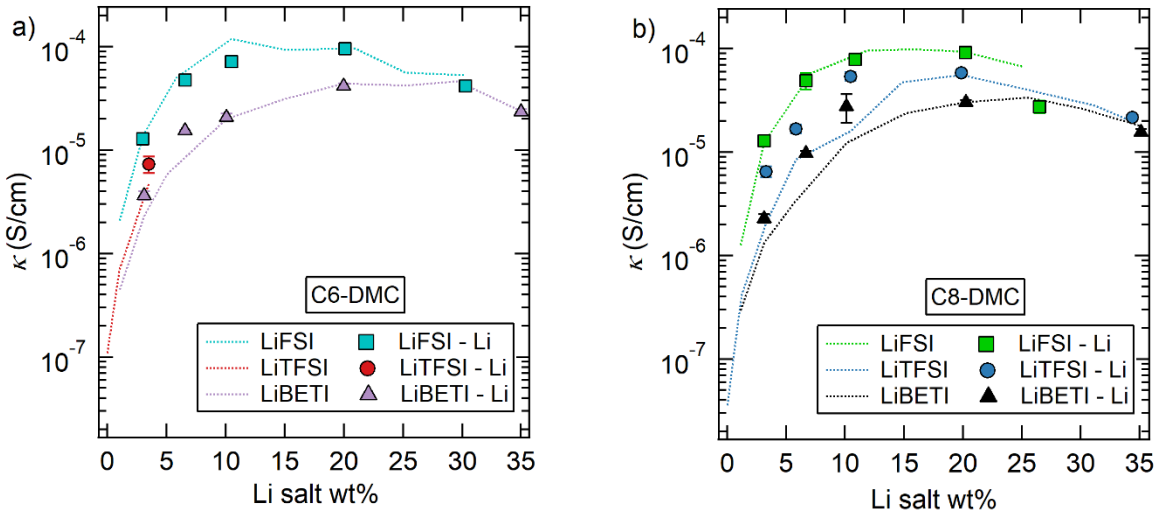

Figure 2.5 Conductivity values extracted from Li symmetric cells and compared to the results from the blocking electrodes for a) C6-DMC and b) C8-DMC. Markers and errors bars from the blocking electrodes were removed for clarity, but the blocking electrode conductivities can be seen as continuous lines. Conductivities calculated from non-blocking lithium electrodes are shown as symbols.

The dependence of interfacial resistance, R_i, on salt concentration for C6-DMC is shown in Fig. 2.6a. Due to the limited solubility of LiTFSI in C6-DMC, only one concentration was studied (3 wt % salt). At low salt concentrations, R_i for LiTFSI was similar to that of LiBETI in this solvent. Interestingly, the same can be said for conductivity (Fig. 2.4a). For the soluble salts, LiFSI and LiBETI, R_i decreases with increasing salt concentration until R_i reaches a minimum at 10 wt %. At this concentration, for LiFSI, the minimum R_i for LiFSI is 155 ± 28 Ω cm^2. This is about an order of magnitude lower than that of LiBETI, which is 1040 ± 24.5 Ω cm^2. At concentrations between 10 wt % and the solubility limit, R_i of LiBETI increases dramatically to values as high as 2019 +/- 569 Ω cm^2, while that of LiFSI approaches a plateau.

The dependence of interfacial resistance, R_i, on salt concentration for C8-DMC is shown in Fig. 2.6b. R_i obtained from LiBETI exhibits a minimum that is similar to that obtained in C6-DMC (Fig. 2.6a). R_i obtained from LiTFSI is independent of salt concentration (within experimental error). R_i obtained from LiFSI exhibits a shallow maximum with a minimum value of 154 ± 23 Ω cm^2 at 20 wt %. While the trends seen in Fig. 2.6b are complex, at a given salt concentration, interfacial impedance generally decreases with decreasing anion size.

It is noteworthy that LiFSI/C6-DMC and LiFSI/C8-DMC, the systems that exhibit the highest conductivity, also exhibit the lowest interfacial impedance (Figs. 2.4 and 2.6).

A significant motivation to the large number of published papers on lithium metal and PEO-based electrolytes is the stability of the solid-electrolyte interface that forms in these systems.[62,63] The interfacial impedance of lithium metal and PEO (MW = 4000 kg/mol) with LiBETI was measured by Appetecchi, G. B. *et al.*[64] They report a minimum of 80 Ω cm^2 in an electrolyte with 20wt % salt. In another study by Zhang, H. *et al.* on LiFSI and LiTFSI in PEO (MW = 5000 kg/mol) at concentrations of 17.5 and 24.5 wt %, R_i values of 80 Ω cm^2 and 325 Ω cm^2 were obtained, respectively.[65] The values of R_i reported in our study for LiFSI/PFE systems are thus similar to those of LiFSI/PEO, and significantly lower than that of LiTFSI/PEO. The interfacial resistances that were measured in the PEO electrolytes in references 64 and 65 were obtained without the passage of current. In contrast, the values reported in Fig. 6 were obtained after the passage of current; see details about conditioning cycles in section 2.3 (Experimental Characterization). The differences in R_i of PFE and PEO electrolytes could also be due to differences in hydrophilicity and the presence of trace amounts water.[66]

Figs. 2.7a and 2.7b show the current obtained upon application of a dc potential of 40 mV in C6-DMC and C8-DMC electrolytes. The data shown here were obtained from solutions of LiFSI, LiTFSI, and LiBETI at a salt concentration of 3 wt % for both electrolytes. In all cases, the current obtained at early times is slightly higher than that obtained at steady-state. The steady-state current, I_{ss}, obtained at t > 10 min, is highest for LiFSI, followed by LiTFSI and then LiBETI. I_{ss} is governed by electrolyte conductivity, interfacial impedance, and other transport properties, namely the salt diffusion coefficient and transference number.[67] The data in Fig. 2.7 enable calculation of the approximate transference number based on steady-state current, $t_{+,id}$, using Eq. 2.2 and 2.3.

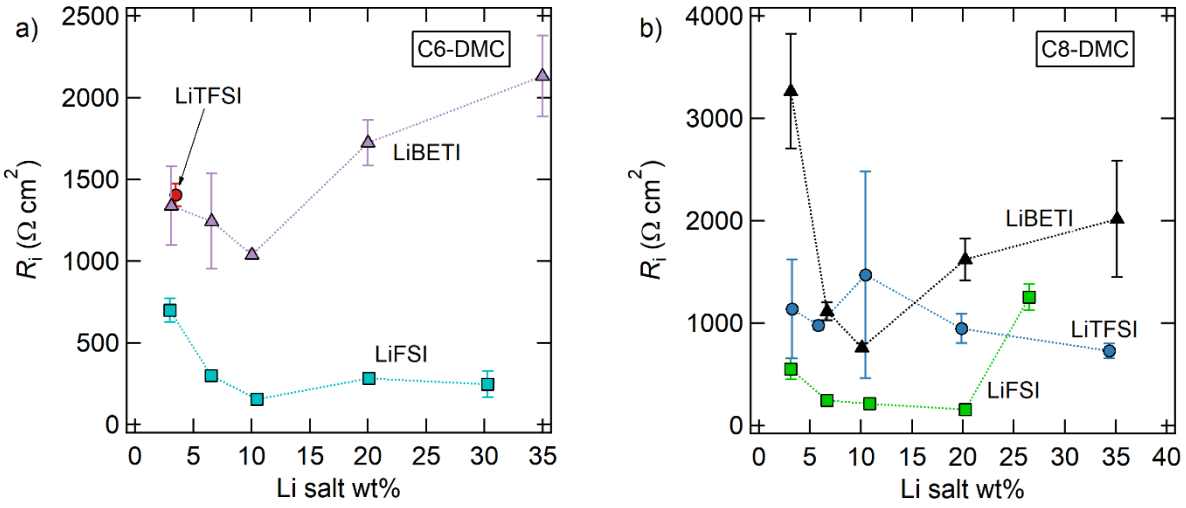

Figure 2.6: Final interfacial resistance as a function of Li salt concentration and type of Li salt for a) C6-DMC and b) C8-DMC.

Fig. 2.8a plots $t_{+,id}$ against salt concentration for C6-DMC. At the lowest salt concentration (3 wt %), all three electrolytes exhibit $t_{+,id}$ values near unity (between 0.93 and 0.98). For the soluble salts, LiFSI and LiBETI, $t_{+,id}$ decreases with increasing salt concentration. The LiFSI electrolytes reach a minimum of 0.64 ± 0.03 at 30 wt %, while the LiBETI electrolytes reach a minimum of 0.82 ± 0.02 at 35 wt %. Fig. 2.8b plots $t_{+,id}$ against salt concentration for C8-DMC. For LiBETI and LiTFSI, $t_{+,id}$ decreases with increasing salt concentration. For LiFSI, $t_{+,id}$ reaches a minimum of 0.73 ± 0.05 at 20 wt %. Over most of the experimental window, $t_{+,id}$, at a given salt concentration, increases with anion size: BETI- > TFSI- > FSI-. This result is expected as larger ions should be less mobile.

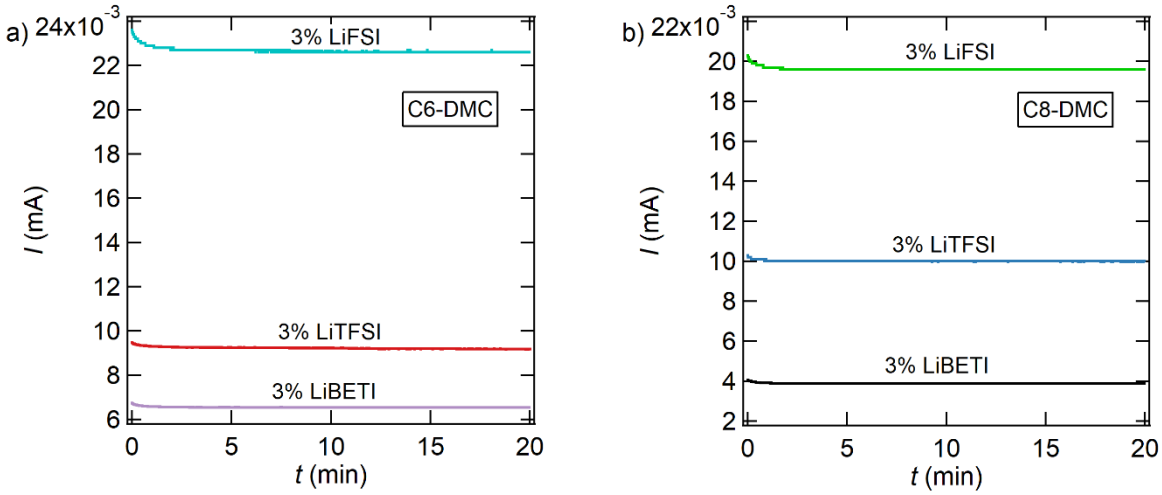

Figure 2.7: Typical current vs time profile for a) C6-DMC and b) C8-DMC as a function of Li salt. Notice that the steady-state current is a strong function of the anion.

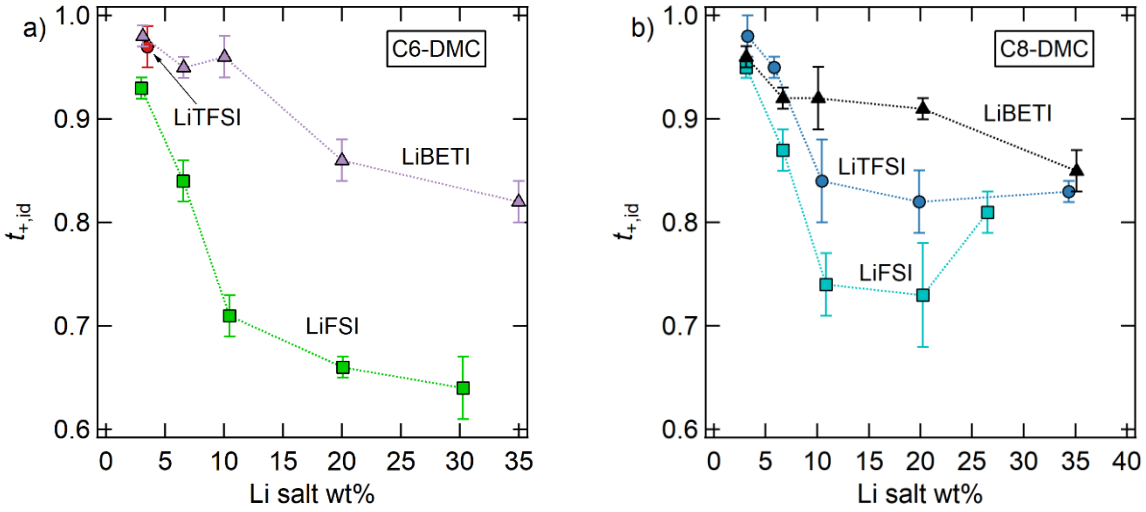

Figure 2.8 Ideal transference number for a) C6-DMC and b) C8-DMC as a function of Li salt and Li salt wt %.

Of note is that even though LiFSI has the lowest $t_{+,id}$ value in this study, it is still greater than 0.6 in C6-DMC and greater than 0.7 in C8-DMC across all concentrations. This is still much

higher than PEO-based electrolytes wherein $t_{+,id}$ values are reported to be in the range of 0.1-0.4.[68] Furthermore, $t_{+,id}$ values for C8-DMC electrolytes are higher than those for C6-DMC electrolytes. In previous work, it was shown that $t_{+,id}$ for a 9.1 wt % LiTFSI in PFPE with DMC endgroups (MW = 1.1 kg/mol) was 0.9,[46] which is higher than that of 10 wt % LiTFSI in C8-DMC. These observations suggest that $t_{+,id}$ increases with increasing molecular weight. In contrast, $t_{+,id}$ of PEO-based electrolytes decrease with increasing molecular weight.[68] The presence of specific interactions between PEO and Li cations is well-established, and this effect is used to describe the dependence of $t_{+,id}$ and molecular weight.[69] Our observations in PFPE electrolytes thus suggest the presence of specific interactions between the anions and the fluorinated backbone.

Figs. 2.4 and 2.8 indicate that increasing salt concentration has opposite effects on κ and $t_{+,id}$: κ generally increases while $t_{+,id}$ generally decreases with salt concentration. In practical applications, the current through an electrolyte under an applied dc potential is the important metric. This metric is proportional to the product $\kappa t_{+,id}$.[52,54,69,70] Figs. 2.9a and 2.9b show the dependence of $\kappa t_{+,id}$ on salt concentration. A maximum is observed in the vicinity of 20 wt % salt in both C6-DMC and C8-DMC, irrespective of the soluble salt used. The optimal value of $\kappa t_{+,id}$ in PFE electrolytes, 7 x 10^{-5} S/cm, is lower than that of PEO-based electrolytes, which are in the range of 2 x 10^{-4} to 5 x 10^{-4} S/cm. Additionally, $\kappa t_{+,id}$ of LiFSI in C8-DMC is within experimental error of LiFSI in C6-DMC, even though C8-DMC is of a higher molecular weight. It is evident that the optimal salt concentration for our PFE electrolytes is 20 wt %; neither κ nor $t_{+,id}$ is maximized at this concentration.

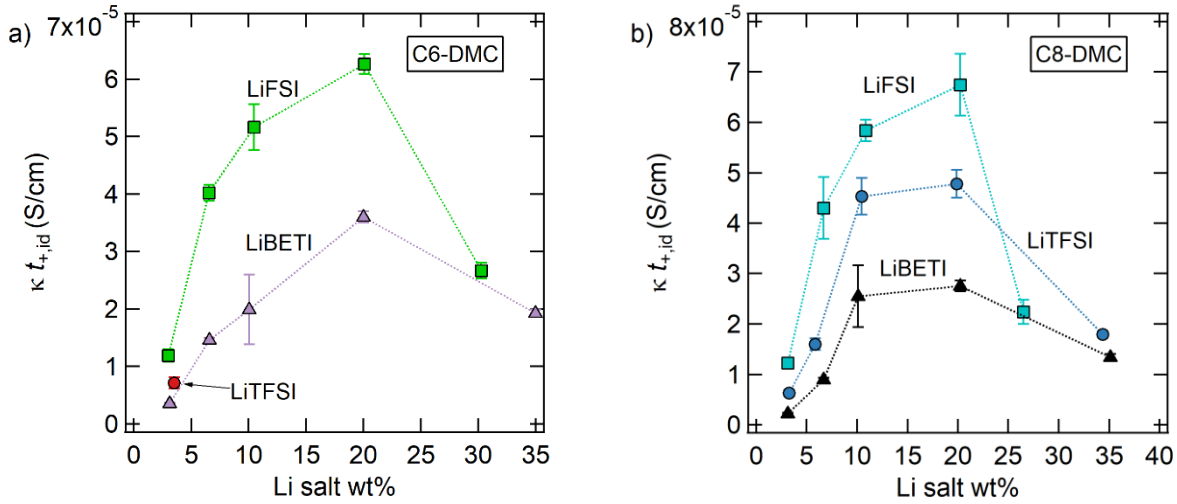

Figure 2.9 Conductivity of the Li cation for a) C6-DMC and b) C8-DMC as a function of Li salt and Li salt wt %.

2.4 Conclusion

The effect of anion size on ion transport in perfluoropolyether electrolytes was studied by examining mixtures of LiFSI, LiTFSI, and LiBETI in C6-DMC and C8-DMC. The solubility

limit of all systems was in the 25 – 35 wt % range except for LiTFSI in C6-DMC, which was 4.4 wt %. Electrolytes with LiFSI exhibited the highest conductivity, κ, and lowest interfacial impedance. However, their steady-state transference number, $t_{+,id}$, was lower than that of the other two salts. The efficacy of the electrolytes was studied by examining the product, $\kappa t_{+,id}$. The optimal salt concentration was 20 wt % in all cases (except the system with limited salt solubility). Of the salts studied, LiFSI-based systems exhibited the highest value of $\kappa t_{+,id}$. Our work suggests that specific interactions between the anions and the fluorinated backbones of our solvents may be important. Further spectroscopic and computational studies to examine these effects seem warranted.

2.5 Supplemental Information

2.5.1 Synthesis

Fig. 2.S1 shows ^{1}H NMR of the C6-DMC neat oligomer after synthesis and purification in deuterated acetone. The measurement was carried out in deuterated acetone. The peak at 3.84 ppm corresponds to the hydrogens attached to the methyl group while the peak at 4.73 ppm corresponds to the hydrogens part of the backbone. The peak integration values, which are listed below each peak, correspond to the number of hydrogens contributing to that peak.

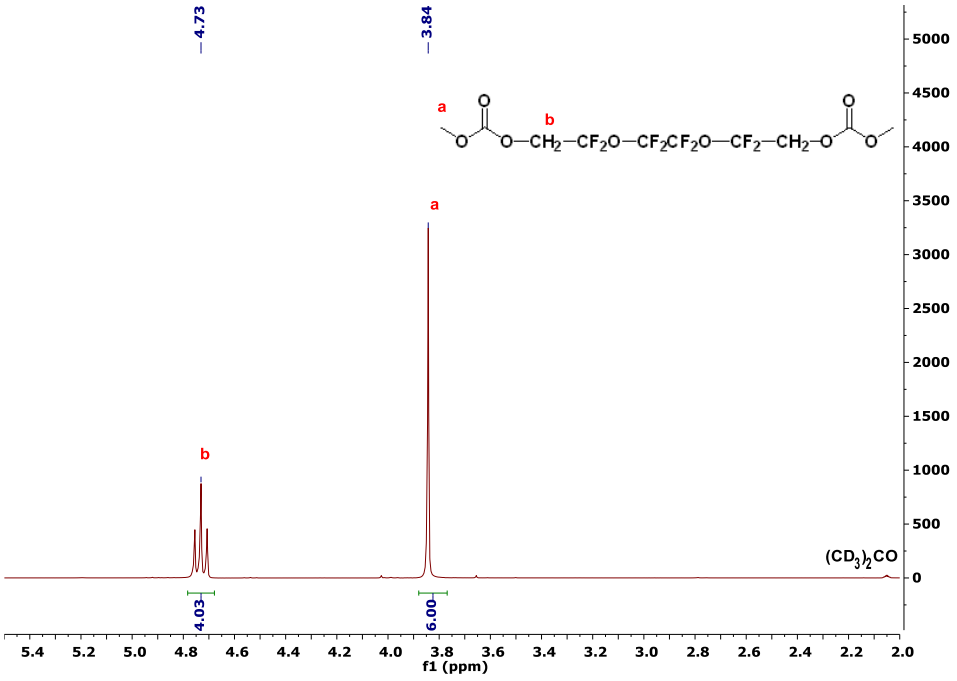

Figure 2.S1 NMR of C6-DMC in deuterated acetone.

Fig. 2.S2 shows ^{1}H NMR of the C8-DMC neat oligomer after synthesis and purification. The measurement was carried out in deuterated acetone. The peak at 3.84 ppm corresponds to the hydrogens attached to the methyl group while the peak at 4.77 ppm corresponds to the hydrogens

part of the backbone. The peak integration values, which are listed below each peak, correspond to the number of hydrogens contributing to that peak.

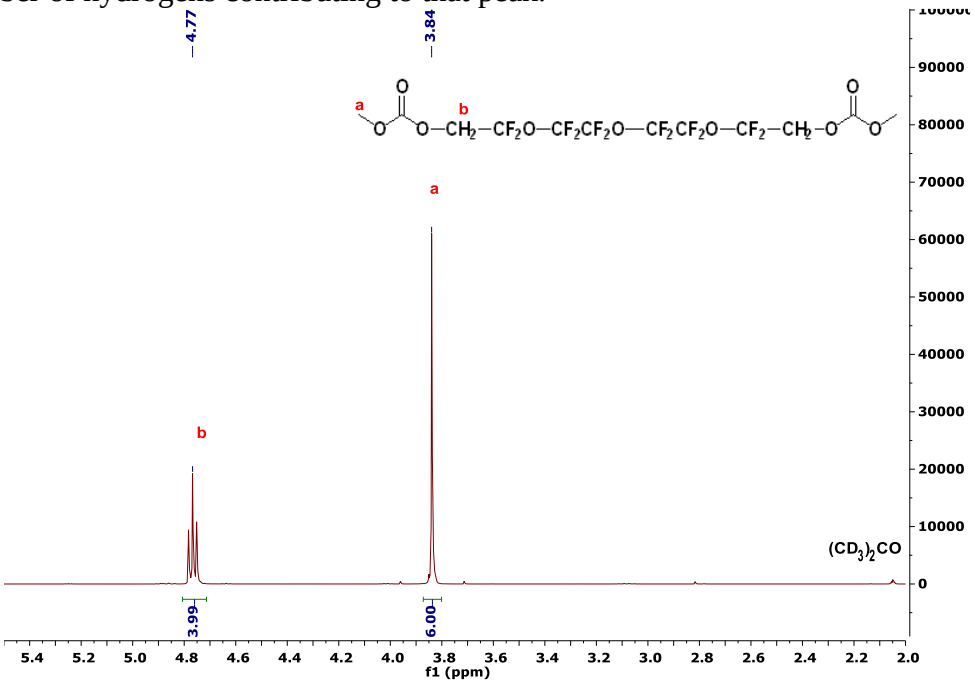

Figure 2.S2 NMR of C8-DMC in deuterated acetone.

2.5.2 Error Propagation

Error bars were obtained through error propagation, as shown in Eq. 2.S1, for $\kappa t_{+,id}$

$$\delta\kappa t_{+,id} = \left|\kappa t_{+,id}\right| \sqrt{\left(\frac{\delta\kappa}{\kappa}\right)^2 + \left(\frac{\delta t_{+,id}}{t_{+,id}}\right)^2} \tag{2.S1}$$

where $\delta\kappa t_{+,id}$, $\delta\kappa$, and $\delta t_{+,id}$ is the standard deviation of $\kappa t_{+,id}$, κ, and $t_{+,id}$, respectively.

2.6 Acknowledgements

This project is primarily funded by the National Science Foundation,grant Number 1505669, under the SusChEM initiative, which supported the work of D. B. S., A. K., and N. P. B. The work of K. R. O., S. J. M., and J. D. S. was supported as part of the Center for Mesoscale Transport Properties, an Energy Frontier Research Center supported by the U.S. Department of Energy, Office of Science, Basic Energy Sciences, under award #DE-SC0012673.

2.7 Nomenclature

κ	Conductivity of the electrolyte; (S/cm)
$t_{+,id}$	Ideal transference number determined by the steady-state current method

$\delta t_{+,id}$	Standard deviation in $t_{+,id}$
$\delta\kappa$	Standard deviation in κ; (S/cm)
A	Active surface area of electrode; (cm^2)
c	Ratio of conductivity between liquid cells and coin cells
I_{ss}	Steady-state current; (mA)
I_o	Initial current; (mA)
l	Thickness of separator; (cm)
L_c	Inductance of measurement cabling
Q_{el}	Constant phase element of the electrolyte
Q_{int}	Constant phase element of the interface
R_c	Resistance of measurement cabling; (Ω)
R_{el}	Resistance of electrolyte; (Ω)
R_{int}	Resistance of solvent/electrode interface; (Ω)
$R_{i,0}$	Resistance of solvent/electrode interface initially, prior to polarization; (Ω)
$R_{i,ss}$	Resistance of solvent/electrode interface when I_{ss} reached; (Ω)

3 Difference Between Approximate and Rigorously Measured Transference Numbers in Fluorinated Electrolytes[†]

3.1 Introduction

Developing next generation lithium-ion technology requires synergistic efforts ranging from electrode development to electrolyte engineering. Electrolytes used in current lithium-ion cells are typically mixtures of ethylene carbonate (EC), dimethyl carbonate (DMC) and lithium hexafluorophosphate ($LiPF_6$).[71–74] However, these electrolytes are highly flammable at room temperature; the flash point of DMC is 18 °C. The development of nonflammable electrolytes has thus garnered considerable attention. Electrolytes based on fluorinated solvents have been recently shown as interesting candidate materials for lithium-ion batteries.[31,45,46,75–77] While fluorinated additives are often used in lithium-ion technology to help stabilize the solid electrolyte interphase layer at the anode, the notion that a fluorinated solvent could serve as an electrolyte is relatively new.[78,79] These electrolytes exhibit larger electrochemical stability windows than alkyl carbonates.[45] The standard approach for quantifying ion transport in electrolytes comprises measurement of ionic conductivity, κ, using blocking electrodes. However, it is well established that complete characterization of a binary electrolyte (solvent + salt) requires measurement of two additional transport coefficients, the salt diffusion coefficient, D, and the transference number of the cation with respect to the velocity of the solvent, t_+^0, and the thermodynamic factor, T_f.[39,80]

The transference number of fluorinated electrolytes is of interest due to fundamental differences in solvent-salt interactions relative to conventional electrolytes. In conventional electrolytes such as alkyl carbonates, the salt-solvent interactions are dominated by associations between oxygen atoms on the solvent and lithium cations. Such associations are weakened in fluorinated electrolytes due to the electron withdrawing character of fluorine atoms. Instead, one might expect associations between the fluorinated solvent and the fluorinated anion due to the well-documented fluorous effect.[50,81] These interactions could result in an increase in the cation transference number, which, in turn, could improve the efficacy of fluorinated electrolytes. Interestingly, reported cation transference numbers of fluorinated electrolytes in the literature are as high as 0.9, compared with 0.4 or less in conventional electrolytes.[46,76,82–84] All of the cation transference numbers of fluorinated electrolytes reported in the literature are based on the assumption that the solutions are ideal. An ideal electrolyte is defined to be one that contains completely disassociated ions that do not interact with each other and this gives rise to activity coefficients that are unity and independent of molality. We use a symbol $t_{+,id}$ to refer to the transference number based on the ideal solution approximation. The method for measuring $t_{+,id}$ was pioneered by Bruce and Vincent.[53,54] The high ideal cation transference number is often taken as a signature of rapid diffusion of the cation relative to the anion. A standard approach for measuring the self-diffusion coefficient of the ions is pulsed field gradient NMR (PFG-NMR).[48,85–88] If the ideal solution assumption were valid, then $t_{+,NMR}$ and $t_{+,id}$ would be in quantitative agreement.

[†] This chapter is reported in Shah, D. B., *et al*. Difference between approximate and rigorously measured transference numbers in fluorinated electrolytes. *Phys. Chem. Chem. Phys.* **2019**, *21*, 7857 – 7866.

The purpose of this paper is to report on the complete electrochemical characterization of a fluorinated electrolyte including measurement of κ, D, t_+^0 and T_f. The chemical structures of the fluorinated solvent, C8-DMC, is shown in Fig. 3.1a and that of the FSI anion is shown in Fig. 3. 1b. Pulsed field gradient NMR experiments were used to quantify self-diffusion coefficients of the cations and anions in this fluorinated electrolyte. We show that the rigorously measured transference number, t_+^0, differs qualitatively from that obtained using the ideal solution approximation.

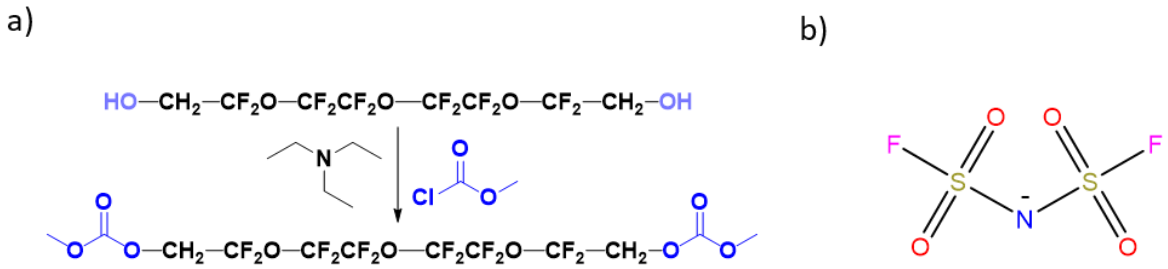

Figure 3.1 (a) Reaction to produce C8-DMC from the commercial C8-Diol analog and (b) FSI anion.

3.2 Experimental Details

3.2.1 Perfluoroether Synthesis

The perfluoroether (PFE) was synthesized from a diol terminated precursor following procedures described in Wong, D. *et al.* and Olson, K. *et al.*[31,49] Fig. 3.1a shows our approach to synthesize C8-DMC. 0.10 mol of the perfluorinated glycol precursor (0.20 mol -OH end groups) and three molar equivalents triethylamine (84 mL, 0.60 mol) were dissolved in 400 mL of 1,1,1,3,3-pentafluorobutane in a 1 L 3-neck round-bottom flask. The solution was cooled to 0°C under nitrogen atmosphere using a salt + ice bath. Methyl chloroformate (46 mL, 0.60 mol) was added dropwise over the course of two hours with rapid stirring, resulting in significant gas evolution and formation of the white triethylamine hydrochloride (TEA HCl) precipitate. The reaction was stirred overnight under nitrogen atmosphere at ambient temperature, and reaction completion was confirmed by proton nuclear magnetic resonance (^{1}H-NMR).

The TEA HCl salt was removed by gravity filtration, yielding a pale-yellow solution. The salt was washed three times with 50 mL 1,1,1,3,3-pentafluorobutane to remove residual product. The combined pentafluorobutane solution was then washed 3x with 500 mL water and 1x with 500 mL brine using a separatory funnel. The solution was stirred with activated carbon to remove coloration and dried with magnesium sulfate. After filtering the solids, pentafluorobutane was removed under reduced pressure, yielding a clear oil. The dimethyl carbonate terminated perfluorinated tetraethylene ether (C8-DMC) was dried under vacuum at 50°C for two days. The molecular weight (MW) for C8-DMC is 526 g/mol. Figs. 3.S1a and 3.S1b in the supplemental

information show the ^{1}H-NMR spectra of the precursor and product dissolved in deuterated acetone.

Thermogravimetric analysis (TGA) was used to determine the volatility of C8-DMC using a TA Instruments Q5000 TGA under nitrogen flow (10 mL/min) from 25 °C to 500 °C at a heating rate of 10 °C/min. The temperature at which a 5% mass loss were recorded from the TGA curve was 129 °C for C8-DMC. Closed-cup flash point measurements were performed using an Erdco Rapid Tester small-scale apparatus following ASTM D 3278. No flash point was detected for C8-DMC within the experimental window (up to 250°C).

3.2.2 Salts

Lithium bis(fluorosulfonyl)imide (LiFSI) (cat. no. 097602) was purchased from Oakwood Products, Inc. The salt was ≥ 99% pure, as confirmed by a Certificate of Analysis form. The salt was dried at 100 °C under dynamic vacuum for three days inside a glovebox antechamber. The salt, oligomer, and electrolytes were stored within an argon filled Vac glovebox with H_2O and O_2 concentrations kept below 1 ppm.

3.2.3 Electrolyte Preparation

Prior to transfer into the glovebox, C8-DMC was dried under active vacuum inside the glovebox antechamber at 50 °C for 72 hours. In order to form electrolytes, a predetermined amount of Li salt was added to a known mass of C8-DMC. Once the salt was added, the electrolytes were placed on a magnetic stirrer and were allowed to mix for 12 hours or more using a magnetic stir bar.

3.2.4 Experimental Characterization

All experiments were conducted at 30 °C ± 1 °C. Coin cells were run in heating ovens and concentration cells were immersed in a temperature controlled oil bath. All the error bars reported are standard deviations of replicate measurements. Error propagation formulas for relevant measurements are reported in supplemental information.

Conductivity measurements

Conductivity samples were prepared by sandwiching an electrolyte soaked separator, Celgard 2500 (Celgard Company), with a stainless steel shim (MTI Corporation) on either side. The stainless steel shims were 15.5 mm in diameter and 0.2 mm in thickness; Celgard 2500 was cut to 19 mm in diameter and had a thickness of 25 μm. The stack was placed into CR2032 coin cells (Pred Materials) that were than hermetically sealed. Three replicate cells were produced and measured for each electrolyte. Conductivity data was collected through ac impedance spectroscopy performed on a Bio-Logic VMP3 potentiostat. The frequency range analyzed was between 1 MHz and 100 mHz at an amplitude of 60 mV. Fig. 3.2a shows typical impedance data

collected in coin cells and the equivalent circuit is shown in the inset. Here, R_s is the resistance of the electrolyte/separator composite, Q and Q_{int} are the constant phase elements associated with the electrolyte/separator and interface, respectively, and R_c and L_c are the resistance and inductance, respectively, associated with the VMP3 cables. The conductivity of the electrolytic phase, κ, was calculated using Eq. 3.1

$$\kappa = \frac{\tau}{\phi_c}\frac{l}{R_s A} \tag{3.1}$$

where A is the electrode area of the coin cells in cm^2, l is the thickness of the separator in cm, τ is the tortuosity of the separator and ϕ_c is the volume fraction of the conducting element within the separator. Both τ and ϕ_c are experimentally determined, and the ratio was determined by measuring the conductivity of five electrolytes using a FiveEasy Conductivity Meter F30 (Mettler Toledo) and dividing the obtained conductivity values by the separator conductivities. The five molalities measured using the conductivity probe were 0.28, 0.60, 0.94, 1.30 and 1.78 mol LiFSI/kg C8-DMC and $\frac{\tau}{\phi_c}$ was found to be 8.47 ± 0.69.

The conductivity of neat C8-DMC solvent was measured to be 3.02×10^{-7} S/cm, which we assume is due to impurities. We treat this value as a background and report the conductivity of our electrolytes after subtracting 3.02×10^{-7} S/cm from the measured values.

The cell constant, $\frac{\tau}{\phi_c}$, is also known as the MacMullin number, N_m

$$N_m = \frac{\tau}{\phi_c} = \frac{\kappa}{\kappa_s} \tag{3.2}$$

where κ_s is the separator conductivity.[89] The volume fraction was calculated following a similar procedure to that of reference 90. In order to calculate the porosity of the Celgard 2500 separator, 5 replicate uptake volume measurements for each salt molality were done. The average conducting phase volume fraction was found to be 0.535 ± 0.030 across the range of salt molalities. The density, ρ, at each salt concentration was obtained by filling a differential scanning calorimetry (DSC) sample pan (TA Instruments) with a known volume of 40 uL and measuring the mass of the electrolyte at 30 °C; three replicates were measured at each salt concentration. Results are shown in Table 3.1.

The MacMullin number was combined with the conducting phase volume fraction in order to calculate the separator tortuosity, τ = 4.53 ± 0.45.

Table 3.1 Values of LiFSI wt %, molality, calculated concentration, and measured density for C8-DMC electrolytes.

LiFSI wt%	*m* (mol/kg)	*c* (mol/L)	ρ (g/L)
0	0	0	1459 ± 64
1.0	0.05	0.08	1487 ± 26
5.0	0.28	0.39	1447 ± 72
10.0	0.60	0.89	1660 ± 17
14.9	0.94	1.36	1681 ± 24
19.6	1.30	1.70	1627 ± 75
25.0	1.78	2.36	1764 ± 14

Lithium symmetric cells for ideal transference number

Lithium symmetric cells were assembled similar to conductivity samples. However, instead of stainless steel shims, lithium discs, cut from lithium chips (MTI Corp.), were used on either side of the electrolyte-soaked Celgard. The diameter of the 150 μm thick Li disc was 12.7 mm. Three replicate cells were produced for each electrolyte. Data were collected on a Bio-Logic VMP3 potentiostat. Each sample cell was subjected to a conditioning treatment, which consisted of charge and discharge cycles at 0.02 mA/cm^2 in order to help stabilize the interfacial layer. The sequence performed was a 4 hour charge, 30 minutes rest, a 4 hour discharge, 30 minutes rest, and repeated for a total of 6 times. Ac impedance was carried out before the beginning of conditioning, after each rest step, and at the end of conditioning. Each sample was then polarized at ΔV = ± 40 mV and ± 80 mV for 1 hour in order to ensure that the ideal transference number, $t_{+,id}$, collected was independent of the applied potential, an important consideration since the method assumes that minimal concentration gradients develop over the course of the measurement. During chronopotentiometry, current was measured at 1 second intervals in order to capture the full current response. Ac impedance data were collected every 20 minutes with an ac amplitude of 20 mV and 40 mV for the dc applied potentials of ± 40 mV and ± 80 mV, respectively. The data obtained for all of these cases were similar. We report data acquired using ac impedance spectroscopy with an amplitude of 20 mV during dc polarization of 40 mV in Fig. 3.2b. Data were modeled to the equivalent circuit shown in the inset of Fig. 3.2b, where R_{int} is the interfacial impedance. Fig. 3.2b represents the typical impedance data seen for Li symmetric cells.

Assuming Ohm's law, which is a reasonable assumption prior to cell polarization due to a lack of concentration gradients, an initial current, I_Ω, is given by Eq. 3.3:

$$I_\Omega = \frac{\Delta V}{R_T} \tag{3.3}$$

where ΔV is the applied polarization potential and R_T is the total initial cell resistance as measured by ac impedance spectroscopy. Eq. 4 was then used to calculate the ideal transference number:[54,91]

$$t_{+,id} = \frac{I_{ss}}{I_\Omega}\left(\frac{\Delta V - I_\Omega R_{i,0}}{\Delta V - I_{ss}R_{i,ss}}\right) \tag{3.4}$$

where I_{ss} is the steady state current, $R_{i,0}$ is the initial interfacial resistance, and $R_{i,ss}$ is the interfacial resistance when I_{ss} is reached.

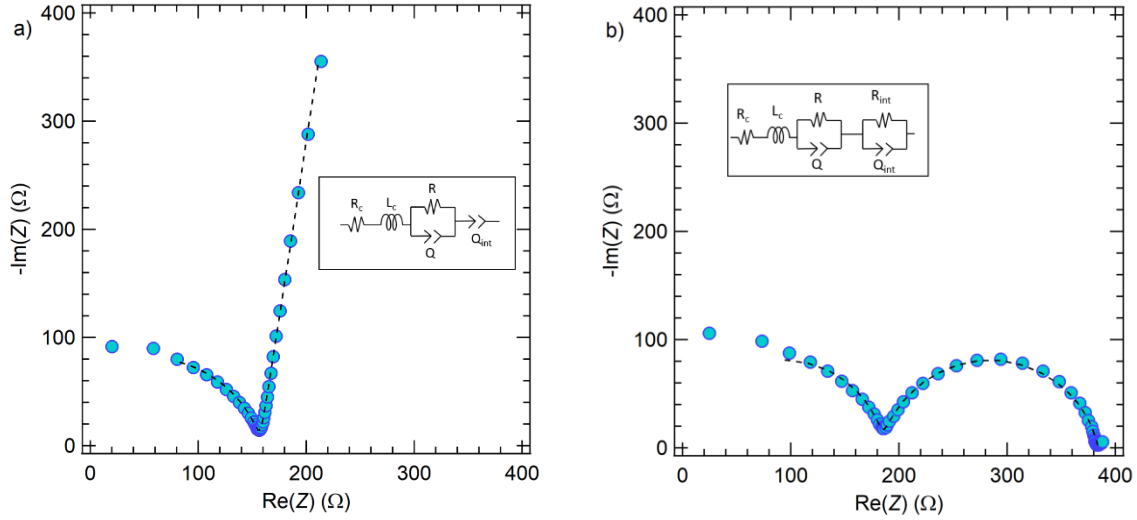

Figure 3.2 Ac impedance data of C8-DMC/LiFSI at m = 0.60 mol/kg at T = 30 °C. (a) A symmetric cell with stainless steel (blocking) electrodes (data shown to 250 Hz for clarity) and (b) a symmetric cell with lithium (non-blocking) electrodes. The dashed black lines are fits to the equivalent circuits shown.

Restricted diffusion measurements

Diffusion coefficients were measured using the restricted diffusion technique.[89,90] Lithium electrodes (thickness 150 μm, diameter 12.7 mm) sandwiched electrolyte soaked Celgard 2500 separators (thickness 25 μm). Four dc potentials, ±40 mV and ±80 mV, were used to polarize the cell until a steady-state current was realized. The potential was then removed and the cells were allowed to relax for 2 hours while the open-circuit potential, U, was measured every 5 seconds. Porous separators were used in order to control for convection, an important precaution for liquid electrolytes.[91] Three configurations were used, with 5, 10 and 15 separators stacked to adjust the thickness of the electrolyte. The three thicknesses, combined with four dc potentials resulted in 36 independent diffusion coefficient measurements for each salt concentration. The open circuit relaxation potential was analyzed, and representative relaxation profiles for m = 0.60 mol/kg can be seen in Fig. 3.3 for all three electrolyte thicknesses. The relaxation profiles were fit to Eq. 3.5

$$U(t) = k_0 + ae^{-bt} \tag{3.5}$$

where a and b are fit parameters and k_0 is an empirically determined offset voltage. The salt diffusion coefficient within the separator, D_s, is related to b by

$$D_s = \frac{l^2 b}{\pi^2} \tag{3.6}$$

where l is the thickness of the separator stack. The lower time limits of the fits are such that $\alpha = D_s t/l^2 > 0.05$.[92]

This paper reports the diffusion coefficient of the salt in the electrolytic phase, D, and in order to do so, the tortuosity of the separator had to be taken into consideration:

$$D = \tau D_s \tag{3.7}$$

where D_s is the measured diffusion coefficient within the separator.

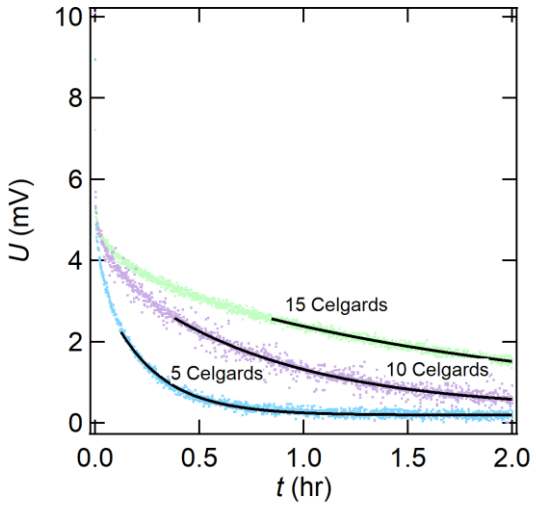

Figure 3.3 Open circuit potential versus time after dc polarization of 40 mV of a C8-DMC/LiFSI electrolyte with m = 0.60 mol/kg in lithium-electrolyte-lithium cells with Celgard 2500 separators. The number of Celgard 2500 separators was varied to obtain different electrolyte thicknesses. Salt diffusion coefficients are extracted by fitting the data to Eq. 3.5 (solid black curves). The diffusion coefficients obtained from the different fits are in good agreement (1.86 x 10^{-8} (α = 0.051), 2.39 x 10^{-8} (α = 0.051), 2.39 x 10^{-8} (α = 0.050) cm^2/s for 5, 10 and 15 stacked Celgards, respectively).

Concentration cells

In order to gather information on the electrolytes' thermodynamic factor, concentration cells were made. A U-cell design, similar to what is found in Stewart et al., was custom made by Adams & Chittenden.[93] A porous glass frit separated the two sides of the U-cell, and care was taken to ensure that mixing did not occur between the two halves. Two glass frits of different pore size were used: one with pore sizes ranging from 10 – 16 μm and another ranging from 1.0 – 1.6 μm. One side of the U-cell contained a reference electrolyte of m_{ref} = 0.60 mol/kg, while

the other side was filled with electrolytes of varying molalities. Both sides of the U-cell were filled with electrolyte such that the heights on both sides were the same, an effort necessary to minimize pressure differences across the glass frit. Strips of lithium (MTI Corp.) were cut and brushed, and then immersed into the two halves of the U-cell. The open-circuit potential, *U*, was monitored with time. The open-circuit potential was monitored for 1 hour, in which the potential plateaued for the entirety of the measurement, further confirming that electrolyte mixing did not occur within the measurement time frame. The potential difference is related to the thermodynamic factor by the following equation:[39]

$$\frac{F(z^+v^+)}{vRT(1-t_+^0)}\frac{dU}{dlnm} = 1 + \frac{dln\gamma_\pm}{dlnm} \tag{3.8}$$

where z^+ is the charge number, v^+ is the number of cations, both of which are 1 for LiFSI, and $\frac{dU}{d\ln m}$ is the change in the open-circuit potential, *U*, with ln(*m*).

Transference number calculation

The transference number of the electrolytic phase, t_+^0, was then calculated by combining the above four independent measurements (conductivity, ideal transference number, concentration cells, and restricted diffusion). Balsara and Newman showed that the ideal transference number is related to the cation transference number[70]

$$t_+^0 = 1 - \sqrt{\frac{\frac{F^2\phi_c D_s c}{v\kappa_s RT}\left(\frac{1}{t_{+,id}}-1\right)}{1+\frac{dln\gamma_\pm}{dlnm}}}. \tag{3.9}$$

Here, *v* is related to the stoichiometric factor and is equal to 2 for a monovalent salt. The volume fraction of the conducting phase, ϕ_c, must also be included if the separator conductivity, κ_s, and separator salt diffusion coefficient, D_s, are used since t_+^0 is a property of only the electrolytic phase. By combining Eq. 3.9 with Eq. 3.8, the thermodynamic factor can be determined with experimentally measurable quantities

$$\frac{\kappa_s(z^+v^+)}{vRT\phi_c D_s c\left(\frac{1}{t_{+,id}}-1\right)}\left(\frac{dU}{dlnm}\right)^2 = 1 + \frac{dln\gamma_\pm}{dlnm}. \tag{3.10}$$

Eq. 3.10 is slightly different from similar equations used by us to analyze data.[94,95] The main difference is that the $\frac{dU}{\mathrm{d}\ln m}$ term in Eq. 3.10 is squared. The sign of the open circuit potential depends on convention – some researchers report positive values for *U*, while others report negative values for *U*.[70,93,95,96] This depends on whether the positive or negative lead from the potentiostat is connected to the reference electrolyte. Eq. 3.10 is applicable regardless of convention or how the potentiostat is connected to the reference electrolyte. Once the

thermodynamic factor is calculated, t_+^0 can be determined. Additionally, the above equation is true for all concentrations, as there are no assumptions about ideality within the calculation of t_+^0.

Pulsed field gradient NMR

NMR samples were prepared in an argon glovebox using 5 mm tubes with high-pressure caps. Self-diffusion coefficients were measured on a Bruker Avance 600 MHz instrument with a Z-gradient direct detection broad-band probe and a variable temperature unit maintained at 30 °C throughout the experiments. Measurements were performed on ^{7}Li at 233 MHz and ^{19}F at 565 MHz to probe the diffusion of the lithium cations and fluorine-containing FSI anions. The peak at 50 ppm is assigned to the FSI anion (see Fig. 3.S2a and 3.S2b in supplemental information). The T_1 of each peak was measured using inversion recovery, and a recycle delay of at least 4 times T_1 was used in diffusion measurements. For all samples containing less than m = 1.30 mol/kg, a double stimulated bipolar gradient pulse sequence (Bruker sequence dstebpgp3s) was used to correct for convection in the sample.[97,98] Because of the lower signal intensity in more concentrated electrolytes, a longitudinal delay eddy current delay without convection compensation was used (Bruker sequence stebpgp1s). Experiments were performed with a variety of diffusion delays and pulse lengths to confirm that convection was not a source of inaccuracy in these samples. Diffusion intervals, Δ, varied from 0.5 to 1 s (^{7}Li) and 0.07 to 0.15 s (^{19}F), and pulse lengths, δ, varied from 16 to 40 ms (^{7}Li) and 2 to 11 ms (^{19}F). For the dstebpgp3s program, the signal attenuation, E, was fit to

$$E = e^{-\gamma^2 g^2 \delta^2 D_i (\Delta - \frac{5\delta}{8} - \tau_d)} \tag{3.11}$$

where γ is the gyromagnetic ratio, g is the gradient strength, D_i is the self-diffusion coefficient of species i, and τ_d is the delay for gradient recovery. For the stebpgp1s program, the signal attenuation was fit to

$$E = e^{-\gamma^2 g^2 \delta^2 D_i (\Delta - \frac{\delta}{4})}. \tag{3.12}$$

For both pulse programs, corrections for sine-shaped gradients were included.[99] 32 experiments with varying gradient strength, g, were performed for each diffusion coefficient measurement, always resulting in a linear signal attenuation on the Stejskal-Tanner plot. An example of the Li PFG-NMR data for a diffusion time of 0.1 s is shown in Fig. 3.S3, which shows the ln(E) vs $\gamma^2 g^2 \delta^2 D_i (\Delta - \frac{5\delta}{8} - \tau_d)$. All parameters on the x-axis are known, thus the magnitude of the slope is the self-diffusion coefficient of Li, D_{Li}.

3.3 Results and Discussion

The electrochemical characterization experiments were conducted on C8-DMC/LiFSI mixtures contained within one or more Celgard 2500 separators. Our objective is to extract the properties of the C8-DMC/LiFSI electrolyte from these measurements. The ionic conductivity of the electrolytic phase, κ, is extracted from the raw data using Eq. 3.1, which accounts for the

tortuosity of the separator, τ, and the volume fraction of the conducting phase in the separator, ϕ_c. The salt diffusion coefficient of the electrolytic phase, *D*, is extracted from the raw data obtained from restricted diffusion experiments using Eq. 3.6 – 3.8; only tortuosity affects *D*. The ideal transference number, $t_{+,id}$, is obtained from the raw data with no corrections for the presence of a separator. Obviously, the open circuit potential, *U*, obtained from concentration cells (U-cell) is not corrected for tortuosity or porosity because the U-cell contains only liquids. However, the relationship between the thermodynamic factor and *U* contains a volume fraction correction, given by Eq. 3.10 when values of the salt diffusion coefficient and conductivity obtained from separator/electrolyte systems are used. Similarly, the expression for t_+^0 also contains volume fraction corrections, as shown in Eq. 3.9. Electrolyte properties thus obtained, κ, *D*, $t_{+,id}$, and *U* are plotted as a function of molality in Figs. 3.4a – d.

Fig. 3.4a indicates that at low concentrations, conductivity increases dramatically with increasing salt concentration, going through a shallow maximum of 8.49 x 10^{-5} S/cm at m = 0.94 mol/kg. The maximum concentration studied was m = 1.78 mol/kg (25 wt% LiFSI); the solution with m = 2.31 (30 wt% LiFSI) was phase separated, and the solubility limit was taken as the average between these two molalities, which was m = 2.03.[76] The salt diffusion coefficient of our perfluoroether-based electrolytes, shown in Fig. 3.4b, monotonically decreases with increasing salt concentration. Over the accessible concentration range, *D* decreases by about an order of magnitude. It is perhaps worth noting that *D* in other ether-based solvents follow different behavior. For example, in poly(ethylene oxide)-based electrolytes, *D* is more or less independent of salt concentration over the same concentration window.[94,95] Fig. 3.4c is a plot of the ideal transference number vs. salt concentration. At the lowest concentration, $t_{+,id}$ is 0.97 which is remarkably close to unity. If our electrolytes were thermodynamically ideal, the near unity transference number would imply that the cation is much more mobile than the anion. As concentration increases, $t_{+,id}$ decreases monotonically to a value of 0.67 at m = 1.30. The fact that $t_{+,id}$ is greater than 0.5 everywhere suggests that the cation is more mobile throughout our concentration window. In conventional liquid electrolytes, $t_{+,id}$ is generally less than 0.5 at all salt concentrations.[68] A high $t_{+,id}$ is thought to be a desirable characteristic for electrolytes, as that reduces concentration overpotential. However, this is only true if the electrolyte is thermodynamically ideal. In Fig. 3.4d, the open circuit potential for concentration cells is shown in blue as a function of the natural log of salt molality. The potential equals zero when both sides of the U-cell contain the reference electrolyte (m = 0.60 mol/kg). A polynomial fit to the open circuit potential is shown in solid blue circles, and follows the equation, shown as a solid blue line:

$$U(m) = -1.896(\ln m)^4 - 11.761(\ln m)^3 - 23.298(\ln m)^2 - 32.681 \ln m - 12.928. \quad (3.13)$$

If the solution were thermodynamically ideal, then *U* would be given by the Nernst potential

$$U(c) = -\frac{RT}{F} \ln\left(\frac{c}{c_{ref}}\right), \quad (3.14)$$

and Table 3.1 is used to convert concentrations to molality and c_{ref} = 0.89. The open circles and dashed line in Fig. 3.4d represent the Nernst potential.

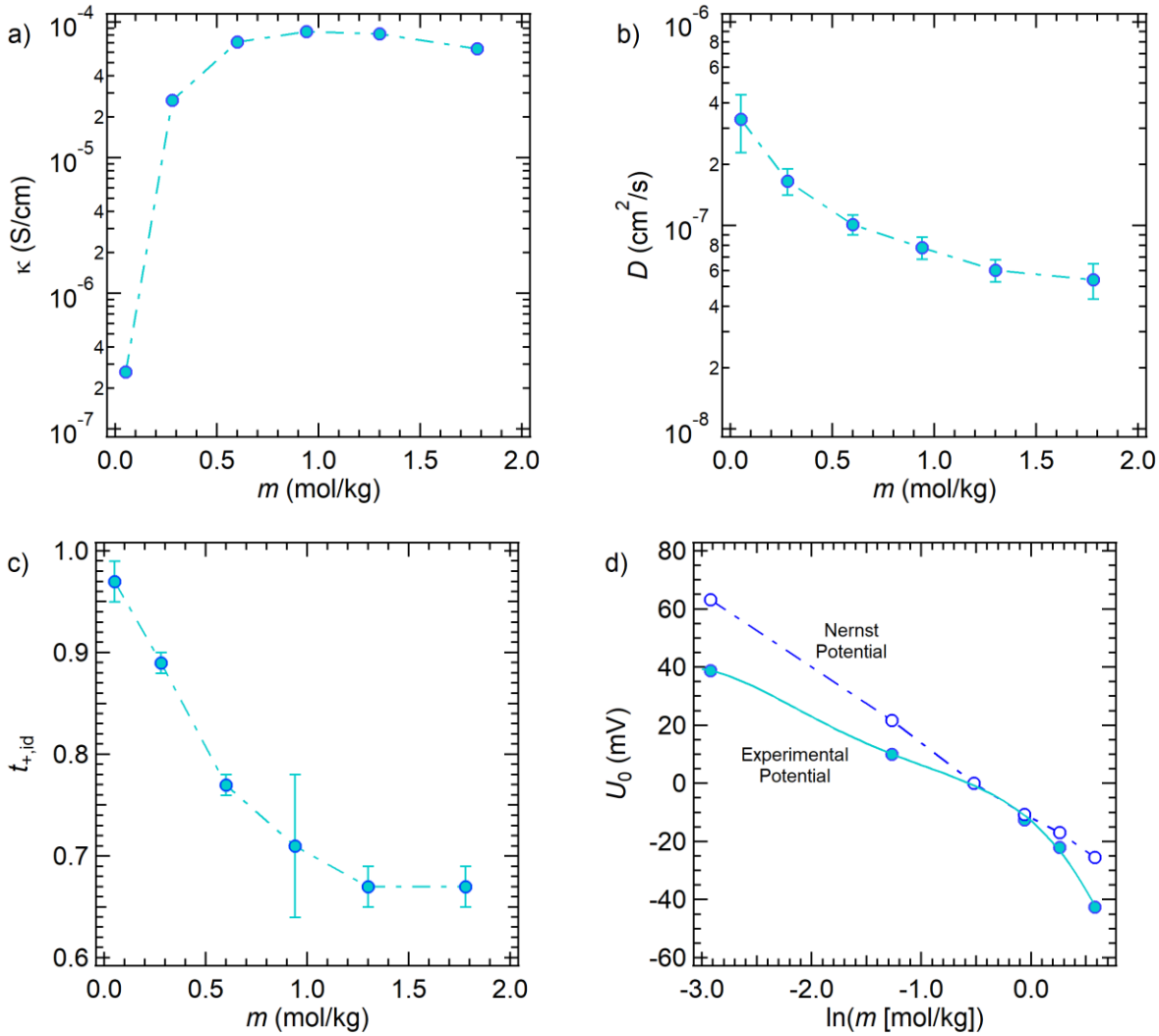

Figure 3.4 Electrochemical properties of C8-DMC/LiFSI (electrolytic phase) as a function of molality. **(**a) The conductivity measured by ac impedance, (b) the diffusion coefficient measured by the restricted diffusion method, and (c) $t_{+,id}$ as measured by the steady-state current method. d) Results obtained in concentration cells with m_{ref} = 0.60 mol/kg (solid symbols). The solid line is a fit through the experimental data (Eq. 3.13). The open symbols and dashed line give the Nernst potential (Eq. 3.14).

The thermodynamic factor, $1 + \frac{dln\gamma_{\pm}}{dln\mathrm{m}}$, calculated using Eq. 3.10 and the data shown in Fig. 3.4, is plotted as a function of concentration in Fig. 3.5. It increases monotonically with salt concentration. The transference number, t_+^0, calculated using Eq. 3.9 and the data shown in Fig. 3.4, is plotted as a function of salt concentration in Fig. 3.6. Interestingly, t_+^0 is negative over the entire experimental window. (At the lowest salt concentration, m = 0.05, our approach indicates that t_+^0 is -10.8. The raw data were relatively noisier at this concentration, probably due to low conductivity.)

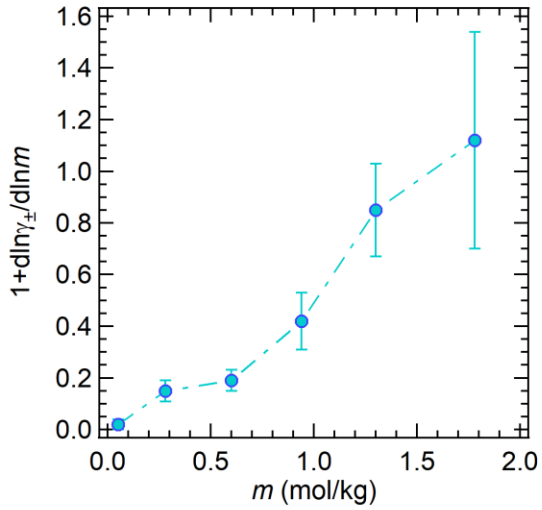

Figure 3.5 The thermodynamic factor as a function of salt concentration.

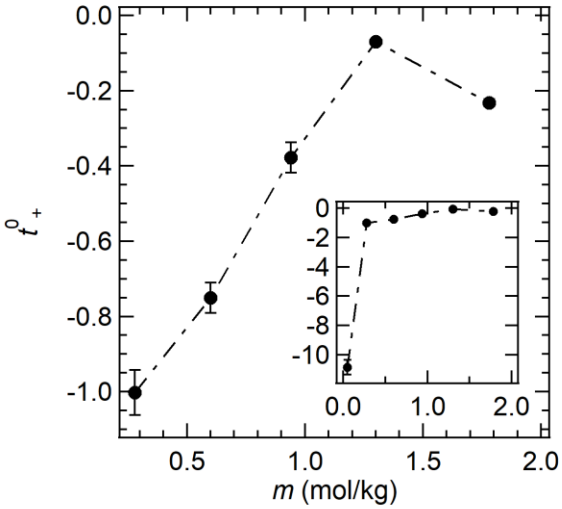

Figure 3.6 Transference number, t_+^0, based on concentrated solution theory as a function of salt concentration in the range m = 0.28 to 1.78 mol/kg. The inset includes data at a very low concentration, m = 0.05 mol/kg. The rest of the paper will focus on the range m = 0.28 to 1.78 mol/kg.

In Fig. 3.7, the self-diffusion coefficients of the lithium cation, D_{Li}, and the fluorinated anion, $D_{FSI,}$ measured by PFG-NMR are plotted as a function of salt concentration. These diffusion coefficients are sensitive functions of salt concentrations, decreasing by a factor of 30 over our concentration window. However, the self-diffusion coefficients for both species are approximately the same at all salt concentrations, suggesting that their motion is coupled.

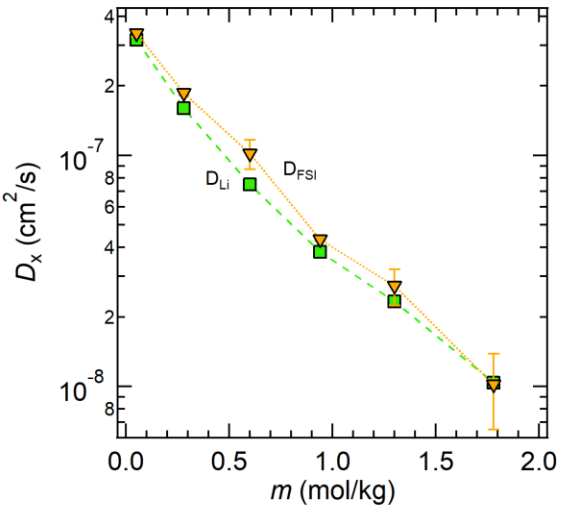

Figure 3.7 Self-diffusion coefficients of Li and FSI determined by PFG-NMR as a function of salt concentration. D_{FSI} and D_{Li} are very similar throughout the concentration window.

The Nernst-Hartley relation is often used to obtain an overall salt diffusion coefficient from PFG-NMR experiments and is usually defined as:[100–102]

$$D_{NMR} = \frac{2D_{Li}D_{FSI}}{D_{Li} + D_{FSI}} \tag{3.15}$$

However, it should be noted that Eq. 3.15 is only applicable to dilute electrolytes comprising completely disassociated ions. Fig. 3.8 compares D_{NMR} with D; D is the salt diffusion coefficient measured by restricted diffusion. At the lowest concentration, m = 0.28 mol/kg, the two diffusion coefficients are within experimental error. Both diffusion coefficients decrease monotonically with salt concentration. It is evident that D_{NMR} is a more sensitive function of concentration than D.

Analogous to Eq. 3.15, a transference number based on NMR measurements is usually defined as:

$$t_{+,NMR} = \frac{D_{Li}}{D_{Li} + D_{FSI}}. \tag{3.16}$$

As was the case with Eq. 3.15, Eq. 3.16 is only applicable to dilute electrolytes comprising completely disassociated ions.

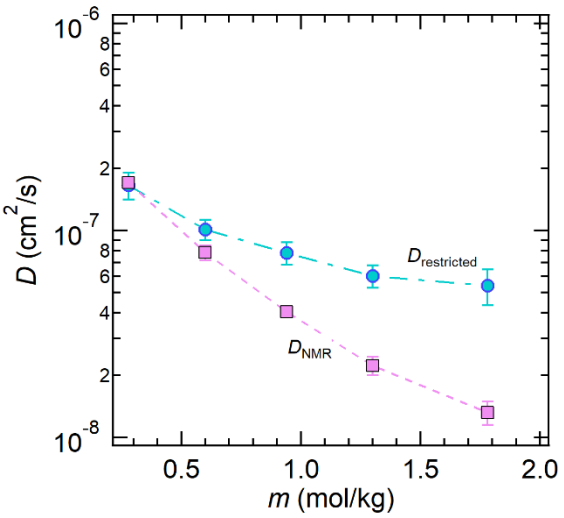

Figure 3.8 Dependence of the salt-diffusion coefficients measured by PFG-NMR and restricted diffusion on salt concentration.

We conclude this section by comparing three different measurements of the transference number. Fig. 3.9 compares shows $t_{+,\mathrm{id}}$ in blue, $t_{+,\mathrm{NMR}}$ in red, and t_+^0 in black. Focusing on the data at m = 0.28 mol/kg, $t_{+,id}$ = 0.89. Based on the value of $t_{+,id}$ alone, one might have concluded that the cation is much more mobile than the anion. However, at m = 0.28 mol/kg, $t_{+,NMR}$ = 0.48, suggesting that the cation and the anion are equally mobile. These two conclusions are clearly inconsistent with each other. Interpretations presented above are only true if the salt had disassociated into Li^+ and FSI^- ions that migrated independently of each other. The inconsistency indicates that the migration of Li+ and FSI- are not independent. The nature of ion motion in our electrolytes is complex and captured by full electrochemical characterization. At m = 0.28 mol/kg, t_+^0 = -1.0. The negative value of t_+^0 implies that when a field is applied to an electrolyte with uniform composition, both the Li^+ and FSI^- are driven to the positive electrode. This can only happen if the solution contains charged clusters such as $[Li(FSI)_2]^-$ in addition to other charged species such as Li^+ and FSI^-. It is possible that the observation that D_{Li} and D_{FSI} measured by PFG-NMR are similar due to the fact that most of the ions are present in the form of clusters. The stark differences between $t_{+,NMR}$, $t_{+,id}$ and t_+^0 are noteworthy. The NMR transference number, $t_{+,NMR}$, is positive and independent of concentration. The ideal transference number, $t_{+,id}$, is positive and a monotonically decreasing function of concentration. In contrast, the rigorously defined transference number, t_+^0, is negative and an increasing function of concentration, suggesting the presence of ion clusters in all of the electrolytes we studied.

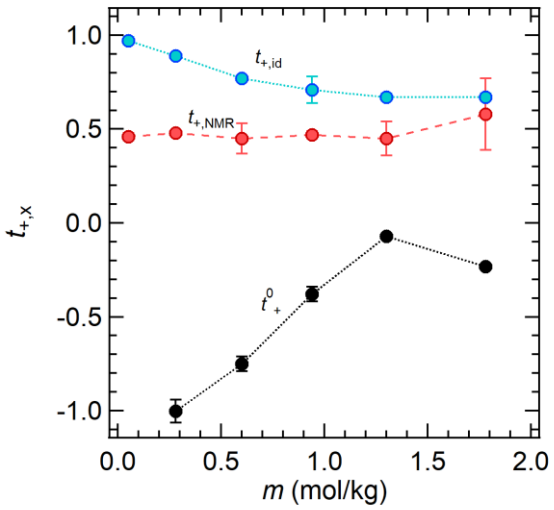

Figure 3.9 The cation transference numbers measured by the steady-state current method, $t_{+,id}$, and PFG-NMR, $t_{+,NMR}$, are compared with the rigorously defined transference number based on concentrated solution theory, t_+^0, at different salt concentrations. The lack of agreement between the three measurements indicates the presence of ion clusters.

3.4 Conclusion

We have measured the electrochemical properties of a fluorinated electrolyte comprising LiFSI dissolved in a perfluoroether solvent (C8-DMC). Conductivity, κ, was measured by ac impedance, the salt diffusion coefficient, D, was measured by restricted diffusion, and the transference number based on the ideal solution assumption, $t_{+,id}$, was measured using the steady-state current method. The open circuit potential measured in concentration cells, U, was combined with the three measurements described above to obtain the transference number, t_+^0. The equations used to determine t_+^0 are based on concentrated solution theory of Newman, which is applicable to all electrolytes, whether they are ideal or not. The self-diffusion coefficients of Li and FSI were measured by PFG-NMR, and these results give a third measure of the transference number, $t_{+,NMR}$. If all of the salt molecules were dissociated into free Li+ and FSI-, then the three transference numbers are expected to be identical (within experimental error). The data obtained from LiFSI/C8-DMC mixtures differ qualitatively from this expectation. The rigorously defined transference number, t_+^0, is negative across all salt concentrations, and it increases with increasing salt concentration. In contrast, the ideal transference number, $t_{+,id}$, is positive across all salt concentrations and it decreases with salt concentration. The most surprising result is obtained in the dilute limit at m = 0.28 mol/kg where $t_{+,id}$ = 0.89 which suggests that the electrolyte is a single ion conductor,[7,15] while the rigorously defined transference number, t_+^0, at this concentration is -1.0. It is evident that in fluorinated electrolytes, $t_{+,id}$ does not provide direct insight into the relative contribution of cations to the overall cell current. The NMR-based transference number, $t_{+,NMR}$, is approximately 0.5, independent of salt concentration.

When an electric field is applied to a solution of uniform concentration, comprised of fully dissociated anions and cations, the positive ion will migrate toward the negative electrode and the negative ion will migrate toward the positive electrode. In this case, $t_{+,id}$ and $t_{+,NMR}$, which by definition are always positive, provide insight into the relative mobilities of the dissociated cation and anion. Our measurements of negative t_+^0 imply that applying an electric field in an LiFSI/C8-DMC solution results in the migration of both Li+ and FSI- towards the positive electrode. This implies the presence of charged clusters. Further experimental and theoretical work is needed to quantify the nature of charged (individual ions, triplets, etc.) and uncharged species (ion pairs, quadruplets, etc.) in solution.

3.5 Supplemental Information

3.5.1 ^{1}H NMR Spectra

Fig. 3.S1a shows the ^{1}H NMR of the precursor C8-Diol dissolved in deuterated acetone. Fig. 3.S1b is the ^{1}H NMR of the product, C8-DMC, after synthesis and purification dissolved in deuterated acetone.

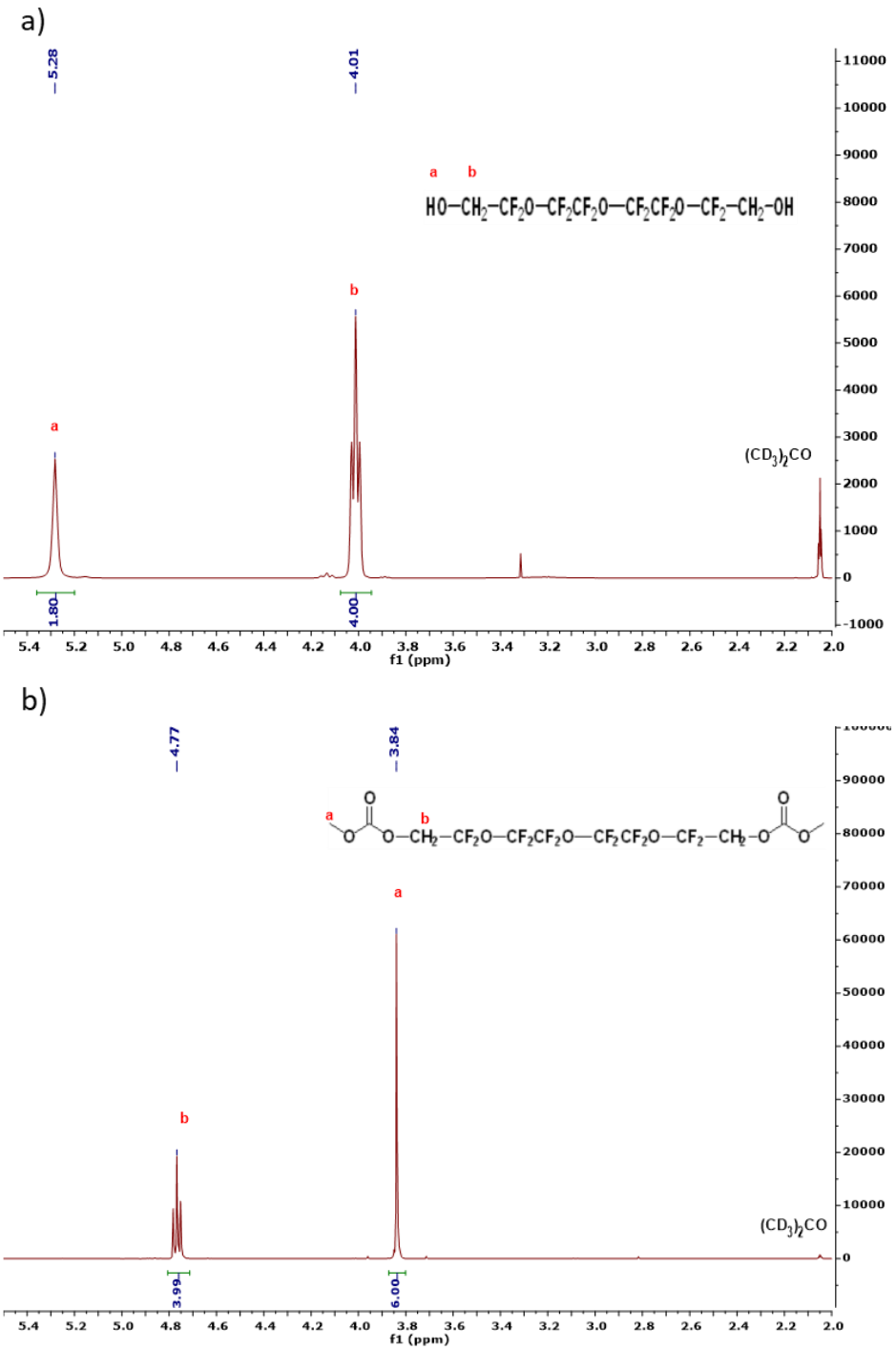

Figure 3.S1 (a) ^{1}H NMR of the precursor, C8-Diol and (b) ^{1}H NMR of the product, C8-DMC in deuterated acetone.

3.5.2 ^{19}F NMR Spectra

Fig. 3.S2 shows ^{19}F NMR spectra of C8-DMC with and without LiFSI. Fig. 3.S2a is that of neat C8-DMC and Fig. 3.S2b is of an electrolyte of composition m = 0.60 mol/kg. The fluorine peak

from LiFSI appears at a shift of 51.7 ppm. This peak shift was used during ^{19}F PFG-NMR in order to determine the FSI tracer-diffusion coefficient.

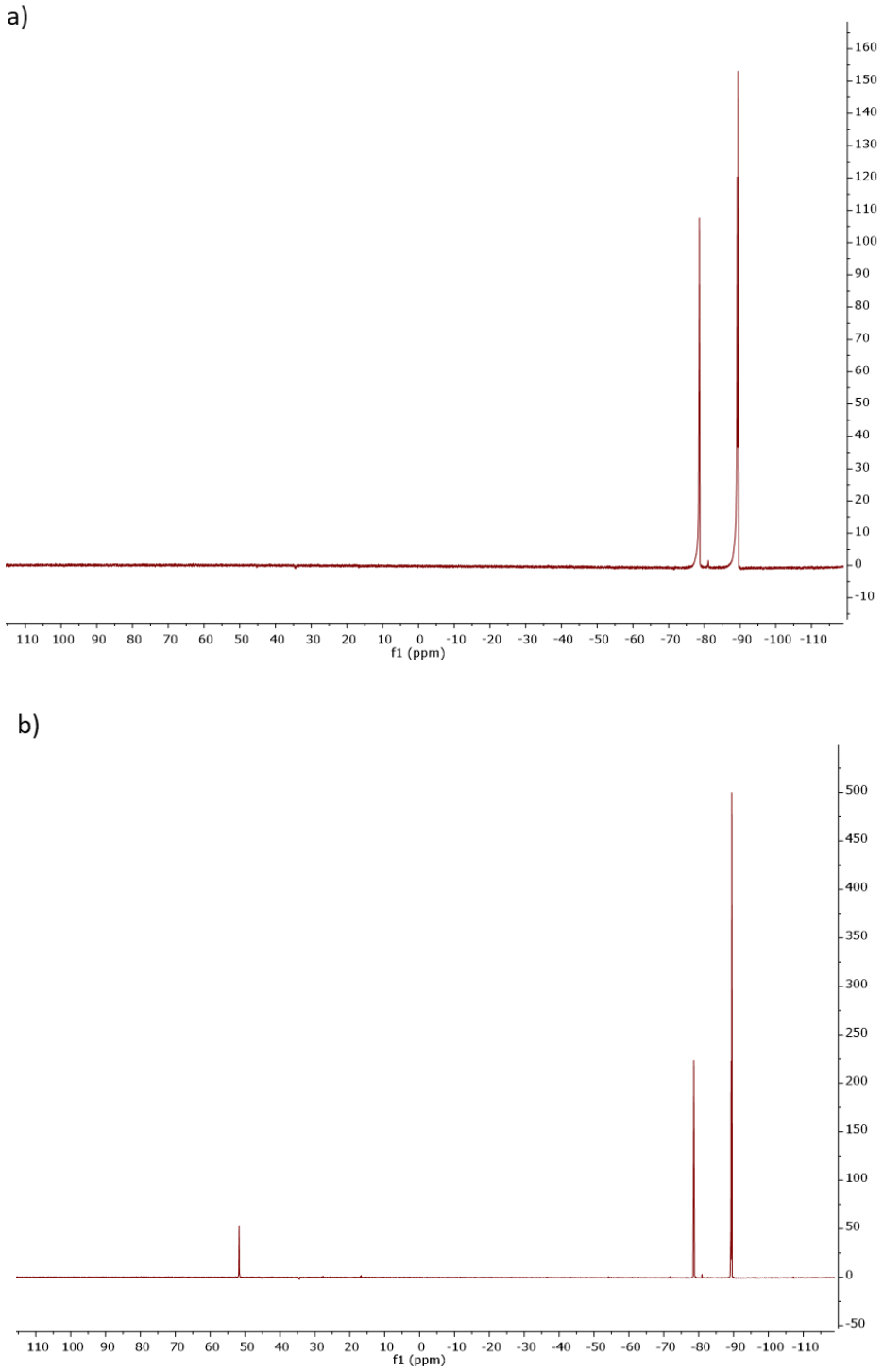

Figure 3.S2 ^{19}F NMR spectra of C8-DMC (a) neat C8-DMC (no salt) and (b) a C8-DMC based electrolyte with m = 0.60 mol/kg.

3.5.3 PFG-NMR Data

Fig. 3.S3 displays the natural log of the PFG-NMR attenuation signal vs the constants within the exponential of Eq. 3.11 in the main manuscript. The red circles are the experimental data and the black line is a linear fit to the data. The magnitude of the slope of the line-of-best-fit is the self-diffusion coefficient of D_{Li}, which is 3.23x10^{-7} cm^2/s in this case.

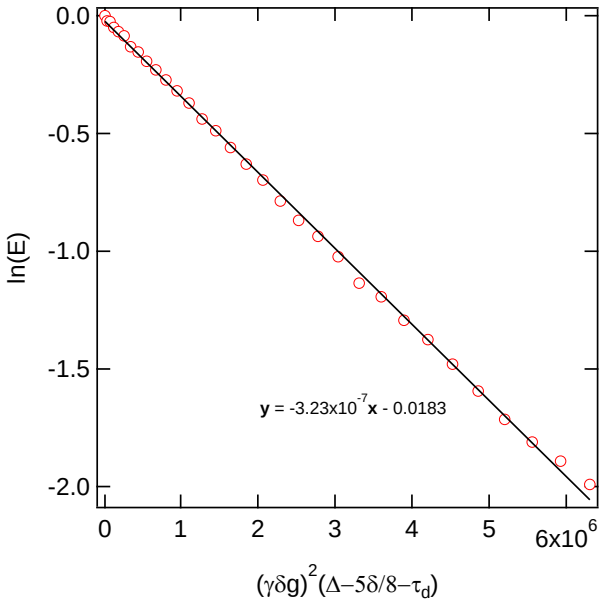

Figure 3.S3 ^{7}Li PFG-NMR diffusion data for a C8-DMC electrolyte with m = 0.05. The red circles are experimental data and the black line is the line of best fit. The slope is the self-diffusion of lithium.

3.5.4 Error Propagation

Rigorously defined transference number, t_+^0:

$$\delta t_+^0 = |t_+^0| \sqrt{\left(\frac{\delta\kappa}{\kappa}\right)^2 + \left(\frac{\delta D_s}{D_s}\right)^2 + \left(\frac{\delta t_{+,id}}{t_{+,id}}\right)^2 + \left(\frac{\delta \phi_c}{\phi_c}\right)^2} \tag{3.S1}$$

Thermodynamic factor, $1 + \frac{dln\gamma_\pm}{dlnm}$:

$$\delta\left(1 + \frac{dln\gamma_\pm}{dlnm}\right) = \left|1 + \frac{dln\gamma_\pm}{dlnm}\right| \sqrt{\left(\frac{\delta\kappa}{\kappa}\right)^2 + \left(\frac{\delta D_s}{D_s}\right)^2 + \left(\frac{\delta t_{+,id}}{t_{+,id}}\right)^2 + \left(\frac{\delta \phi_c}{\phi_c}\right)^2} \tag{3.S2}$$

Overall tracer-diffusion coefficient, D_{NMR}:

$$\delta D_{NMR} = \sqrt{\left(\frac{2D_{FSI}}{(D_{Li}+D_{FSI})^2}\delta D_{Li}\right)^2 + \left(\frac{2D_{Li}}{(D_{Li}+D_{FSI})^2}\delta D_{FSI}\right)^2} \quad (3.S3)$$

3.6 Acknowledgements

This work was intellectually led by the Joint Center for Energy Storage Research (JCESR), an Energy Innovation Hub funded by the U.S. Department of Energy (DOE), Office of Science, Basic Energy sciences (BES), under Contract No. DEAC02-06CH11357, which supported both synthesis and characterization work conducted by D. B. S., H. Q. N., and L. S. G., under the supervision of N. P. B. Early work by D. B. S. was supported by the National Science Foundation, grant number 1505669, under the SusChEM initiative. The electrolyte synthesis work was initially established by K. R. O., S. J. M., and J. D. S. who were supported by the Center for Mesoscale Transport Properties, an Energy Frontier Research Center supported by the U.S. Department of Energy, Office of Science, Basic Energy Sciences, under award #DE-SC0012673.

3.7 Nomenclature

A	Active surface area of electrode (cm2)
a, b	Fit parameters in Eq. 3.5
c	Concentration (mol/L)
D	Salt diffusion coefficient of electrolytic phase (cm^2/s)
D_i	Self-diffusion coefficient of species i as measured by PFG-NMR (cm^2/s)
D_{FSI}	Self-diffusion coefficient of FSI as measured by PFG-NMR (cm^2/s)
D_{Li}	Self-diffusion coefficient of Li as measured by PFG-NMR (cm^2/s)
D_{NMR}	Overall self-diffusion coefficient (cm^2/s)
D_s	Salt diffusion coefficient of electrolyte in separator (cm^2/s)
E	Attenuation of the echo
F	Faraday's constant (96,485 C/mol)
G	Gradient strength
I_{ss}	Steady-state current (mA)
I_{o}	Initial current (mA)
k_0	Offset voltage (mV)
L_{c}	Inductance of measurement cabling (H)
l	Thickness of electrolyte/separator (cm)
m	Molality (mol/kg)
N_{m}	MacMullin number; obtained by taking the ratio of κ/κ_s
Q_{el}	Constant phase element of the electrolyte
Q_{int}	Constant phase element of the interface
R	Ideal gas constant (J/mol K)
R_{c}	Resistance of measurement cabling (Ω)

R_{int}	Resistance of electrolyte/electrode interface (Ω)
$R_{i,0}$	Resistance of electrolyte/electrode interface initially, prior to polarization (Ω)
$R_{i,ss}$	Resistance of solvent/electrode interface when Iss reached (Ω)
R_s	Resistance of electrolyte/separator composite (Ω)
R_T	Total resistance of cell (R_s + $R_{i,0}$)
T	Temperature (K)
T_f	Thermodynamic factor
t	Time (s)
t_+^0	Transference number obtained using the Balsara and Newman method
$t_{+,id}$	Ideal transference number using steady-state current method
$t_{+,NMR}$	Transference number obtained using pulsed field gradient NMR
U	Open-circuit voltage (mV)
z^+	Cation charge
$1+\frac{dln\gamma_\pm}{dlnm}$	Thermodynamic factor

Greek

α	Nondimensional time
γ	Gyromagnetic ratio
$\gamma_\pm$	Mean molal activity coefficient of the salt
Δ	Diffusion interval (s)
ΔV	Dc polarization potential (mV)
δ	Length of gradient pulse (s)
κ	Conductivity of the electrolytic phase; (S/cm)
κ_s	Conductivity of the electrolyte and separator combined; (S/cm)
v	Stoichiometric parameter = 2 for univalent salts ($= v^+ + v^-$)
v^i	Number of cations/anions per molecule of salt ($i = +$ or $-$)
ρ	Density of electrolyte (g/L)
τ	Tortuosity of the separator
τ_d	Delay for gradient recovery (s)
ϕ_c	Volume faction of conducting phase in separator

4 Comparing Measurements of Limiting Current of Electrolytes with Theoretical Predictions up to the Solubility Limit[†]

4.1 Introduction

A barrier to the development of next-generation rechargeable lithium-based batteries is the electrolyte. Conventional electrolytes, comprising a lithium salt, $LiPF_6$, dissolved in a mixture of cyclic carbonates, exhibit limited electrochemical stability windows (< 4.5 V vs Li^+/Li), and are susceptible to thermal runaway.[103,104] One approach has been to replace conventional, carbonate electrolytes with fluorinated, electrolytes that have reduced flammability.[31,46,75,76,105] Fluorinated electrolytes also exhibit high oxidation potentials (> 5 V vs. Li^+/Li), and thus have the potential to enable high voltage cathodes.[45,106]

The operation of a battery results in the development of salt concentration gradients within the electrolyte. These gradients arise due to existence of two mobile charge carriers: the anion and cation, and the magnitudes of the gradients increase with increasing current density. The limiting current is defined as the largest current that can be imposed on the electrolyte. Conventional wisdom suggests that at the limiting current, the salt concentration gradient is so large that the salt concentration at the cathode approaches zero.[39] A few studies report experimentally determined liming current, but the factors that govern this parameter have not been fully elucidated.[107,108]

Complete electrochemical characterization for a binary electrolyte requires the measurement of the thermodynamic factor, T_f, and three transport properties: conductivity, κ, the salt diffusion coefficient, D, the cation transference number with respect to the solvent t_+^0.[39] All of the parameters must be measured as a function of salt concentration to obtain a complete picture.[80,94,95,109,110] In a recent study, Pesko et al. used measured values of T_f, κ, D, and t_+^0 in mixture of poly(ethylene oxide) (PEO) and lithium bis(trifluoromethanesulfonyl)imide salt (LiTFSI) to predict limiting current based on the conventional definition of limiting current.[111]

Recently, we reported T_f, κ, D, and t_+^0 for a perfluoropolyether, C8-DMC, mixed with lithium bis(fluorosulfonyl)imide salt (LiFSI).[112] We use Newman's concentrated solution theory to predict concentration and potential profiles as a function of salt concentration and current density in lithium symmetric cells at steady-state. We also use the theory to calculate transient concentration and potential profiles in the electrolyte. We note conditions (salt concentration and current density) under which the salt concentration at the cathode approaches zero. We also note the conditions under which salt concentration at the anode approaches the solubility limit. These predictions are compared with experimental data without the use of any adjustable parameters.

[†] This work is reported in Shah, D. B., *et al.* Comparing Measurements of Limiting Current of Electrolytes with Theoretical Predictions up to the Solubility Limit. *J. Phys. Chem. C.* **2019**, *123*, 23872 – 23881.

4.2 Experimental Details

4.2.1 Electrolyte Preparation

The perfluoroether, C8-DMC (CAS-No. 1976035-41-2), was synthesized from a diol terminated precursor following procedures described in previous work.[31,49,76,112] The chemical formula of C8-DMC is given in Fig. 1a. All sample preparation was done within an argon filled Vac glovebox with H_2O and O_2 concentrations kept below 1 ppm. Lithium bis(fluorosulfonyl)imide (LiFSI) (cat. no. 097602) was purchased from Oakwood Products, Inc. Fig. 1b contains the chemical formula of the FSI anion. The salt was ≥ 99% pure, as confirmed by a Certificate of Analysis form. The salt was dried at 100 °C under dynamic vacuum for three days inside a glovebox antechamber. Prior to transfer into the glovebox, C8-DMC was dried under active vacuum inside the glovebox antechamber at 50 °C for 72 hours. In order to form electrolytes, a predetermined amount of Li salt was added to a known mass of C8-DMC. Once the salt was added, the electrolytes were placed on a magnetic stirrer and were allowed to mix for 12 hours or more using a magnetic stir bar. The salt concentration of prepared electrolytes is described as m_{av}, the molality of the electrolyte in units of mol LiFSI/kg C8-DMC. Electrolytes were prepared within a concentration window of $0.28 \leq m_{av} \leq 1.78$ mol/kg.

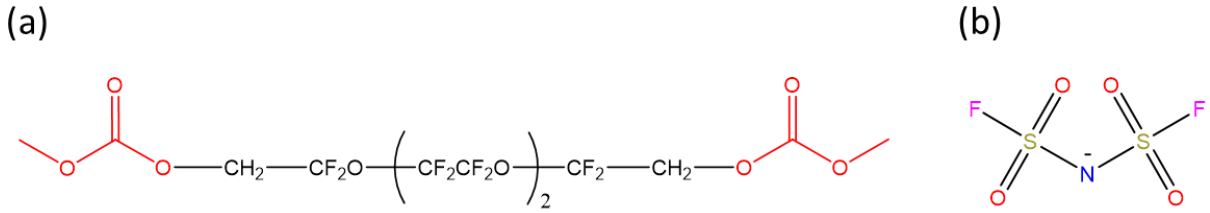

Figure 4.1 (a) C8-DMC and (b) FSI anion.

4.2.2 Lithium symmetric cells and limiting current measurements

Lithium symmetric cells were assembled by sandwiching an electrolyte-soaked separator, Celgard 2500 (Celgard Company), with lithium discs, cut from lithium chips (MTI Corp.). Celgard 2500 was cut to 19 mm in diameter and had an average thickness, L, of 25.4 ± 0.6 μm. The diameter of the 150 µm thick Li disc was 12.7 mm. Three replicate cells were produced for each electrolyte and the reported data is the average of those three cells, with error bars representing the standard deviation between the replicate cells. Data were collected on a Bio-Logic VMP3 potentiostat. Each sample cell was subjected to a conditioning treatment, which consisted of charge and discharge cycles at 0.02 mA/cm^2 in order to help stabilize the interfacial layer. The sequence performed was a 4 hour charge, 30 minutes rest, a 4 hour discharge, 30 minutes rest, and repeated for a total of 6 times. To track the cell impedance with time, ac impedance spectroscopy was performed before the beginning of conditioning, after each rest step, and at the end of conditioning. Complex impedance plots were obtained within a frequency range of 1 MHz to 100 mHz. Each sample was then polarized at all of the following current densities for 30 minutes: i_{ss} = 0.20, 0.40, 0.50, 0.60, 0.70, 0.75, 0.80, and 1.00 mA/cm^2 with potential and current data recorded every five seconds. Ac impedance spectroscopy followed each polarization and the data were analyzed in the form of a Nyquist plot. The data were fit to an equivalent electrical circuit and the interfacial impedance, R_i, was extracted, as described in a

previous publication.[76] The interfacial impedance was used to correct for the potential drop, Φ, across an electrolyte, as described in Eq. 4.1 below

$$\Phi(t) = \Phi_{measured}(t) - R_i i_{ss} A \tag{4.1}$$

where $\Phi_{measured}$ is the potential across the lithium symmetric cell as measured by the potentiostat under a given steady-state current density, i_{ss}, and A is the active area of the electrode. All electrochemical characterization was done at 30 °C.

4.3 Theory

4.3.1 Steady-state model

The relationship between i_{ss} and the electrochemical properties of an electrolyte, based on Newman's concentrated solution theory,[39] was derived in ref. [111]. This relationship changes slightly when the electrolyte is contained in a porous separator (we call this the electrolyte/separator composite), and is given by Eq. 4.2

$$\int_{m(x=0)}^{m(x)} \frac{c(m)D_s(m)}{mt_-^0(m)}\,dm = \frac{i_{ss}L}{Fz_-\nu_-}\left(\frac{x}{L}\right) \tag{4.2}$$

where c is the concentration of the salt in the electrolytic phase in mol/cm^3, D_s is the salt diffusion coefficient measured by restricted diffusion on the electrolyte/separator composite, m is the molality, t_-^0 is the anion transference number relative to the velocity of the solvent ($t_-^0 = 1 - t_+^0$), z_- is the charge number on the anion, ν_- is the number of anions the salt disassociates into, L is the thickness of the electrolyte/separator composite, x/L is the normalized thickness, and F is Faraday's constant (the transference number is unaffected by the presence of the separator). All of the ion transport properties depend on salt concentration, as indicated in Eq. 4.2. During an experiment, the average salt concentration of the electrolyte, m_{av}, is controlled. The molality profile predicted by Eq. 4.2 must be averaged from $x = 0$ to $x = L$ to ensure that the model predicted average concentration is equal to m_{av}.

The relationship between the electric potential within an electrolyte/separator composite to the measurable transport properties is given by

$$\Phi_{ss}(x) = -Fz_-\nu_- \int_{m(x=L)}^{m(x=0)} \frac{c(m)D_s(m)}{mt_{+,id}(m)\kappa_s(m)t_-^0(m)}\,dm \tag{4.3}$$

where $t_{+,id}$ is the ideal transference number (unaffected by the presence of the separator) and κ_s is the conductivity of the electrolyte/separator composite. The ideal transference number, $t_{+,id}$, is determined by the steady-state current method.[53,54] The relationship between the ideal transference number and κ, t_-^0, $1 + \frac{d\ln\gamma_\pm}{d\ln m}$ (the thermodynamic factor), and D is given in ref. [70]

and a relationship was first noted in ref. [67]. In this paper, Eqs 4.2 and 4.3 were solved numerically using MATLAB and published data[112] for the relevant parameters.

4.3.2 Transient Model

As is the case for the steady-state model, the transient model is also based on Newman's concentrated solution theory.[39] We solve the governing differential equation along the thickness direction (denoted as the x-direction in the present analysis) of the polymer electrolyte. Since lithium metal exists on both ends of the electrolyte domain, these lithium/polymer interfaces have been considered as the two boundaries of the one-dimensional computational domain. Table 1 summarizes the governing equations and boundary conditions used in this study. The mass balance relation for electrolyte salt is expressed in Eq. 4.4, which was derived based on concentrated solution theory, is used to obtain transient concentration profiles $(c(x,t))$ across the polymer electrolyte. Note that the effect of transference number gradient is also taken into account, as shown in the second term on the right of Eq. 4.4. The modified Ohm's law expressed in Eq. 4.7, which includes the polarization in the electrolyte due to concentration gradients, is used to obtain transient ionic potential profiles, $\Phi_1(x,t)$, across the polymer. The potential drop across the polymer electrolyte is denoted as $\Phi_{1,(x=0)} - \Phi_{1,(x=L)}$. The model parameters used in this study are listed in Table 4.2.

Table 4.1 Summary of governing equations for C8-DMC/LiFSI with a Celgard 2500 separator in a Li symmetric cell.

	Governing equation	Boundary conditions
Mass balance (electrolyte)	$\frac{\partial c}{\partial t} = \nabla \cdot \left[D_S \left(1 - \frac{d\ln c}{d\ln c_0}\right) \nabla c\right] - \frac{i_{ss} \cdot \nabla t_+^0}{F}$ (4.4)	$-D_s \frac{\partial c}{\partial x}\Big\|_{x=0} = \frac{1-t_+^0}{F} i_{ss}$ (4.5) $-D_s \frac{\partial c}{\partial x}\Big\|_{x=L} = -\frac{1-t_+^0}{F} i_{ss}$ (4.6)
Modified Ohm's law (Ionic phase)	$i_{ss} = -\kappa_S \nabla \Phi_2 + \frac{2\kappa_S RT}{F}\left(1 + \frac{\partial \ln f_\pm}{\partial \ln c}\right)(1 - t_+^0)\nabla \ln c$ (4.7)	$\Phi_{2,L} = 0$ (4.8)

Table 4.2 Parameters used for Li symmetric transient modeling of C8-DMC/LiFSI with a Celgard 2500 separator.

Symbol	Parameter	Initial Value	Reference
L	Thickness of separator	2.54e-3 [cm]	Measured
κ	Ionic conductivity of C8-DMC	Function of concentration	Measured
D	Diffusion coefficient of LiFSI in C8-DMC	Function of concentration	Measured
t_+^0	Cation transference number	Function of concentration	Measured
F	Faraday constant	96450 [C/mol]	-
R	Universal gas constant	8.314 [J/mol/K]	-
T	Temperature	30 [°C]	-

4.4 Results and Discussion

Our objective is to compare potential versus time curves determined experimentally in Li symmetric cells as a function of average salt concentration and current density up to the salt solubility limit and the limiting current with theoretical predictions. Table 4.3 shows the aforementioned transport and thermodynamic properties of electrolyte/separator composites for a range of salt concentrations taken from ref. [112]. It is convenient to work with units of molality for steady-state calculations while transient calculations are best done using molar concentrations. In Table 3, we list both *m* and *c*, based on measurements reported in ref. [112]. Note that t_+^0 is negative over the entire concentration range, indicating the formation of charged clusters. The interactions that lead to the formation of these clusters has not yet been elucidated.

Table 4.3 Transport properties of C8-DMC/LiFSI with a Celgard 2500 separator at 30 °C.[112]

m (mol/kg)	c (mol/cm^3)	κ_s (S/cm)	D_s (cm^2/s)	$t_{+,id}$	t_+^0	$1+\frac{d\ln\gamma_\pm}{d\ln m}$
0.28	3.87 x 10^{-4}	[2.91 ± 0.19] x 10^{-6}	[3.66 ± 0.39] x 10^{-8}	0.89 ± 0.01	-1.002 ± 0.06	0.15 ± 0.02
0.60	8.89 x 10^{-4}	[9.82 ± 0.90] x 10^{-6}	[2.24 ± 0.12] x 10^{-8}	0.77 ± 0.01	-0.751 ± 0.04	0.19 ± 0.02
0.94	1.36 x 10^{-3}	[1.17 ± 0.07] x 10^{-5}	[1.72 ± 0.13] x 10^{-8}	0.71 ± 0.07	-0.378 ± 0.04	0.42 ± 0.06
1.30	1.70 x 10^{-3}	[1.14 ± 0.09] x 10^{-5}	[1.34 ± 0.11] x 10^{-8}	0.67 ± 0.02	-0.070 ± 0.00	0.85 ± 0.11
1.78	2.36 x 10^{-3}	[7.92 ± 0.75] x 10^{-6}	[1.20 ± 0.21] x 10^{-8}	0.67 ± 0.02	-0.232 ± 0.01	1.12 ± 0.23

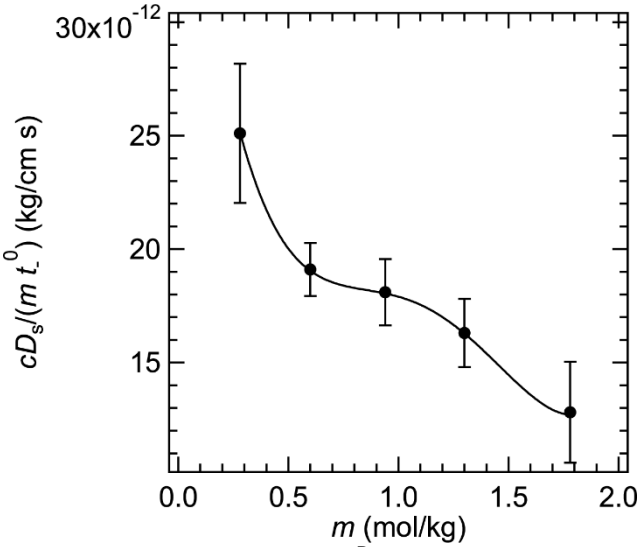

Figure 4.2: Fit of the integrand term of Eq. 2, $\frac{cD_s}{mt_-^0}$, with LiFSI salt molality. The solid curve shows the least-squares polynomial fit given by Eq. 4.9.

To calculate the concentration profile within an electrolyte given a steady-state current density, i_{ss}, and thickness, *L*, the transport parameters given in Table 4.3 were fit as a continuous function to salt concentration. In Fig. 4.2, we show the 4th order polynomial fit to the product appearing on the right side of Eq. 4.2,

$$\frac{c(m)D_s(m)}{mt_-^0(m)} = k_0 + k_1 m + k_2 m^2 + k_3 m^3 + k_4 m^4 \qquad (4.9)$$

with fitting parameters

$$k_0 = 4.358\text{x}10^{-11} \quad k_1 = -9.717\text{x}10^{-11} \quad k_2 = 1.387\text{x}10^{-10}$$
$$k_3 = -8.565\text{x}10^{-11} \quad k_4 = 1.850\text{x}10^{-11}$$

where t_-^0 is equal to $1 - t_+^0$, D_s is in cm^2/s, c is in mol/cm^3, and m is in mol/kg. The parameters apply to the range $0.28 \leq m \leq 1.78$ mol/kg and for T = 30 °C.

The concentration profile within a lithium symmetric cell under a steady-state operation is governed by the thickness of the electrolyte, L, the salt concentration, m_{av}, and the steady-state current density, i_{ss}.

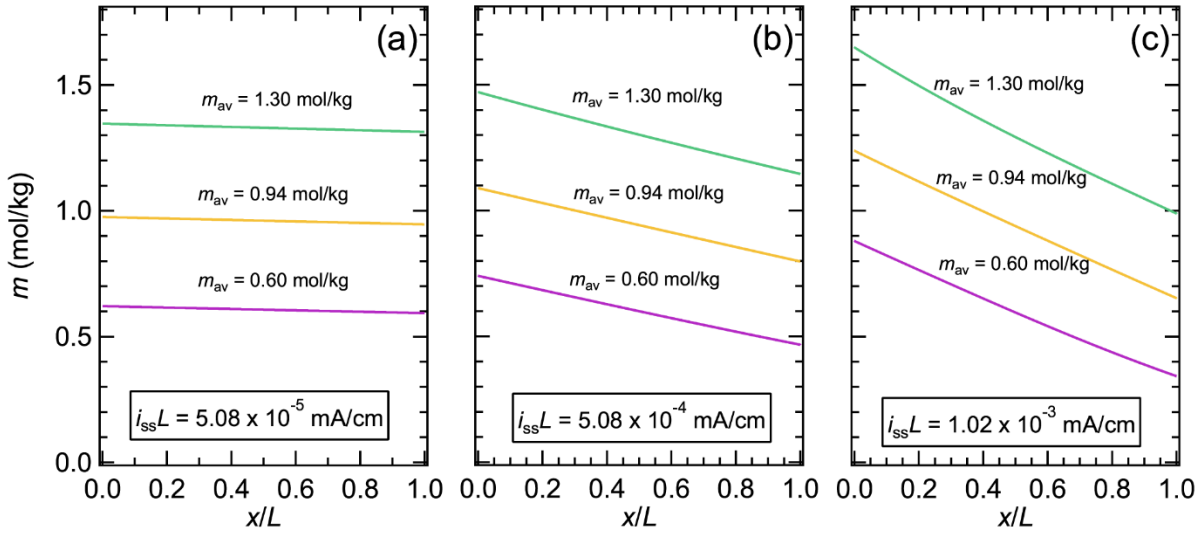

Figure 4.3 Concentration profiles of LiFSI in C8-DMC predicted by Eq. 4.2 at steady-state for three different normalized current densities: (a) $i_{ss}L$ = 5.08 x 10^{-5}, (b) $i_{ss}L$ = 5.08 x 10^{-4}, and (c) $i_{ss}L$ = 1.02 x 10^{-3} mA/cm.

Fig. 4.3 shows the concentration profiles across a mixture of C8-DMC/LiFSI for three initial concentrations of m_{av} = 0.60, 0.94, and 1.30 mol/kg and for three values of normalized current density, $i_{ss}L$. We have chosen the product $i_{ss}L$ for this plot because i_{ss} is inversely proportional to L; Fig. 4.3 may thus be used to determine i_{ss} values for L values different from that used in this particular study. The concentration profiles were obtained by numerically solving Eq. 4.2 using the fitted Eq. 4.4. The figures correspond to $i_{ss}L$ = 5.08 x 10^{-5}, 5.08 x 10^{-4}, and 1.02 x 10^{-3} mA/cm (relating to i_{ss} = 0.02, 0.20, and 0.40 mA/cm^2 for L = 0.00254 cm). It is evident from Fig. 4.3a that under small applied normalized current densities ($i_{ss}L$ = 5.08 x 10^{-5} mA/cm), the concentration profiles are approximately linear and the gradients are small. However, with increasing normalized current densities, the concentration gradients become steeper, as shown in Figs. 3b and c. Note that the overall flux of lithium cations, at steady-state, is toward the negative electrode in spite of the fact that the transference number is negative at all salt concentrations.

The sign of the transference number only gives the direction of the flux of lithium cations in a solution of uniform composition in response to an applied electrochemical potential. Thus, at the instant that a dc potential is applied to the cell, the net lithium cation flux is toward the positive electrode. At steady-state after the salt concentration gradients are fully developed, the net lithium cation flux is toward the negative electrode.[13]

One can estimate the normalized limiting current, $i_{\text{limit}}L$, within an electrolyte using model predicted concentration profiles. In order to do so, an electrolyte of known m_{av} must be modeled under a number of $i_{\text{ss}}L$ values and the salt concentration at the cathode (x/L = 1) is extracted at each normalized current density. An example of such an analysis is shown in Fig. 4.4a. In Fig. 4.4a, $i_{\text{ss}}L$ is plotted against the model predicted salt concentration, m, at x/L = 1 in blue circles for an electrolyte with an average salt concentration of m_{av} = 0.94 mol/kg. As the model is limited between $0.28 \leq m \leq 1.78$ mol/kg, the conventional limiting current must be predicted by extrapolating m(at x/L = 1) to zero. The dashed, black curve is a 2nd order polynomial fit to the model predicted values in Fig. 4.4a, and predicts $i_{\text{limit}}L$ = 3.7 x 10^{-3} mA/cm. It should be noted that the solubility limit of LiFSI in C8-DMC is 2.03 mol/kg.[76] It is obvious that the concentration at any x/L in the cell must not exceed this value for stable operation. The highest salt concentration occurs at the anode (x/L = 0). In Fig. 4.4b, we thus plot $i_{\text{ss}}L$ versus m(x/L = 0) for the same average salt concentration used in Fig. 4.4a (m_{av} = 0.94 mol/kg). A 2nd order polynomial is fit through the data and extrapolated to m = 2.03 mol/kg is shown as a dashed curve. We define the normalized limiting current at which this occurs as $i_{\text{limit,sat}}L$ which is 3.2 x 10^{-3} mA/cm for m_{av} = 0.94 mol/kg.

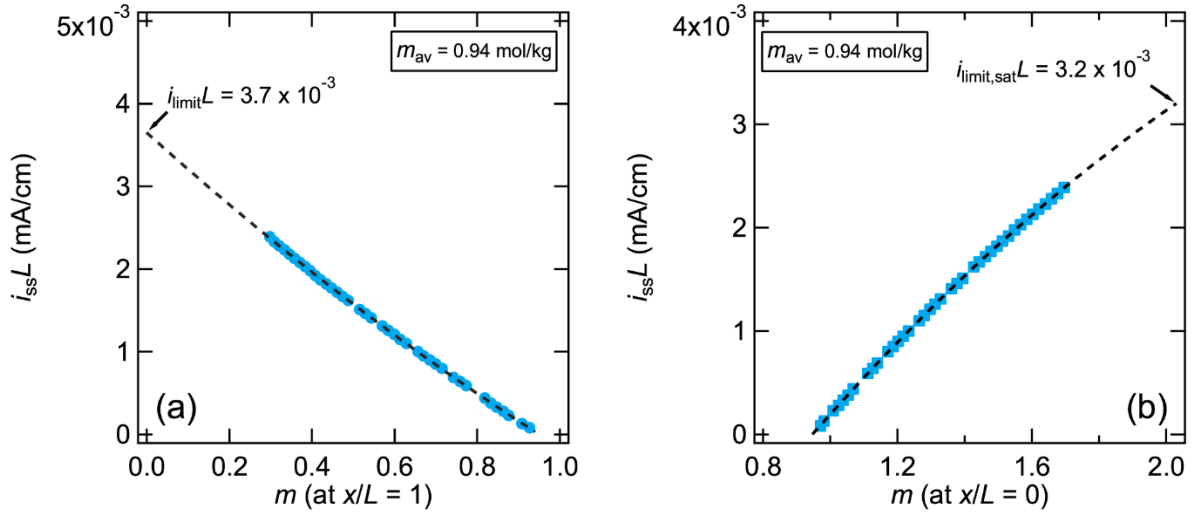

Figure 4.4 Concentration predictions at the anode (x/L = 0) and cathode (x/L = 1) for varying $i_{ss}L$ values for an electrolyte with an average concentration of m_{av} = 0.94 mol/kg. (a) Model predictions of the concentration at the cathode, x/L = 1. The black dashed curve shows the least-squares polynomial fit, which was extrapolated to m = 0 mol/kg to determine the normalized limiting current density (marked as $i_{limit}L$). (b) Model predictions of the concentration at the anode, x/L = 0. The black dashed curve is a least-squares polynomial fit, which was extrapolated to the salt solubility limit of m = 2.03 mol/kg. This determined the normalized limiting current density caused by salt saturation at the anode (marked as $i_{limit,sat}L$).

There is an important question: for a given m_{av}, which mode of the limiting current will be observed? We posit that the mode will correspond to the one that is obtained at the lower normalized limiting current. For m_{av} = 0.94 mol/kg, we conclude that the normalized limiting current will occur due to salt precipitation. Similar analysis was repeated at all values of m_{av}.

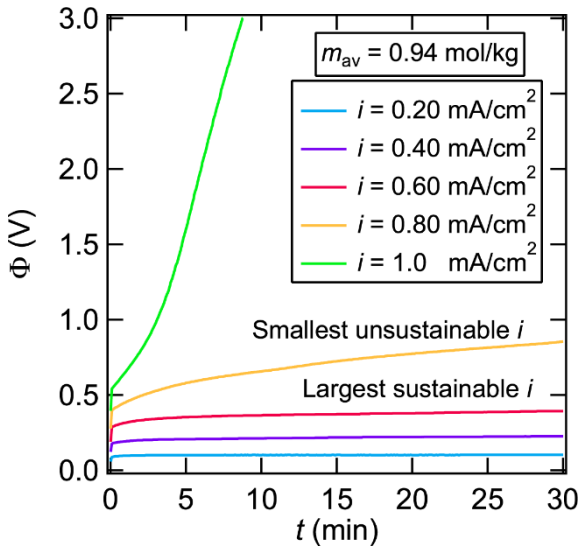

Figure 4.5 Time dependent potential behavior of C8-DMC/LiFSI with an average salt concentration of m_{av} = 0.94 mol/kg in response to applied current densities from i = 0.20 to 1.0 mA/cm^2 (no interfacial impedance correction). The largest sustainable current density, i, as determined by plateau in measured potential, was 0.60 mA/cm^2, shown as a solid red curve. The smallest unsustainable i, as determined by the lack of a plateau in the potential within the measurement window, was 0.80 mA/cm^2 and is shown as a solid yellow curve.

Turning to experiments, we now discuss potential versus time curves for an electrolyte/separator composite in a lithium symmetric cell (L = 0.00254 cm) at a fixed applied current. In Fig. 4.5, we show the potential profile versus time for current densities ranging from i_{ss} = 0.20 mA/cm^2 to 1.00 mA/cm^2 in 0.2 mA/cm^2 increments for an initial concentration of m_{av} = 0.94 mol/kg. At low current densities (below 0.60 mA/cm^2), the potential increases instantaneously at $t = 0^+$ due to the resistance of the cell when concentration is uniform, increases with time as concentration gradients develop, and reaches a plateau when the concentration profile in the cell approaches steady-state. At a slightly higher current density of 0.80 mA/cm^2, the potential increases monotonically with time and does not reach a plateau. We refer to 0.60 mA/cm^2 as the largest sustainable current density and 0.80 mA/cm^2 as the smallest unsustainable current density. Increasing the current density beyond 0.80 mA/cm^2 leads to potential increases exponentially with time with no hint of a plateau. Data similar to that shown in Fig. 4.5 was obtained for all of the electrolytes. The normalized limiting current density, $i_{limit}L$, was determined for each electrolyte by averaging the largest sustainable current and smallest unsustainable current. In Fig. 4.6, we plot the experimental limiting current, $i_{limit}L$, as a function of m_{av}. The normalized limiting current for m_{av} = 0.28 mol/kg is 1 x 10^{-3} mA/cm. It increases with increasing salt concentration, reaching a broad maximum of $i_{limit}L$ = 1.8 x 10^{-3} mA/cm between m_{av} = 0.60 and

0.94 mol/kg. Further increase in m_{av} results in a decrease in $i_{limit}L$ until m_{av} = 1.78 mol/kg, a value that is close to the salt solubility limit.

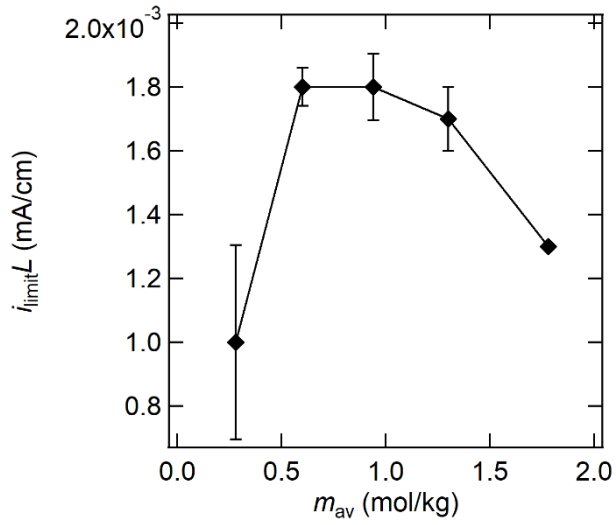

Figure 4.6 Experimental limiting current as a function of salt concentration. The limiting current was taken as the average between the largest sustainable current and smallest unsustainable current. The solid line is drawn to guide the eye.

In Fig. 4.7a, $i_{limit}L$ is plotted against m_{av}; the black diamonds show experimental measurements that were shown in Fig. 4.6, red squares represent the predicted $i_{limit}L$ when concentration reaches zero at the cathode (x/L = 1), and blue circles are the predicted $i_{limit}L$ values when the solubility limit of m = 2.03 is reached at the anode (x/L = 0). The cathode-dominated $i_{limit}L$ (the traditional limiting current) increases with increasing concentration. In contrast, the anode-dominated $i_{limit,sat}L$ decreases with increasing concentration. The two normalized limiting currents are equal to each other at m_{av} = 0.88 mol/kg. Following our assumption that the failure mode obtained experimentally corresponds to the one that requires the lower current density, we conclude that salt depletion at the cathode causes the limiting current at m_{av} < 0.88 mol/kg, while salt precipitation at the anode causes the limiting current at m_{av} > 0.88 mol/kg. The two solid curves through the theoretical predictions in Fig. 4.7a show these two branches. The theoretical predictions provide a qualitative explanation for the observed non-monotonic dependence of the measured limiting current on salt concentration. There are two important quantitative differences between theory and experiment in Fig. 4.7a: (1) The theoretical limiting currents are about a factor of 2 higher than those measured experimentally and (2) The peak in the limiting current versus salt concentration predicted by theory is sharper than that observed experimentally. We do not have definitive explanations for these deviations, except to note that the interface between the electrode and electrolyte is complex, and that failure in the experimental cells may begin before the salt concentration at the cathode reaches zero or the salt concentration at the anode reaches the solubility limit.

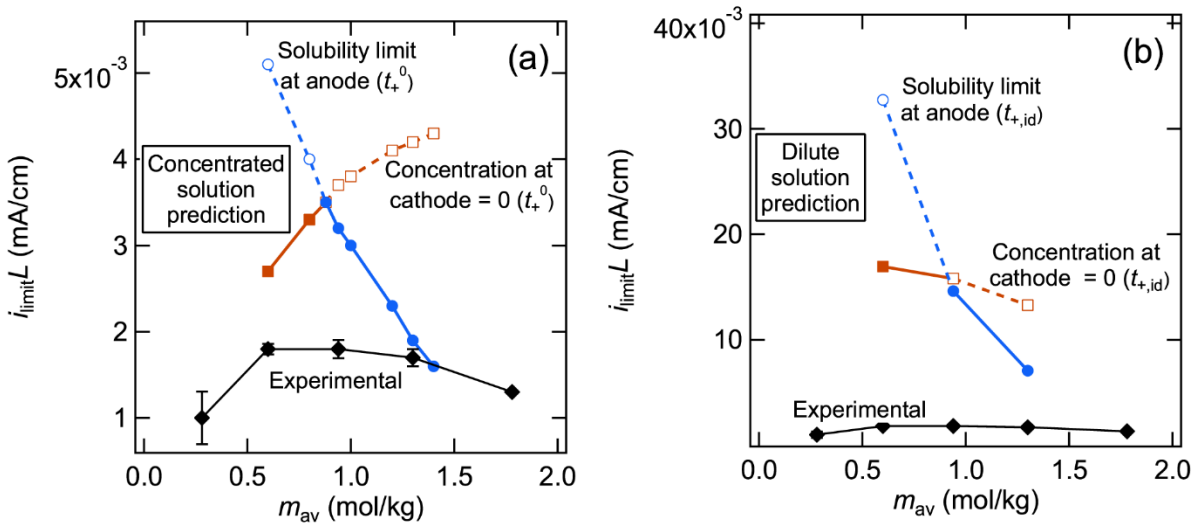

Figure 4.7 Normalized limiting current predictions as a function of m_{av} and compared to experimental values (shown in black). (a) Concentrated solution theory predictions of the normalized limiting current. The red dashed and solid curves are the $i_{limit}L$ predicted when extrapolating m_{av} to 0 mol/kg at the cathode (x/L = 1). The blue dashed and solid curves are the $i_{limit,sat}L$ predicted by extrapolating m_{av} to 2.03 mol/kg at the anode (x/L = 0). (b) Normalized limiting current predictions using dilute solution theory. The red dashed and solid curves are the $i_{limit}L$ predicted by Eq. 4.10 (concentration equal to 0 mol/cm^3 at the cathode). The blue dashed and solid curves are the $i_{limit,sat}L$ predicted by Eq. 4.11 (salt saturation at the anode, c_{sat} = 2.61 x 10^{-3} mol/cm^3). Normalized limiting current predictions using dilute solution theory are an order of magnitude higher than the experimental values.

Approximate expressions are often used to determine the normalized limiting current due to salt depletion at the cathode. [113–115] One such expression can be derived by combining equations 11.22, 11.41, 11.43, and 11.57 in ref. [39]:

$$i_{limit}L = \frac{2c_{av}D_sF}{1-t_{+,id}} \tag{4.10}$$

where c_{av} is the average electrolyte concentration in mol/cm^3, D_s is the restricted diffusion coefficient in the electrolyte/separator composite, and we have taken the liberty of using the $t_{+,id}$. Similarly, the normalized limiting current that causes the concentration at the anode to approach the solubility limit is:

$$i_{limit,sat}L = \frac{2(c_{sat}-c_{av})D_sF}{1-t_{+,id}} \tag{4.11}$$

where c_{sat} is salt solubility limit. For mixtures of C8-DMC and LiFSI, c_{sat} = 2.61 x 10^{-3} mol/cm^3. Equations 4.10 and 4.11 were derived using dilute solution theory, thus the ideal transference number, $t_{+,id}$, is used in both equations. In Fig. 4.7b, we plot $i_{limit}L$ vs. m_{av}; red squares denote the predicted $i_{limit}L$ using Eq. 4.10, and blue circles represent the predicted $i_{limit,sat}L$ using Eq. 4.11. Both predictions for the normalized limiting current decrease with increasing salt

concentration. The cross-over from the salt-depletion limit to the salt precipitation limit occurs at a reasonable value of m_{av}, but the predicted trend is monotonic with salt concentration and inconsistent with the experimental data. In addition, the theoretical predictions for normalized limiting current based on dilute solution theory are an order of magnitude higher than those measured experimentally (black squares in Fig. 4.7b). It is obvious from Fig. 4.7 that concentrated solution theory is essential for establishing the underpinnings of the normalized limiting current in our system.

We now return to the potential that can be predicted using Eq. 4.3. In Fig. 4.8, we plot the integrand in Eq. 4.3 along with a fit to the following empirically determined function:

$$\frac{c(m)D_s(m)}{mt_{+,id}(m)\kappa_s(m)t_-^0(m)} = b_0\exp(\tau_3 m) + b_1\exp(\tau_4 m) \tag{4.12}$$

with fitting parameters

$$b_0 = 1.802 \text{ x } 10^{-6} \quad b_1 = 8.566 \text{ x } 10^{-5}$$
$$\tau_3 = 0.1541 \qquad \tau_4 = -8.525$$

where κ_s is the conductivity of the separator/electrolyte composite in S/cm.

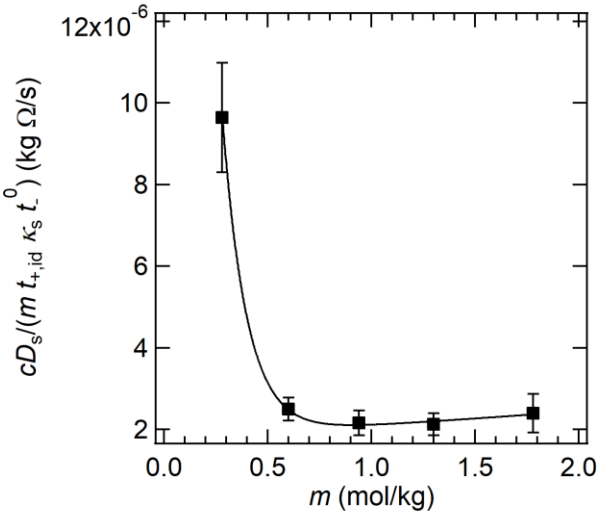

Figure 4.8: Fit of the integrand term of Eq. 4.3, $\frac{cD_s}{mt_{+,id}\kappa_s t_-^0}$, with LiFSI salt molality. The solid curve shows the least-squares fit to the double exponential given by Eq. 4.7.

The fit from Fig. 4.8 allows for potential predictions across the C8-DMC/LiFSI electrolyte. In Fig. 4.9, we show the predicted potential profile, $\Phi(x/L)$, across the electrolyte from x/L = 0 to 1 for selected values of m_{av} and $i_{ss}L$. We define Φ = 0 at x/L = 1. The purple, yellow, and green solid curves are potential profiles for m_{av} = 0.60, 0.94, and 1.30 mol/kg, respectively. From left to right, each figure provides profiles for $i_{ss}L$ = 5.08 x 10^{-5}, 5.08 x 10^{-4}, and 1.02 x 10^{-3} mA/cm, respectively. Note that these values of $i_{ss}L$ correspond to the applied i_{ss} in our cell equal to 0.02, 0.20, and 0.40 mA/cm^2 (L = 0.00254 cm). At $i_{ss}L$ = 5.08 x 10^{-5} mA/cm, the potential profile

across the electrolyte is linear and the gradient is small, as shown in Fig. 4.9a, but the potential behavior becomes less linear with increasing $i_{ss}L$. Interestingly, the intermediate concentration of m_{av} = 0.94 mol/kg shows a lower $\Phi(x)$ across the electrolyte at all values of $i_{ss}L$, compared to m_{av} = 0.60 or 1.30 mol/kg. The potential drop for m_{av} = 0.60 shows more complex behavior: it has a lower potential drop across the electrolyte when compared to m_{av} = 1.30 at both $i_{ss}L$ = 5.08 x 10^{-5} and 5.08 x 10^{-4} mA/cm, but has the largest potential drop across the electrolyte at $i_{ss}L$ = 1.02 x 10^{-3} mA/cm. Next, we compare the model predicted potential drop across the electrolyte to experimental measurements of potential, Φ_{exp}, for a range of m_{av}. The experimentally accessible potential is at x/L = 0. We thus define Φ_0 as to be the theoretically predicted potential at x/L = 0 for a given m_{av} and i_{ss}.

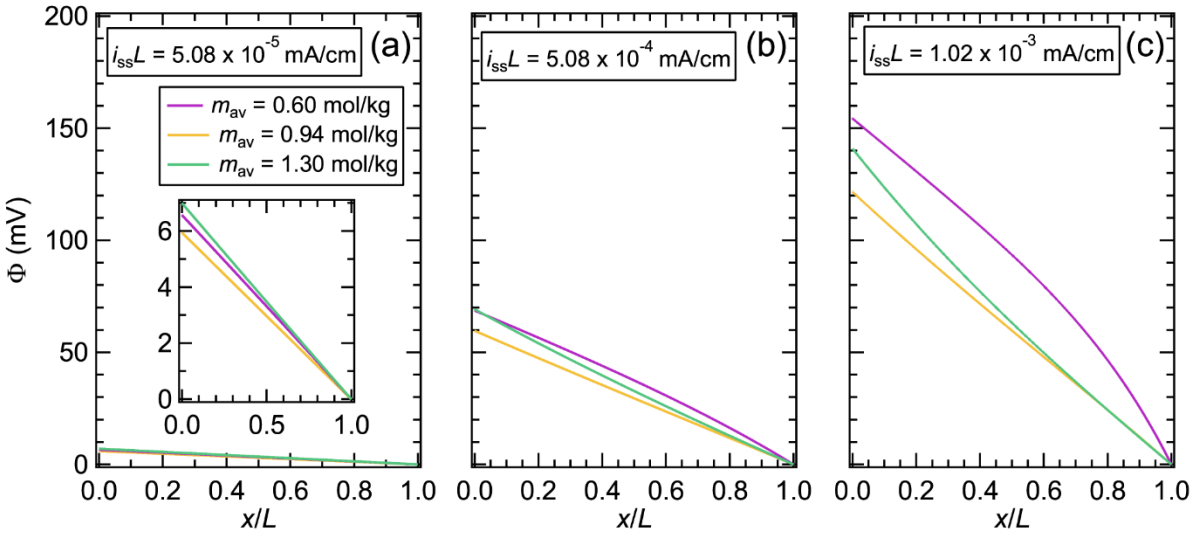

Figure 4.9 Potential profiles in C8-DMC/LiFSI electrolytes predicted by concentrated solution theory at steady-state. These are calculated using Eq. 4.3 based on the fit shown in Fig. 4.8. Potential profile for (a) $i_{ss}L$ = 5.08 x 10^{-5} mA/cm, (b) $i_{ss}L$ = 5.08 x 10^{-4} mA/cm, and (c) $i_{ss}L$ = 1.02 x 10^{-3} mA/cm. Interestingly, the potential drop across C8-DMC/LiFSI with m_{av} = 0.60 at $i_{ss}L$ = 5.08 x 10^{-5} mA/cm is less than that of m_{av} = 1.30, but has a higher potential drop at $i_{ss}L$ = 1.02 x 10^{-3} mA/cm.

The experimentally applied potential drop, Φ_{exp}/L, for the electrolyte with m_{av} = 0.94 mol/kg is plotted as a function of i_{ss} in Fig. 4.10a. The experimental potential drop is corrected for the lithium/electrolyte interfacial impedance using Eq. 4.1. Also shown in Fig. 4.10a is the predicted potential drop, Φ_0/L, calculated from Fig. 4.9 for m_{av} = 0.94 mol/kg. Both theory and experiment indicate that Φ/L increases with increasing i_{ss}. At i_{ss} = 0.20 mA/cm^2, the theoretically predicted potential drop, Φ_0/L, is within experimental error. The deviation between experiments and theory increases with increasing current density. Further work is needed to resolve this discrepancy. In Fig. 4.10b, we plot Φ_{exp}/L versus m_{av} for i_{ss} = 0.4 mA/cm^2. Φ_{exp}/L is a weak function of m_{av}. Theoretical predictions, also shown in Fig, 10b, support this observation. While the theoretical predictions generally lie below the experimental data, they are within experimental error at m_{av} = 0.60 and 1.30 mol/kg.

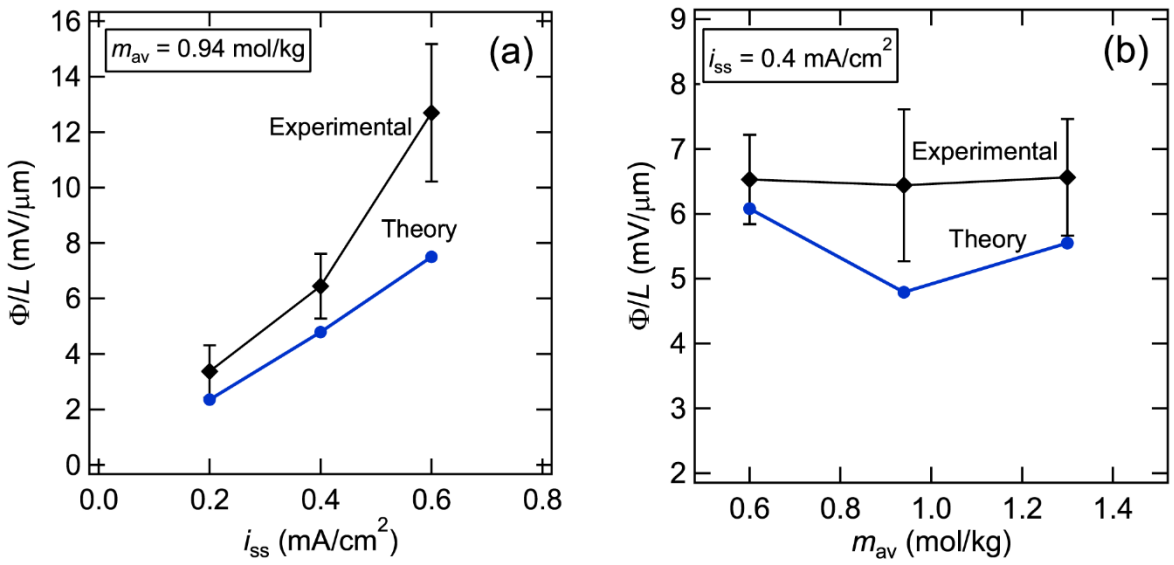

Figure 4.10 Experimental (black) and model predicted (blue) potential as a funtion of (a) i_{ss} for a concentration of m_{av} = 0.94 mol/kg and (b) m_{av} for i_{ss} = 0.40 mA/cm^2.

Fig. 4.11 shows the comparison between the experimentally measured and predicted time evolution of cell potential based on the transient model (Table 1) using the same thermodynamic and transport parameters used in the analysis of steady-state data presented in Figs. 2-10. The transient model, as described in Table 4.1, is used for the numerical predictions of cell potential for different average salt concentrations of m_{av} = 0.60 mol/kg (c_{av} = 8.89 x 10^{-4} mol/cm^3), m_{av} = 0.94 mol/kg (c_{av} = 1.36 x 10^{-3} mol/cm^3), and m_{av} = 1.30 mol/kg (c_{av} = 1.70 x 10^{-3} mol/m^3). The experimental results, denoted by the solid curves, are obtained from averaged potentials measured from three separate cells; whereas, the highlighted regions show the range of measured potentials across the cells. The dashed curves indicate the transient model results. As shown in Fig. 4.11a and b, the transient model predictions are in quantitative agreement with experiments at all applied current densities for m_{av} = 0.60 and 0.94 mol/kg. The theoretical and experimental potential jumps at $t = 0^+$ are in agreement, as is the approach to steady-state wherein the cell potential increases with time as concentration gradients develop. The agreement between theory and experiment is only qualitative at m_{av} = 1.30 mol/kg (Fig. 4.11c). While the time-scale over which concentration gradients develop are similar in both theory and experiment, both the instantaneous potential at $t = 0^+$ and the steady-state potential measured experimentally are higher than theoretical predictions. While it is not clear why this discrepancy is seen at m_{av} = 1.30, the agreement between the model and the data seen in Fig. 4.11 is noteworthy, as there are no adjustable parameters in the model.

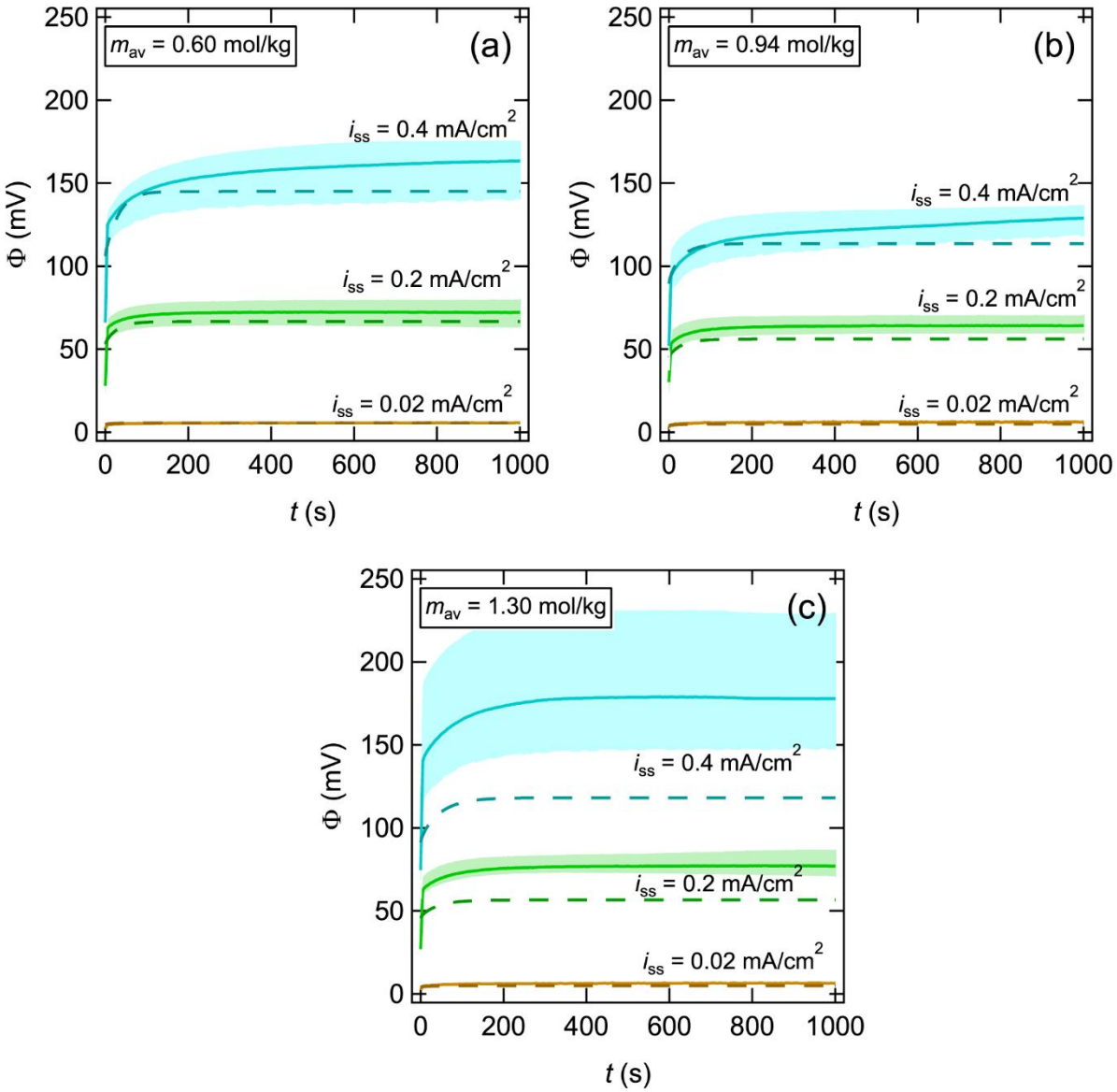

Figure 4.11 Time dependent experimental potentials (solid curves) are compared to our transient model (dashed curves) for litihium symmetric cells. The experimental data was averaged from three replicate cells (solid curves) and the error is given by the standard deviation (light shaded areas). Transient potential behavior for i_{ss} = 0.02, 0.20, and 0.40 mA/cm^2 for (a) m_{av} = 0.60 mol/kg, (b) m_{av} = 0.94 mol/kg, and (c) m_{av} = 1.30 mol/kg.

4.5 Conclusion

The performance of an electrolyte in a battery is limited, in part, by the maximum current that can be drawn through it. Traditionally, this maximum is calculated by predicting salt concentration profiles as a function of current density and noting the current density at which the salt concentration at the cathode is zero. Another limitation arises when the salt concentration at the anode exceeds the solubility limit. Our analysis considers both possibilities. We have used Newman's concentrated solution theory to predict steady-state salt concentration profiles as a

function of current density for mixtures of C8-DMC and LiFSI. These predictions were enabled by the complete electrochemical characterization of these mixtures (i.e., measurement of κ, D, t_+^0, and T_f as functions of salt concentration) that was reported in ref. [112]. An interesting feature of these electrolytes is that t_+^0 is negative across all salt concentrations. The dc potential across Li symmetric cells containing C8-DMC/LiFSI was measured experimentally as a function of applied current density and salt concentrations. At high enough current densities, clear signatures of the limiting current were observed. The experimentally determined limiting current was a non-monotonic function of salt concentration. It increases with increasing salt concentration up to m_{av} = 0.94 mol/kg and decreases with increasing salt concentration at higher values of m_{av}. The solubility limit of LiFSI in C8-DMC is 2.03 mol/kg. Our theoretical analysis indicates that the limiting current, up to m_{av} = 0.88 mol/kg, occurs due to depletion of salt at the cathode, while the limiting current at higher values of m_{av} occurs due to the salt saturation at the anode. The experimentally determined time dependence of the potential across the lithium symmetric cells was also compared to predictions based on Newman's concentrated solution theory. Our approach enables comparing theory with experiment with no adjustable parameters.

4.6 Acknowledgements

This work was intellectually led by the Joint Center for Energy Storage Research (JCESR), an Energy Innovation Hub funded by the U.S. Department of Energy (DOE), Office of Science, Basic Energy Sciences (BES), under Contract No. DEAC02-06CH11357. Early work by D.B.S. was supported by the National Science Foundation, Grant Number 1505669, under the SusChEM initiative. We thank Dr. Kevin R. Olson, Dr. Sue J. Mecham, and Prof. Joseph M. DeSimone for their helpful guidance in synthesizing C8-DMC.

4.7 Nomenclature

A	Active surface area of electrode (cm^2)
c	Concentration (mol/cm^3)
D	Salt diffusion coefficient of electrolytic phase (cm^2/s)
D_s	Salt diffusion coefficient of electrolyte in separator (cm^2/s)
F	Faraday's constant (96,485 C/mol)
i_{ss}	Steady-state current density (mA/cm^2)
i_{limit}	Limiting current density (mA/cm^2)
$i_{limit,sat}$	Limiting current density due to salt precipitation (mA/cm^2)
L	Thickness of electrolyte/separator (cm)
m	Molality (mol/kg)
R	Ideal gas constant (J/mol K)
R_i	Resistance of electrolyte/electrode interface when i_{ss} is reached (Ω)
T	Temperature (K)
T_f	Thermodynamic factor
t	Time (s)
t_+^0	Cation transference number relative to the solvent velocity. Obtained using the Balsara and Newman method

t_-^0	Anion transference number relative to the solvent velocity; $t_-^0 = 1 - t_+^0$
$t_{+,id}$	Ideal transference number using steady-state current method
x	Position (cm)
z_-	Anion charge
$1 + \frac{dln\gamma_\pm}{dlnm}$	Thermodynamic factor

Greek

$\gamma_\pm$	Mean molal activity coefficient of the salt
κ	Conductivity of the electrolytic phase; (S/cm)
κ_s	Conductivity of the electrolyte and separator combined; (S/cm)
v_i	Number of cations/anions per molecule of salt ($i = +$ or $-$)
Φ	Electrolyte potential (mV)
Φ_{exp}	Experimental electrolyte potential (mV)
$\Phi_{measured}$	Measured cell potential (mV)
Φ_0	Steady-state model predicted electrolyte potential taken at x = 0 (mV)
Φ_1	Potential of the electrolyte at the electrode boundary for the transient model (mV)

5 Complete Set of Ion Transport Properties in Low Molecular Weight Poly(Ethylene Oxide) as a Function of Temperature

5.1 Introduction

Next-generation lithium-based batteries are a necessity for enabling a carbon-free energy grid and transportation sector.[116–118] An ideal battery requires high energy densities combined with safe, and reliable operation.[40] However, traditional lithium-ion batteries utilize electrolytes that are composed of flammable, volatile carbonates. Ethylene oxide derivatives have the potential to replace carbonate electrolyte as a safe alternative.[55,68,119–121] An interesting property of ethylene oxide is that it can be polymerized to various molecular weights, which imbues interesting transport properties as a function of molecular weight. Many studies exist on ion transport properties for high and low molecular weight poly(ethylene oxide) (PEO), but often only a few ion transport properties are measured in isolation.[80,95,109,122–125] Lithium bis(trifluoromethanesulfonyl)imide (LiTFSI) is traditionally used within ethylene oxide based polymers due to its high dissociation constant and ethylene oxide's ability to solvate lithium cations.[126–128] In addition, it is important to understand the full suite of transport parameters as a function of molecular weight. The conductivity of PEO decreases with increasing molecular weight until the entanglement regime is approached.[60,121,129] However, we do not have a clear understanding of how the salt diffusion coefficient or transference number are affected by molecular weight.

Electrolytes facilitate ion transport within a battery, and for a binary electrolyte, that transport is governed by the thermodynamic factor, T_f, and three transport parameters: ionic conductivity, κ, salt diffusion coefficient, D, and the transference number, t_+^0. Once these parameters are experimentally measured as a function of salt concentration, electrolyte behavior can be predicted for a given current density. Such predictive behavior could be beneficial to electric vehicles or energy storage devices as it would inform the rate of charge or discharge a cell can undergo prior to failure. In addition, as current is drawn through a battery, significant temperature changes can occur due to joule heating.[130] These temperature changes affect ion transport properties, and thus the current draw an electrolyte can support. The maximum current that can be passed through an electrolyte is known as the limiting current, which is the point at which lithium cations are depleted on the cathode surface.

In this work, we study a low molecular weight analog of PEO – tetraethylene glycol dimethyl ether (tetraglyme), mixed with lithium bis(trifluoromethanesulfonyl)imide (LiTFSI).The chemical structure of tetraglyme is shown in Fig. 5.1a and that of LiTFSI in Fig. 1b. We report a complete set of electrochemical properties: κ, D, t_+^0, and T_f for T = 30 and 90 °C. We use the measured electrochemical properties at 90 °C to model salt concentration profiles in lithium symmetric cells as a function of salt concentration and current density. We use concentrated solution theory and dilute solution theory to predict the limiting current for a range of salt concentrations. These predictions are compared to experimental limiting current values without the use of any adjustable parameters.

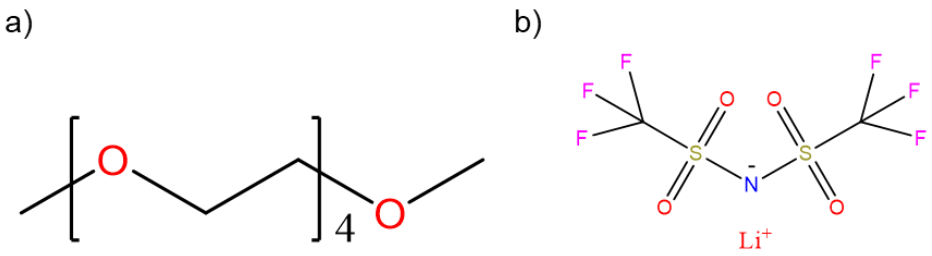

Figure 5.1 Chemical structures of a) Tetraglyme and b) LiTFSI.

5.2 Experimental and Theoretical Details

5.2.1 Electrolyte Preparation

Tetraethylene glycol dimethyl ether (tetraglyme) (cat. no. 172405) was purchased from Sigma-Aldrich. The chemical was ≥ 99% pure. Prior to transfer into the glovebox, tetraglyme was dried under active vacuum inside the glovebox antechamber at 50 °C for 72 hours. Lithium bis(trifluoromethanesulfonyl)imide (LiTFSI) (cat. no. 544094) was purchased from Sigma-Aldrich and was reported to be ≥ 99.95% pure. LiTFSI was dried at 120 °C under dynamic vacuum for three days inside a glovebox antechamber.

In order to form electrolytes, a predetermined amount of LiTFSI was added to a known mass of tetraglyme. Once the salt was added, the electrolytes were placed on a magnetic stirrer and were allowed to mix for 12 hours or more using a magnetic stir bar at room temperature. Salt concentration for electrolytes ranged from m_{av} = 0.18 to 5.37 mol salt per kg solvent (mol/kg). Values of salt wt %, molality, m_{av}, and concentration, c_{av}, for electrolytes prepared for measurements performed at 90 °C and 30 °C are shown in Table 5.1, where m_{av} and c_{av} are the average electrolyte molality and concentrations, respectively.

The density, ρ, for select salt concentrations was obtained by filling a differential scanning calorimetry (DSC) sample pan (TA Instruments) with a known volume of 40 uL and measuring the mass of the electrolyte at 90 °C. The density was interpolated for unmeasured electrolytes using a curve of best fit, shown in Fig. 5.2. The densities of electrolytes measured at 90 °C were also used for 30 °C.

Table 5.1 Values of LiTFSI wt%, molality, and calculated concentration for electrolytes studied at 90 °C. Italicized electrolytes were also studied at 30 °C.

LiTFSI wt%	m_{av} (mol/kg)	c_{av} (mol/L)
4.89	*0.18*	*0.17*
9.41	0.36	0.35
17.2	0.72	0.69
23.7	1.08	0.99
29.4	*1.45*	*1.27*
34.0	1.79	1.52
38.3	2.16	1.76
42.0	2.52	1.96
45.3	*2.88*	*2.16*
48.1	3.23	2.33
52.1	3.78	2.58
55.3	4.30	2.78
58.2	4.86	2.98
60.7	*5.37*	*3.14*

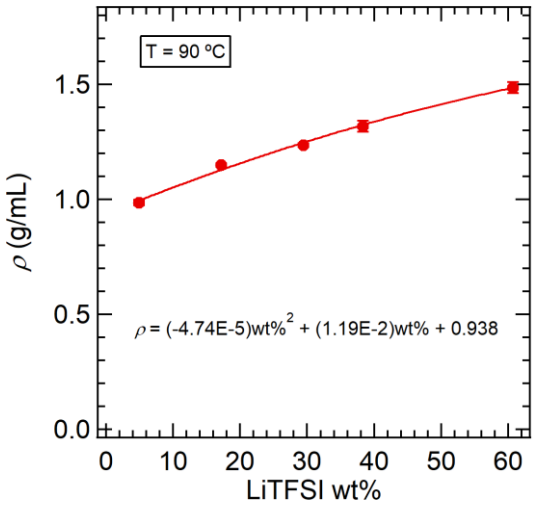

Figure 5.2 Density as a function of LiTFSI wt% for select electrolytes. The red curve is a curve of best fit to interpolate missing electrolyte densities.

5.2.2 Experimental Characterization

All error bars reported are standard deviations of replicate measurements. Measurements were done at 90 °C for all electrolytes and at 30 °C for select electrolytes shown in Table 1.

Conductivity measurements

Ionic conductivity, κ, was measured using a FiveEasy Conductivity Meter F30 (Mettler Toledo). Each measurement was carried out in triplicate.

Ideal transference number measurements

Ideal transference number, $t_{+,id}$, measurements were performed as described in ref. [112]. Assuming Ohm's law, which is a reasonable assumption prior to cell polarization due to a lack of concentration gradients, an initial current, I_Ω, is given by Eq. 5.1:

$$I_\Omega = \frac{\Delta V}{R_T} \tag{5.1}$$

where ΔV is the applied polarization potential and R_T is the total initial cell resistance as measured by ac impedance spectroscopy. Ac impedance data were collected every 20 minutes during applied dc potentials $\pm$ 10 and 20 mV with amplitudes of 5 and 10 mV, respectively. Eq. 5.2 was then used to calculate $t_{+,id}$:[53,54]

$$t_{+,id} = \frac{I_{ss}}{I_\Omega}\left(\frac{\Delta V - I_\Omega R_{i,0}}{\Delta V - I_{ss} R_{i,ss}}\right) \tag{5.2}$$

where I_{ss} is the steady state current, $R_{i,0}$ is the initial interfacial resistance, and $R_{i,ss}$ is the interfacial resistance when I_{ss} is reached.

Restricted diffusion measurements

Restricted diffusion data were measured as described in [112]. Celgard 2500 separators were wetted and stacked to adjust electrolyte thickness. Stacks of 10 and 20 Celgard 2500 separators were used to measure the restricted diffusion coefficients of electrolytes at 30 °C and 90 °C, respectively. The salt diffusion coefficient with in the separator, D_s, is calculated using this technique. In order to obtain the salt diffusion coefficient of the electrolytic phase, the tortuosity, τ, of the separator had to be accounted for:

$$D = \tau D_s. \tag{5.3}$$

Tortuosity has been measured for Celgard 2500 elsewhere and a value of τ = 4.53 ± 0.45 was found.[112] The same value was used in this work to report D.

Concentration cell measurements

Concentration cell measurements were conducted in a similar fashion to that of ref. [112]. One side of the U-cell contained a reference electrolyte of m_{ref} = 1.45 mol/kg, while the other side was filled with electrolytes of varying molalities for measurements at both 30 °C and 90 °C. Both sides of the U-cell were filled with electrolyte such that the heights on both sides were the same, an effort necessary to minimize pressure differences across the glass frit. Strips of lithium (MTI Corp.) were cut and brushed, and then immersed into the two halves of the U-cell. The open-circuit potential, *U*, was monitored with time. The open-circuit potential was monitored for 1 hour, and the reported *U* was averaged over a 5 minute plateau of the open-circuit potential. The potential difference is related to the thermodynamic factor by the following equation:[39]

$$\frac{F(z^+v^+)}{vRT(1-t_+^0)}\frac{dU}{dlnm} = 1 + \frac{dln\gamma_\pm}{dlnm} \tag{5.4}$$

where z^+ is the charge number, v^+ is the number of cations, both of which are 1 for LiFSI, and $\frac{dU}{d\ln m}$ is the change in the open-circuit potential, *U*, with ln(*m*). The salt concentrations studied for 30 °C was limited, thus Eq. 5.5 was used to calculate the thermodynamic factor:

$$\frac{F(z^+v^+)}{vRT(1-t_+^0)}m\frac{dU}{dm} = 1 + \frac{dln\gamma_\pm}{dlnm}. \tag{5.5}$$

Three replicate measurements were performed for data collected at 90 °C for all concentrations reported. One measurement per concentration was taken for data collected at 30 °C.

Transference number calculation

The transference number of the electrolytic phase, t_+^0, was then calculated by combining the above four independent measurements (conductivity, ideal transference number, concentration cells, and restricted diffusion). Balsara and Newman showed that the ideal transference number is related to the cation transference number[70]

$$t_+^0 = 1 - \sqrt{\frac{\frac{F^2Dc}{v\kappa RT}\left(\frac{1}{t_{+,id}}-1\right)}{1+\frac{dln\gamma_\pm}{dlnm}}}. \tag{5.6}$$

Here, *v* is related to the stoichiometric factor and is equal to 2 for a monovalent salt. By combining equations 5.4 and 5.6 The thermodynamic factor can be determined with experimentally measurable quantities

$$\frac{\kappa(z^+v^+)}{vRTDc\left(\frac{1}{t_{+,id}}-1\right)}\left(\frac{dU}{dlnm}\right)^2 = 1 + \frac{dln\gamma_\pm}{dlnm}. \tag{5.7}$$

Combining equations 5.5 and 5.6 gives

$$\frac{\kappa(z^+v^+)}{vRTDc\left(\frac{1}{t_{+,id}}-1\right)}\left(m\frac{dU}{dm}\right)^2 = 1+\frac{dln\gamma_{\pm}}{dlnm}. \tag{5.8}$$

The sign of the open circuit potential depends on convention – some researchers report positive values for *U*, while others report negative values for *U*.[70,93,95,96] This depends on whether the positive or negative lead from the potentiostat is connected to the reference electrolyte. Equations 5.7 and 5.8 are applicable regardless of convention or how the potentiostat is connected to the reference electrolyte. Once the thermodynamic factor is calculated, t_+^0 can be determined. Additionally, the above equation is true for all concentrations, as there are no assumptions about ideality within the calculation of t_+^0.

Limiting current measurements

After conditioning the lithium symmetric cells following a procedure as described in ref. [131], each sample was polarized at all of the following current densities, *i*, for 30 minutes: *i* = 1.0, -2.0, 3.0, and -4.0 mA/cm^2 with the total electrolyte/separator composite thickness, *L* = 0.50 cm. Limiting current data was only collected for *T* = 90 °C. The potential was measured during chronoamperometry every five seconds, and the limiting current was identified when the potential failed to plateau within the measurement timeframe. Once the smallest unsustainable current density and largest sustainable current density was determined (see ref. [131]), additional current densities were applied to the cell in order to obtain higher resolution on the limiting current. Current density increments of 0.2 mA/cm^2 were taken between the absolute values of the smallest unsustainable and largest sustainable *i* and switching between positive and negative current densities. For example, if the smallest unstainable *i* was -4.0 mA/cm^2 and the largest sustainable *i* was 3.0 mA/cm^2, additional current densities of *i* = 3.2, -3.4, 3.6, and -3.8 mA/cm^2 were applied. Negative and positive current densities were used in order to prevent lithium dendritic growth, and thus a short circuit, within the cells.

5.2.3 Steady-state Model

The relationship between i_{ss} and the electrochemical properties of an electrolyte, based on Newman's concentrated solution theory,[39] was derived in ref. [111]. This relationship changes slightly when the electrolyte is contained in a porous separator (we call this the electrolyte/separator composite), and is given by Eq. 5.9 and has been used to predict concentration profiles in other liquid electrolytes[131]

$$\int_{m(x=0)}^{m(x)} \frac{c(m)D_s(m)}{mt_-^0(m)}dm = \frac{i_{ss}l}{Fz_-v_-}\left(\frac{x}{L}\right) \tag{5.9}$$

where *c* is the concentration of the salt in the electrolytic phase in mol/cm^3, D_s is the salt diffusion coefficient measured by restricted diffusion on the electrolyte/separator composite, *m* is the molality, t_-^0 is the anion transference number relative to the velocity of the solvent ($t_-^0 = 1 -$

t_+^0), z_- is the charge number on the anion, ν_- is the number of anions the salt disassociates into, l is the thickness of the electrolyte/separator composite, x/l is the normalized thickness, and F is Faraday's constant (the transference number is unaffected by the presence of the separator). All of the ion transport properties depend on salt concentration, as indicated in Eq. 5.9. During an experiment, the average salt concentration of the electrolyte, m_{av}, is controlled. The molality profile predicted by Eq. 5.9 must be averaged from $x = 0$ to $x = L$ to ensure that the model predicted average concentration is equal to m_{av}.

5.3 Results and Discussion

The ionic conductivity, κ, salt diffusion coefficient, D, and the ideal transference number, $t_{+,id}$ were determined through three independent experiments as described in the Experimental and Theoretical Details section. The three aforementioned transport parameters are shown in Fig. 5.3 as a function of salt concentration, m_{av}, for both T = 30 °C and 90 °C. The blue squares are data collected at 30 °C and red circles are data collected at 90 °C. The solid curves are fits through the data. Parameters for the fitting functions are listed in Table 5.2 for both temperatures. The fit for D at T = 30 °C follows a power law in place of a polynomial function, also shown in Table 5.2.

Table 5.2 The best-fit polynomial, or power law, equations for all transport properties at T = 30 °C and 90 °C in tetraglyme electrolytes.

$P_{tetraglyme} = k_0 + k_1 m + k_2 m^2 + k_3 m^3$				
$P_{\text{Tetraglyme}}$	k_0	k_1	k_2	k_3
κ (90 °C)	-2.32 x 10^{-4}	3.08 x 10^{-1}	-1.39	1.71
D (90 °C)	3.50 x 10^{-6}	-4.66 x 10^{-7}	-2.33 x 10^{-8}	-
$t_{+,\text{id}}$ (90 °C)	0.704	-0.250	2.44 x 10^{-2}	-
κ (30 °C)	-1.03 x 10^{-3}	1.24 x 10^{-3}	-2.44 x 10^{-4}	-
D (30 °C)	= 3.93 x $10^{-7} m^{0.603}$			
$t_{+,\text{id}}$ (30 °C)	0.832	0.255	2.35 x 10^{-2}	-

In Fig. 5.3a, κ as a function of salt concentration is plotted. At 30 °C, κ increases with increasing concentration, with a maximum of κ = 3.21 x 10^{-3} S/cm at m_{av} = 1.45 mol/kg. The conductivity is approximately the same at both m_{av} = 0.18 and 5.37 mol/kg. At 90 °C, κ dramatically increases with increasing m_{av} at low concentrations, approaches a maximum of κ = 2.02 x 10^{-2} S/cm at m_{av} = 2.16 mol/kg followed by a shallow drop in conductivity with increasing concentration. As expected, conductivity is significantly higher at T = 90 °C than at 30 °C. Additionally, the conductivity behavior at the two temperatures reported is qualitatively different from one another. At T = 90 °C, in the limit of high salt concentration, while κ decreases, it does not equal that of the lowest salt concentration studied. The salt diffusion coefficient, D, of the electrolytic phase, as measured by the restricted diffusion technique, as a function of salt concentration, is

shown in Fig. 3b for both T = 30 °C and 90 °C. The tortuosity of the separator was accounted for when reporting D in Fig. 5.3b (see Eq. 5.3). For both temperatures, the salt diffusion coefficient monotonically decreases with increasing salt concentration. Over the measured salt concentration window, D decreases by about an order of magnitude for both temperatures. The decrease in D is expected with increasing m_{av} as the system viscosity increases with increasing m_{av}. The salt diffusion coefficient at 90 °C is higher than the measured values at 30 °C at all salt concentrations. Fig. 5.3c is a plot of the ideal transference number, $t_{+,id}$, as a function of m_{av} for T = 30 °C and 90 °C. For both temperatures, $t_{+,id}$ decreases monotonically as a function of increasing salt concentration. The ideal transference number begins at a maximum of $t_{+,id}$ = 0.75 at m_{av} = 0.18 mol/kg and decreases to a minimum of $t_{+,id}$ = 0.15 at m_{av} = 5.37 mol/kg. For 90 °C, $t_{+,id}$ starts at a maximum of $t_{+,id}$ = 0.67 at m_{av} = 0.18 mol/kg and decreases to 0.06 at the highest salt concentration studied of m_{av} = 5.37 mol/kg. While κ and D increase with increasing temperature, $t_{+,id}$ decreases with increasing temperature within the studied salt concentration window. The ideal transference number at low salt concentrations is significantly larger than the values reported for higher molecular weight analogs of tetraglyme.[58,95,132]

The open circuit potential, U_0, for concentration cells for T = 90 °C is shown in Fig. 5.4a as a function of the natural log of m_{av}. A polynomial fit, shown as the red curve, is used and takes the following functional form:

$$U_0(m) = -3.883\ (\ln m)^4 - 14.121(\ln m)^3 - 24.346(\ln m)^2 - 34.397 \ln m + 18.706. \tag{5.10}$$

Fig. 5.4b is a plot of U_0 vs. m_{av} for T = 30 °C. The blue curve is the following polynomial fit:

$$U_0(m) = 1.632m^2 - 65.708m + 75.301. \tag{5.11}$$

The open circuit potential equals zero when both sides of the concentration cell contains the reference electrolyte ($m_{av,ref}$ = 1.45 mol/kg). It should be noted that the magnitude of the open circuit potential for the lowest (m_{av} = 0.18 mol/kg) and highest (m_{av} = 5.37 mol/kg) concentrations studied for 30 °C is greater than that of 90 °C. However, this may be an artifact of the measurement as only one measurement per concentration was done for 30 °C whereas three replicates were conducted for 90 °C.

The thermodynamic factor, T_f, or $1 + \frac{d \ln \gamma_{\pm}}{d \ln m}$, for 90 °C is calculated by Eq. 5.7 and the polynomial fits in Eq. 5.10 and those of Table 5.2. T_f for T = 30 °C is calculated with Eq. 5.8 and the polynomial fits in Eq. 5.11 and those in Table 5.2. The thermodynamic factor for both temperatures is shown in Fig. 5.5. At 90 °C, T_f monotonically increases with increasing salt concentration. The thermodynamic factor for T = 30 °C, however, is more complex – T_f goes through a shallow maximum at m_{av} = 2.88 mol/kg. In addition, T_f at 90 °C is less than that of 30 °C at concentrations below ca. 4 mol/kg.

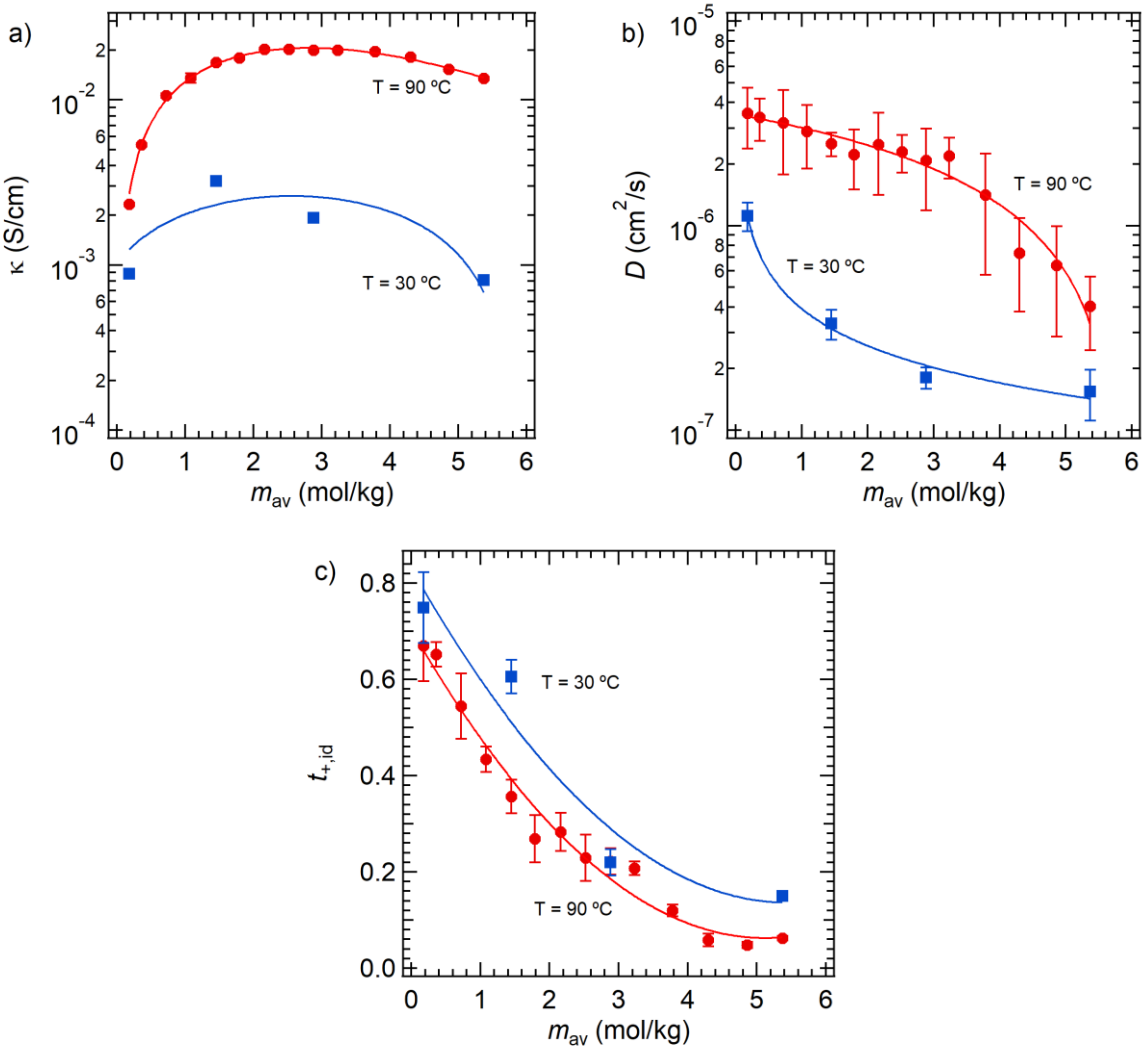

Figure 5.3 Electrochemically determined ion transport properties of tetraglyme/LiTFSI (electrolytic phase) as a function of molality and temperature. Squares and circles are experimental measurements, and the solid curves are polynomial fits to the data. a) Conductivity measured with a conductivity probe, b) the salt diffusion coefficient as measured by the restricted diffusion method, and c) the ideal transference number as measured by the steady-state current method.

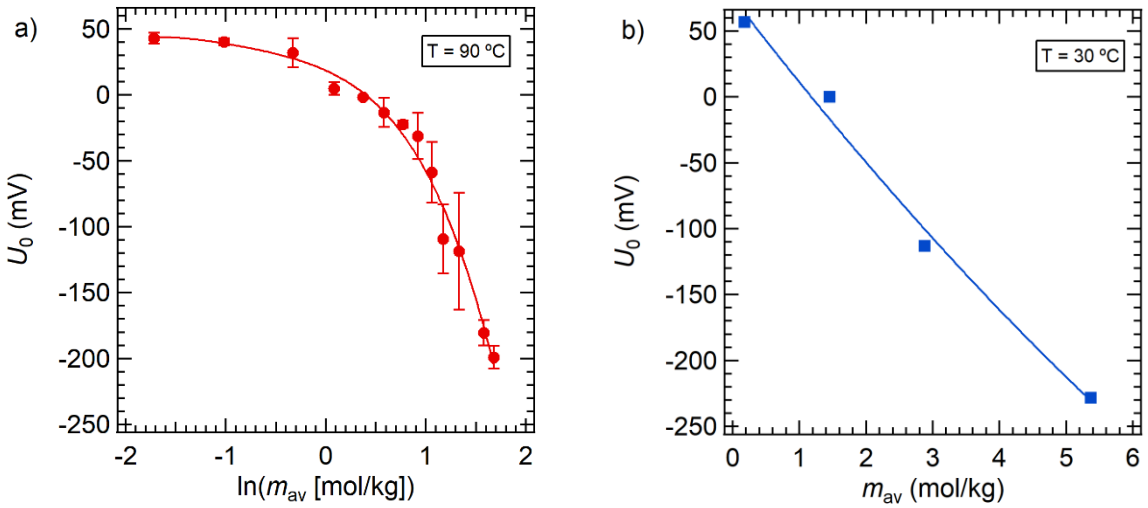

Figure 5.4 Open circuit potential as a function of salt concentration obtained using concentration cells for a) 90 °C and b) 30 °C. Note that the x-axis for 90 °C is $\ln(m_{av})$ whereas that of 30 °C is m_{av} to ensure that the polynomial fit is downward sloping over the experimental window.

The cation transference number with respect to the velocity of the solvent, t_+^0, for 90 °C, calculated using Eq. 5.7, the polynomial fits in Figs 5.3, and data in Fig. 5.5, is shown in red in Fig. 5.6. The cation transference number with respect to the velocity of the solvent for 30 °C, calculated with Eq. 5.8, the polynomial fits in Fig. 5.3, and data in Fig. 5.5, is shown in blue in Fig. 5.6. In general, for both temperatures studied, t_+^0 has a non-monotonic dependence on increasing salt concentration. At 30 °C, t_+^0 goes through a shallow maximum at m_{av} = 1.45 mol/kg, and becomes negative at m_{av} = 5.37 mol/kg. In contrast, t_+^0 at 90 °C is negative at m_{av} = 0.36 mol/kg, followed by positive values for the remaining concentrations that were studied. In the inset, at the lowest salt concentration of m_{av} = 0.18 for 90 °C, t_+^0 is highly negative. This is most likely due to the derivative of the open circuit potential best-fit curve (Eq. 5.10). The derivative to Eq. 5.10 is positive at m_{av} = 0.18 mol/kg even though one would expect a negative derivative with increasing salt concentration. The transference number behavior seen here is qualitatively different from the values that have been reported for high molecular weight poly(ethylene oxide) (PEO) mixed with LiTFSI.[94,95,133]

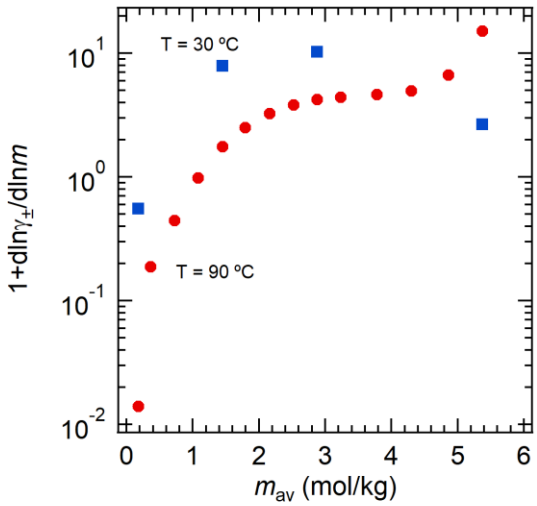

Figure 5.5 The thermodynamic factor as a function of salt concentration for 30 °C and 90 °C.

Our objective is to predict salt concentration profiles and compare experimental limiting current data with theoretical predictions for mixtures of tetraglyme and LiTFSI at 90 °C. We chose to model only the data using 90 °C as we measured transport parameters at finer resolutions of m_{av}. Using the experimental transport properties reported in Figs. 5.3 and 5.6, we can predict the theoretical salt concentration profiles for a given steady-state current density, i_{ss}, thickness, L, and average starting salt concentration, $m_{av,}$ in Li symmetric cells. The constant- and limiting-current experiments were conducted in coin cells, which required an electrolyte/separator composite. In order to account for the tortuosity, τ, of the separator, the salt diffusion coefficient within the electrolyte/separator composite, D_s, was used. In Fig. 5.7, we show a fourth order polynomial fit to the product appearing on the left-hand-side of Eq. 5.8

$$\frac{c(m)D_s(m)}{mt_-^0(m)} = k_0 + k_1 m + k_2 m^2 + k_3 m^3 + k_4 m^4 \tag{5.12}$$

with fitting parameters

$$k_0 = 2.93\text{x}10^{-10} \quad k_1 = 1.23\text{x}10^{-9} \quad k_2 = -6.83\text{x}10^{-10}$$
$$k_3 = 1.22\text{x}10^{-10} \quad k_4 = -7.07\text{x}10^{-12}$$

where t_-^0 is equal to $1 - t_+^0$, D_s is in cm^2/s, c is in mol/cm^3, and m is in mol/kg. The parameters apply to the range of $0.36 \leq m \leq 5.37$ for $T = 90$ °C.

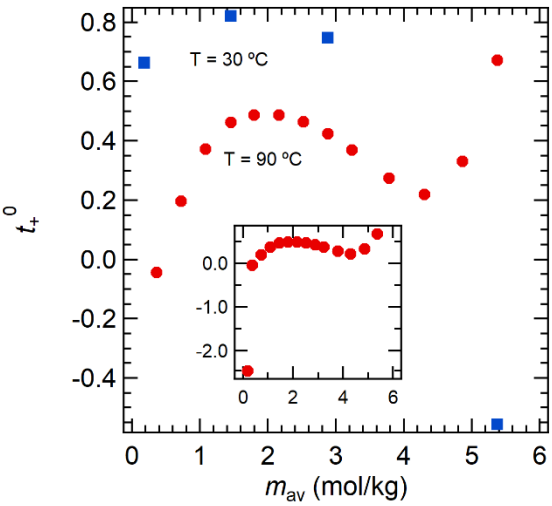

Figure 5.6 The transference number, t_+^0, based on concentrated solution theory as a function of salt concentration in the range m_{av} = 0.18 to 5.37 mol/kg for 30 °C (blue) and in the range m_{av} = 0.36 to 5.37 mol/kg for 90 °C (red). The inset includes data at the lowest salt concentration, m_{av} = 0.18 mol/kg for 90 °C. The remainder of the paper will focus on the range m_{av} = 0.36 to 5.37 mol/kg for 90 °C.

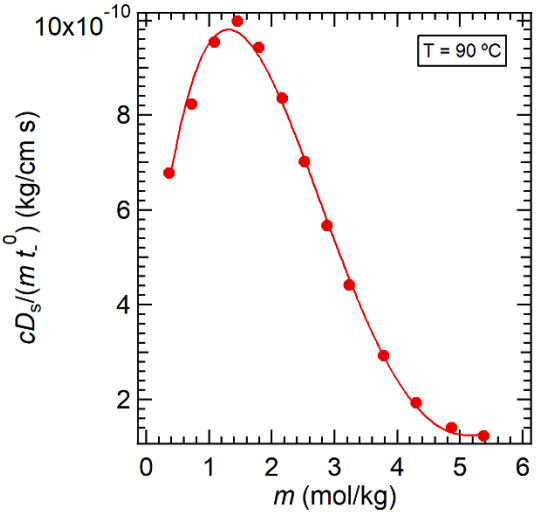

Figure 5.7 Fit of the integrated term of Eq. 5.9, $\frac{cD_s}{mt_-^0}$, as a function of salt concentration for data at 90 °C. The solid curve shows the least-squares polynomial fit given by Eq. 5.12.

Fig. 5.8 shows the salt concentration profiles from x/L = 0 (anode side) to x/L = 1 (cathode side) for a range of mixtures of tetraglyme/LiTFSI. Three starting concentrations of m_{av} = 1.45, 2.16, and 3.23 mol/kg are shown in Figs. 5.8a, b, and c, respectively. In addition, three normalized current densities, $i_{ss}L$, are used for each m_{av} shown: 0.001 (green curve), 0.01 (yellow curve), and 0.1 mA/cm (purple curve). A normalized current density, $i_{ss}L$, is used as it allows for comparison across different systems regardless of cell geometry. The concentration profiles were determined by numerically solving Eq. 5.9 using the fitted Eq. 5.12. It is evident from Fig. 5.8

that in the limit of small $i_{ss}L$ (0.001 mA/cm), the concentration profiles are approximately linear and the gradients are small for all three m_{av}. As larger $i_{ss}L$ are applied, the salt concentration gradients become steeper, as shown in yellow ($i_{ss}L$ = 0.01 mA/cm) and purple ($i_{ss}L$ = 0.1 mA/cm). The concentration profile for $i_{ss}L$ = 0.1 mA/cm for m_{av} = 3.23 mol/kg in Fig. 5.8c shows the largest curvature. The magnitude of the difference between the predicted salt concentration at x/L = 0 and m_{av} ($|m(x/L = 0) - 3.23|$ = 1.86 mol/kg) is greater than the magnitude of the difference between the predicted salt concentration at x/L = 1 and m_{av} ($|m(x/L = 1) - 3.23|$ = 0.96 mol/kg). This may be attributed to a decrease in t_+^0 between m = 2.52 and 5.37 mol/kg.

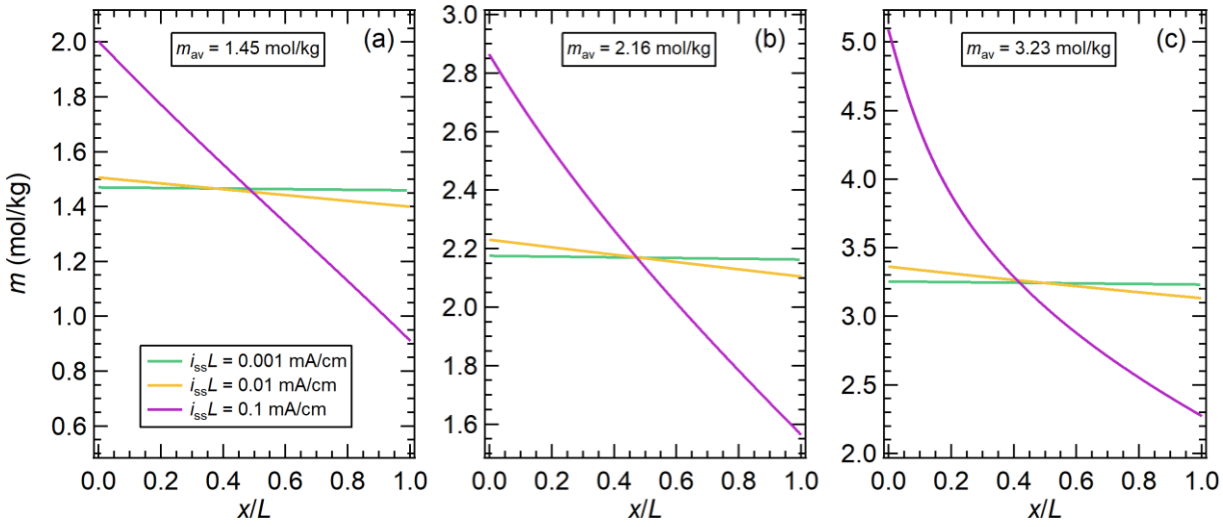

Figure 5.8 Model predicted concentration profiles of LiTFSI in tetraglyme in a lithium symmetric cell as solved for by Eq. 5.9 for three different starting salt concentrations at 90 °C: a) m_{av} = 1.45, b) m_{av} = 2.16, and c) m_{av} = 3.23 mol/kg.

The normalized limiting current density, $i_{limit}L$, can be predicted within an electrolyte using model predicted concentration profiles. To accomplish this, for a given m_{av}, a range of $i_{ss}L$ are used to predict the salt concentration profiles, and m at the cathode surface (x/L = 1) is extracted at each $i_{ss}L$. The concentration at the cathode, $m(x/L = 1)$, is plotted against $i_{ss}L$, and the points are fit to a curve. The curve is extrapolated to $m(x/L = 1) = 0$ mol/kg, at which point the normalized limiting current density, $i_{limit}L$, is reached. An example of such an analysis is shown in Fig. 5.9. The purple triangles are model predicted concentrations at x/L = 1 for a range of $i_{ss}L$ and the dotted curve is a polynomial fit. In Fig. 5.9, a starting concentration of m_{av} = 1.45 mol/kg was used for Fig. 5.9a and m_{av} = 2.16 mol/kg for Fig. 5.9b. The green squares are model predicted concentrations at the anode surface (x/L = 0), which is an important consideration as previous work has suggested that salt precipitation on the anode surface can lead to cell failure.[131] The solubility limit of LiTFSI in tetraglyme was not measured. Note that at a starting concentration of m_{av} = 2.16 mol/kg, the anode surface concentration departs from m_{av} at high $i_{ss}L$ much more so than that of the cathode surface. This approach utilizes concentrated solution theory (CST).

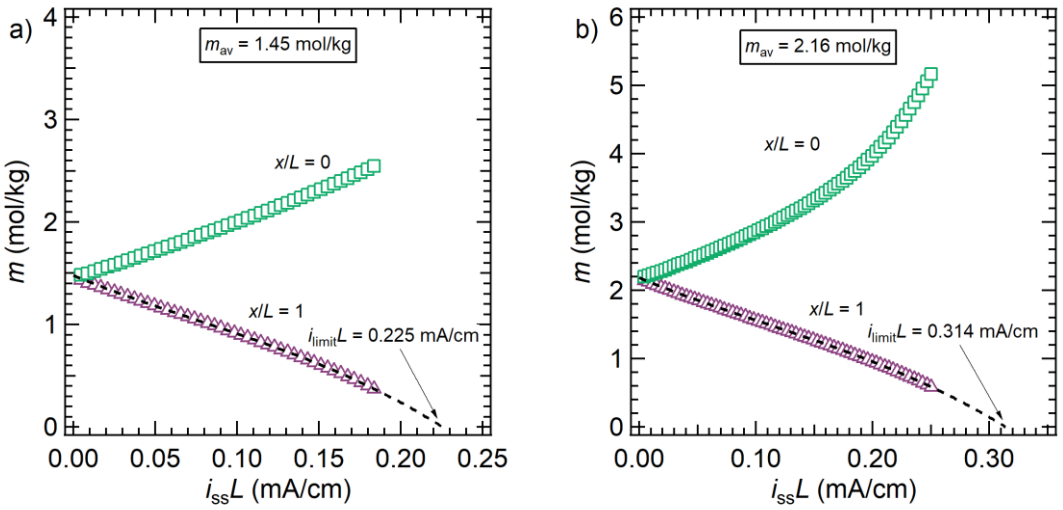

Figure 5.9 Concentration predictions at the cathode (x/L = 1) and anode (x/L = 0) for varying $i_{ss}L$ values for electrolytes with average concentrations a) m_{av} = 1.45 and b) m_{av} = 2.16 mol/kg. The black dashed curve shows a least-squares polynomial fit, which was extrapolated to m = 0 mol/kg to determine the normalized limiting current density (marked as $i_{limit}L$). The anode concentration predictions are shown to highlight the rapid approach to high concentrations for electrolytes with concentrations greater than 1.45 mol/kg.

Experimental measurements of limiting current as a function of salt concentration were obtained using the procedures described in Limiting current measurements under the Experimental Characterization section. In Figure 5.10, the experimental normalized limiting current density, $i_{limit}L$, is plotted as black circles for six concentrations. Each point represents the average of three replicate measurements, however the error bars are smaller than the symbols. In general, $i_{limit}L$ decreases with increasing salt concentration, with the exception at m_{av} = 3.78 mol/kg. One expects the normalized limiting current density to increase with increasing salt concentration, and such a result was seen in electrolytes comprised of PEO (MW = 35 kg/mol) and LiTFSI.[134] One possible explanation for the decrease in $i_{limit}L$ with increasing m_{av} could be due to salt precipitation at the anode surface prior to salt depletion at the cathode surface. However, as mentioned earlier, the solubility limit of LiTFSI in tetraglyme has not been measured in this work.

We can predict the limiting current using dilute solution theory (DST)[39]

$$i_{limit}L = \frac{2c_{av}D_S F}{1 - t_{+,id}} \tag{5.13}$$

where c_{av} is the average electrolyte salt concentration in mol/cm^3. Eq. 5.13 was derived using DST, thus the ideal transference number, $t_{+,id}$, is used to calculate $i_{limit}L$. In Fig. 5.10, predicted $i_{limit}L$ from DST and CST are plotted and shown as green open circles and red filled circles, respectively. Neither DST nor CST predictions capture the experimental qualitative behavior. Both approaches predict maximum normalized limiting current densities at concentrations greater than the experimental maximum. However, DST more closely approximates the

experimental $i_{limit}L$ observed at m_{av} = 0.72 mol/kg, whereas CST more closely predicts the experimental $i_{limit}L$ at m_{av} = 4.30 mol/kg.

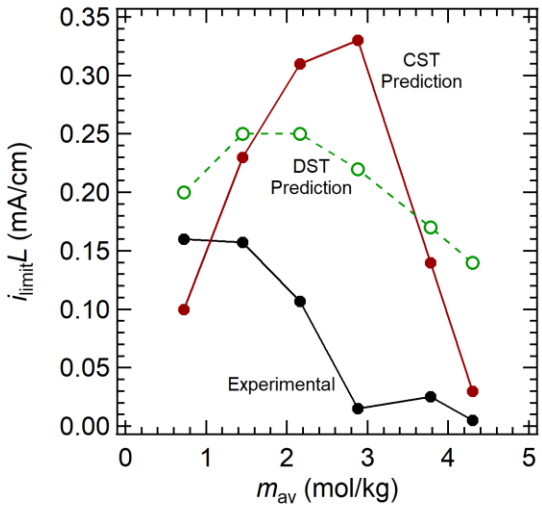

Figure 5.10 A comparison of normalized limiting current density ($i_{limit}L$) values predicted by concentrated solution theory (CST) (Eq. 5.8 and 5.11), dilute solution theory (DST) (Eq. 5.12), and experimental values (black filled circles) as a function of salt concentration, m_{av}.

5.4 Conclusion

The maximum current, and therefore power, a battery can supply, is, in part, limited by the maximum current that can be drawn through the electrolyte. The maximum current is known as the limiting current. The limiting current can be predicted if transport parameters for a wide range of salt concentrations are measured. In this work, a complete set of ion transport parameters, as a function of salt concentration, were determined for electrolytes comprised of LiTFSI and tetraglyme at 30 °C and 90 °C. The measured parameters were conductivity, κ, salt diffusion coefficient, D, as measured by the restricted diffusion technique, ideal transference number, $t_{+,id}$, measured using the steady-state current method, and the thermodynamic factor, T_f, using concentration cells combined with the aforementioned transport properties. These four measurements were combined to calculate the cation transference number with respect to the velocity of the solvent, t_+^0, based in Newman's concentrated solution theory. We find that t_+^0 is higher at 30 °C than at 90 °C at low and moderate concentrations. At 30 °C, t_+^0 drops below zero at the highest concentration studied, m_{av} = 5.37 mol/kg, whereas it remains positive at 90 °C beyond m_{av} = 0.36 mol/kg.

The electrochemical data at 90 °C was used to predict concentration profiles in Li | tetraglyme / LiTFSI | Li symmetric cells for a range of starting salt concentrations, m_{av}. The limiting current was estimated by using the model-predicted concentrations at the cathode surface, and a non-monotonic dependence of limiting current with increasing m_{av} was found. Dilute solution theory was also utilized to estimate the limiting current, and it, too, had a non-monotonic dependence with increasing m_{av}. The predictions were compared to experimental results and both models

failed to accurately capture the experimental behavior. This may be due to a salt solubility limitation at the anode surface. Further work is necessary in determining the solubility limit of LiTFSI in tetraglyme at 90 °C.

5.5 Acknowledgements

This work was intellectually led by the Joint Center for Energy Storage Research (JCESR), an Energy Innovation Hub funded by the U.S. Department of Energy (DOE), Office of Science, Basic Energy Sciences (BES), under Contract No. DEAC02-06CH11357.

5.6 Nomenclature

c	Concentration (mol/cm^3 or mol/L)
D	Salt diffusion coefficient of electrolytic phase (cm^2/s)
D_s	Salt diffusion coefficient of electrolyte in separator (cm^2/s)
F	Faraday's constant (96,485 C/mol)
I_{ss}	Steady-state current (mA)
I_Ω	Initial current calculated using Ohm's law (mA)
i_{ss}	Steady-state current density (mA/cm^2)
i_{limit}	Limiting current density (mA/cm^2)
L	Thickness of electrolyte/separator (cm)
m_{av}	Average molality (mol/kg)
m	Molality (mol/kg)
R	Ideal gas constant (J/mol K)
$R_{i,0}$	Resistance of electrolyte/electrode interface initially, prior to polarization (Ω)
$R_{i,ss}$	Resistance of solvent/electrode interface when Iss reached (Ω)
R_s	Resistance of electrolyte/separator composite (Ω)
R_T	Total resistance of cell (R_s + $R_{i,0}$) (Ω)
T	Temperature (K)
T_f	Thermodynamic factor
t_+^0	Cation transference number relative to the solvent velocity. Obtained using the Balsara and Newman method
t_-^0	Anion transference number relative to the solvent velocity; $t_-^0 = 1 - t_+^0$
$t_{+,id}$	Ideal transference number using steady-state current method
x	Position (cm)
U_0	Open-circuit voltage (mV)
z^+	Cation charge
$1 + \frac{dln\gamma_\pm}{dlnm}$	Thermodynamic factor

Greek

$\gamma_\pm$	Mean molal activity coefficient of the salt
κ	Conductivity of the electrolytic phase; (S/cm)
v	Stoichiometric parameter = 2 for univalent salts ($= v^+ + v^-$)

v^i	Number of cations/anions per molecule of salt ($i = +$ or $-$)
ΔV	Dc polarization potential (mV)
ρ	Density (g/mL)
τ	Tortuosity of the separator

6 Comparing Model and Experimental Potential Drops in Propylene Carbonate Electrolytes

6.1 Introduction

During the operation of a lithium-ion battery, salt concentration gradients develop within the electrolyte. These concentration gradients, and thus concentration overpotential, are further exacerbated in the limit of high dc currents, and can ultimately lead to cell failure.[13,111,134] In order to understand these concentration gradients, Onsager reciprocal relations require $n(n\text{-}1)/2$ transport properties to be measured, where n represents the number of components within the electrolyte.[38,39] For a binary electrolyte (n = 3), in order to fully characterize ion transport, the thermodynamic factor, T_f, and three independent transport parameters in the form of conductivity, κ, salt diffusion coefficient, D, and the rigorous cation transference number, t_+^0 must be characterized as a function of salt concentration. Once these properties are elucidated for a given electrolyte, the potential drop within the electrolyte, which is a combination of conductivity and concentration overpolarization, can be modeled using Newman's concentrated solution theory.[39]

Understanding ion transport within electrolytes is paramount to enabling next generation lithium-based technology, however the vast majority of the literature measures one or two properties.[58,126,135–138] The transference number is especially difficult to measure and the most common technique used is the steady-state current method, as pioneered by Bruce and Vincent, but it is rooted in dilute solution theory.[53,54] The results of this method cannot be assumed to apply to systems of finite concentration. Concentrated solution theory has been applied to some nonaqueous liquid electrolytes in order to elucidate their transport parameters.[83,112,139–142] Landesfeind and Gasteiger recently reported on mixtures of lithium hexafluorophosphate ($LiPF_6$) and two solvents using Newman's concentrated solution theory.[140] However, they assumed that t_+^0 and T_f were constant with respect to concentration in their calculation. In addition, they used a plasma treated separator, which improves electrolyte wettability, and inherently influences ion motion within their electrolyte, thus adding more uncertainty to the reported properties.[143,144] Hou and Monroe recently reported a complete suite of ion transport properties on mixtures of lithium hexafluorophoshate ($LiPF_6$) and propylene carbonate (PC).[139] In order to measure the salt diffusion coefficient, they used a free-standing lithium symmetric cell, which will increase convection effects compared to when a separator is used.[93,142]

In this work, we report on a complete set of ion transport properties for binary mixtures of lithium bis(fluorosulfonyl)imide (LiFSI) and PC and $LiPF_6$ and PC. The chemical structures of the three components are shown in Fig. 6.1. We studied κ, D, t_+^0, and T_f between 0.25 and 2.00 M at room temperature. We apply Newman's concentrated solution theory to predict salt concentration and potential profiles as a function of starting salt concentration and current density in lithium symmetric cells for mixtures of LiFSI and PC at steady-state. The electrolyte potential drop predictions are compared to experimental results without the use of any adjustable parameters.

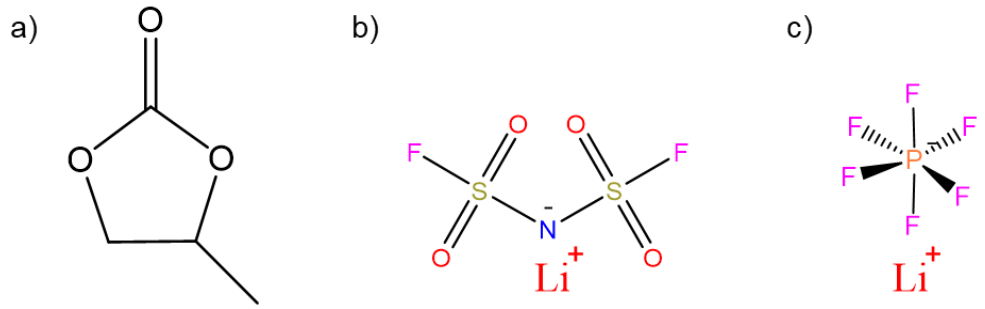

Figure 6.1 a) PC, b) LiFSI, and c) $LiPF_6$.

6.2 Experimental & Theoretical Details

6.2.1 Electrolyte Preparation

Propylene carbonate (PC) and lithium hexafluorophosphate ($LiPF_6$) was purchased from Gotion. Both chemicals were ≥ 99.9% pure, as confirmed by certificate of analysis forms. Lithium bis(fluorosulfonyl)imide (cat. no. 097602) (LiFSI) was purchased from Oakwood Products, Inc. and was ≥ 99% pure, as confirmed by a certificate of analysis form. PC and $LiPF_6$ were used as received, whereas LiFSI was dried at 120 °C under dynamic vacuum for three days inside a glovebox antechamber. The salts, solvent, and prepared electrolytes were stored and used within an argon filled Vac glovebox with H_2O and O_2 concentrations kept below 1 ppm.

Table 6.1 Values of LiFSI wt%, molality, and calculated concentration for electrolytes studied at room temperature.

LiFSI wt%	m_{av} (mol/kg)	c_{av} (mol/L)
3.92	0.22	0.25
7.67	0.44	0.50
11.27	0.68	0.75
14.72	0.92	1.00
18.06	1.18	1.25
21.29	1.45	1.50
27.45	2.02	2.00

In order to form electrolytes, a predetermined amount of LiFSI or $LiPF_6$ was added to a known mass of PC. Once the salt was added, the electrolytes were placed on a magnetic stirrer and were allowed to mix for 12 hours or more using a magnetic stir bar at room temperature. Salt concentration for electrolytes ranged from c_{av} = 0.25 to 2.00 M. Values of salt wt %, molality, m_{av}, and concentration, c_{av}, for LiFSI and $LiPF_6$ based electrolytes are shown in Table 6.1 and Table 6.2, respectively. Here, m_{av} is the average electrolyte molality and c_{av} is the average electrolyte concentration.

Table 6.2 Values of $LiPF_6$ wt%, molality, and calculated concentration for electrolytes studied at room temperature.

$LiPF_6$ wt%	m_{av} (mol/kg)	c_{av} (mol/L)
3.10	0.21	0.25
6.06	0.42	0.50
8.90	0.64	0.75
11.63	0.87	1.00
14.27	1.10	1.25
16.82	1.33	1.50
21.68	1.82	2.00

The density, ρ, for select salt concentrations was obtained by filling a differential scanning calorimetry (DSC) sample pan (TA Instruments) with a known volume of 40 uL and measuring the mass of the electrolyte at room temperature inside an argon filled glovebox. The density was interpolated for unmeasured electrolytes using a curve of best fit, shown in Figs. 6.2a and 6.2b, for mixtures of LiFSI and PC, and $LiPF_6$ and PC, respectively.

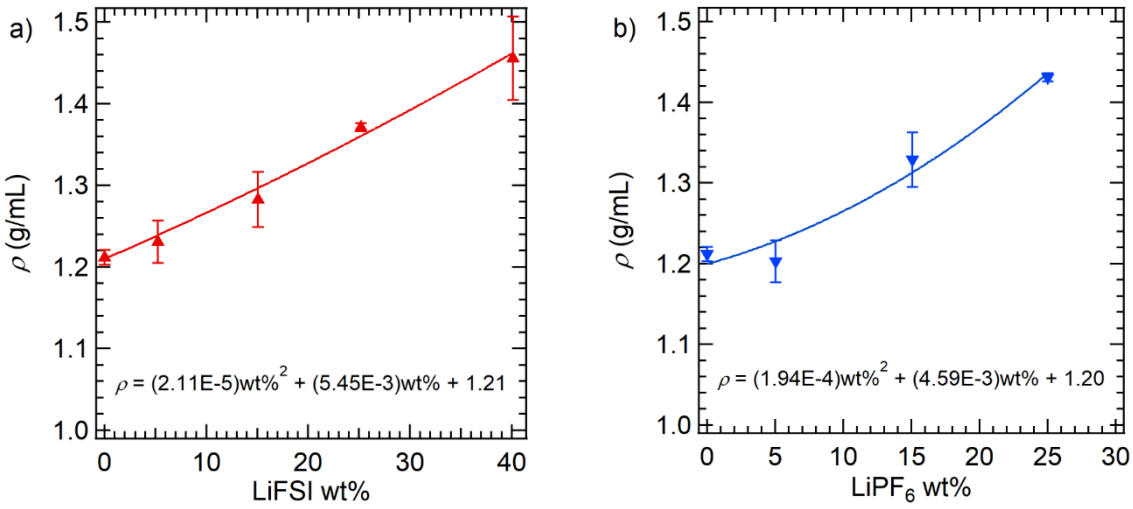

Figure 6.2 Density as a function of a) LiFSI wt% and b) $LiPF_6$ for select electrolytes. The solid curves represent curves of best fit to interpolate missing electrolyte densities.

6.2.2 Experimental Characterization

All electrochemical characterization experiments that utilized coin cells were conducted in an environmental chamber at T = 25 °C. Concentration cells were carried out inside an argon filled glove box at room temperature.

Conductivity measurements

Ionic conductivity of the electrolytic phase, κ, was measured using a FiveEasy Conductivity Meter F30 (Mettler Toledo). Each measurement was carried out in triplicate. The conductivity of neat propylene carbonate was measured to be 6.33 x 10^{-7} S/cm, which we assume is due to impurities. We treat this value as background and subtract 6.33 x 10^{-7} S/cm from the other measured conductivity values.

Ideal transference number measurements

Ideal transference number, $t_{+,id}$, samples were prepared by sandwiching two electrolyte soaked separators, Whatman GF/F (GE Healthcare), with a lithium disc, cut from lithium chips (MTI corp.), on either side. The diameter of the 150 μm thick Li disc was 12.7 mm. Three replicate cells were produced for each electrolyte. Data were collected on Bio-Logic VMP3 and VMP-300 potentiostats. Assuming Ohm's law, which is a reasonable assumption prior to cell polarization due to a lack of concentration gradients, an initial current, I_Ω, is given by Eq. 6.1:

$$I_\Omega = \frac{\Delta V}{R_T} \tag{6.1}$$

where ΔV is the applied polarization potential and R_T is the total initial cell resistance as measured by ac impedance spectroscopy. Ac impedance data were collected every 20 minutes during applied dc potentials $\pm$ 5 mV with an amplitude of 2.5mV. Low dc potentials were required in order to ensure a stable current response. Applied dc potentials greater than 5 mV led to significant interfacial impedance changes, which causes an improperly measured ideal transference number. Eq. 6.2 was then used to calculate $t_{+,id}$.[53,54]

$$t_{+,id} = \frac{I_{ss}}{I_\Omega}\left(\frac{\Delta V - I_\Omega R_{i,0}}{\Delta V - I_{ss}R_{i,ss}}\right) \tag{6.2}$$

where I_{ss} is the steady state current, $R_{i,0}$ is the initial interfacial resistance, and $R_{i,ss}$ is the interfacial resistance when I_{ss} is reached.

Restricted diffusion measurements

Diffusion coefficients were measured using the restricted diffusion technique.[89,90] Lithium electrodes (thickness 150 μm, diameter 12.7 mm) sandwiched two stacked electrolyte soaked Whatman GF/F separators and hermetically sealed in CR2032 coin cells (Pred Materials). Dc potentials of ±5 mV were used to polarize the cell until a steady-state current was realized. The potential was then removed and the cells were allowed to relax for 20 minutes while the open-circuit potential, *U*, was measured every 5 seconds. Porous separators were used in order to control for convection, an important precaution for liquid electrolytes.[91] The relaxation profiles were fit to Eq. 6.3

$$U(t) = k_0 + ae^{-bt} \tag{6.3}$$

where a and b are fit parameters and k_0 is an empirically determined offset voltage. The salt diffusion coefficient within the separator, D_s, is related to b by

$$D_s = \frac{L^2 b}{\pi^2} \tag{6.4}$$

where L is the thickness of the separator stack. The lower time limits of the fits are such that $\alpha = D_s t/L^2 > 0.03$.[92] Traditionally, an $\alpha = 0.05$ is used, however, the OCV relaxation time is short, hence a smaller value of α, which is still large enough for Eq. 6.3 to apply.

Whatman GF/F separators are compressible, thus their thickness changes under the compressive force of a coin cell assembly. In order to calculate L, ac impedance spectroscopy was conducted on the lithium symmetric cells in order to obtain the resistance of the electrolyte/separator composite, R_s. The conductivity of the electrolytic phase, κ, is related to the conductivity of the separator by Eq. 6.4

$$\kappa = \frac{\tau}{\phi_c}\kappa_s = \frac{\tau}{\phi_c}\frac{L}{R_s A} \tag{6.5}$$

where τ is the separator tortuosity, A is the active surface area of the electrode, and ϕ_c is the volume fraction of the conducting phase in the separator. The tortuosity for the separator was found to be $\tau = 1$, and the conducting phase volume fraction was found to be $\phi_c = 0.87 \pm 0.06$ using methods described in ref. [112]. Eq. 6.5 was rearranged to solve for L

$$L = \frac{\phi_c}{\tau}\kappa R_s A. \tag{6.6}$$

This paper reports the diffusion coefficient of the salt in the electrolytic phase, D, and in order to do so, the tortuosity of the separator had to be taken into consideration:

$$D = \tau D_s. \tag{6.7}$$

Concentration cell measurements

Concentration cell measurements were conducted in a similar fashion to that of ref. [112]. One side of the U-cell contained a reference electrolyte of $m_{ref} = 0.92$ mol/kg for LiFSI based electrolytes and $m_{ref} = 0.87$ mol/kg for $LiPF_6$ based electrolytes. The other side was filled with LiFSI or $LiPF_6$ based electrolytes of varying molalities. Both sides of the U-cell were filled with electrolyte such that the heights on both sides were the same, an effort necessary to minimize pressure differences across the glass frit. Strips of lithium (MTI Corp.) were cut and brushed, and then immersed into the two halves of the U-cell. The open-circuit potential, U, was monitored with time. The open-circuit potential was monitored for 1 hour, and the reported U was averaged over a 5 minute plateau of the open-circuit potential. The potential difference is related to the thermodynamic factor by the following equation:[39]

$$\frac{F(z^+v^+)}{vRT(1-t_+^0)}\frac{dU}{dlnm} = 1 + \frac{dln\gamma_\pm}{dlnm} \tag{6.8}$$

where z^+ is the charge number, v^+ is the number of cations, both of which are 1 for LiFSI and $LiPF_6$, and $\frac{dU}{d\ln m}$ is the change in the open-circuit potential, U, with ln(m).

Two replicate measurements were performed for all concentrations studied, with the exception of the LiFSI electrolyte of m_{av} = 0.22 mol/kg, where one measurement was performed.

Transference number calculation

The transference number of the electrolytic phase, t_+^0, was then calculated by combining the above four independent measurements (conductivity, ideal transference number, concentration cells, and restricted diffusion). Balsara and Newman showed that the ideal transference number is related to the cation transference number relative to the solvent velocity[70]

$$t_+^0 = 1 - \sqrt{\frac{\frac{F^2Dc}{v\kappa RT}\left(\frac{1}{t_{+,id}}-1\right)}{1+\frac{dln\gamma_\pm}{dlnm}}}. \tag{6.9}$$

Here, v is related to the stoichiometric factor and is equal to 2 for a monovalent salt. By combining equations 6.8 and 6.9, the thermodynamic factor can be determined with experimentally measurable quantities

$$\frac{\kappa(z^+v^+)}{vRTDc\left(\frac{1}{t_{+,id}}-1\right)}\left(\frac{dU}{dlnm}\right)^2 = 1 + \frac{dln\gamma_\pm}{dlnm}. \tag{6.10}$$

The sign of the open circuit potential depends on convention – some researchers report positive values for U, while others report negative values for U.[70,93,95,96] This depends on whether the positive or negative lead from the potentiostat is connected to the reference electrolyte. Eq. 6.10 is applicable regardless of convention or how the potentiostat is connected to the reference electrolyte. Once the thermodynamic factor is calculated, t_+^0 can be determined. Additionally, the above equation is true for all concentrations, as there are no assumptions about ideality within the calculation of t_+^0.

Electrolyte potential drop measurements

Lithium symmetric cells were prepared and electrochemically conditioned the same way as the ideal transference number measurement samples. Each sample was then polarized at all of the following current densities for 30 minutes: i_{ss} = 0.020, 0.040, and 0.10 mA/cm^2 with potential and current data recorded every five seconds. Ac impedance spectroscopy followed each polarization and the data were analyzed in the form of a Nyquist plot. The data were fit to an

equivalent electrical circuit and the interfacial impedance, R_i, was extracted, as described in a previous publication.[76] The interfacial impedance was used to correct for the potential drop, Φ, across an electrolyte, as described in Eq. 6.11 below

$$\Phi = \Phi_{measured} - R_i i_{ss} A \tag{6.11}$$

where $\Phi_{measured}$ is the steady-state potential across the lithium symmetric cell as measured by the potentiostat under a given steady-state current density, i_{ss}, and A is the active area of the electrode.

6.2.3 Steady-state Model

The relationship between i_{ss} and the electrochemical properties of an electrolyte, based on Newman's concentrated solution theory,[39] was derived in ref. [111]. This relationship changes slightly when the electrolyte is contained in a porous separator (we call this the electrolyte/separator composite), and is given by Eq. 6.12 and has been used to predict concentration profiles in other liquid electrolytes[131]

$$\int_{m(x=0)}^{m(x)} \frac{c(m)D_s(m)}{mt_-^0(m)}\,dm = \frac{i_{ss}l}{Fz_-v_-}\left(\frac{x}{L}\right) \tag{6.12}$$

where c is the concentration of the salt in the electrolytic phase in mol/cm^3, D_s is the salt diffusion coefficient measured by restricted diffusion on the electrolyte/separator composite, m is the molality, t_-^0 is the anion transference number relative to the velocity of the solvent ($t_-^0 = 1 - t_+^0$), z_- is the charge number on the anion, v_- is the number of anions the salt disassociates into, L is the thickness of the electrolyte/separator composite, x/L is the normalized thickness, and F is Faraday's constant (the transference number is unaffected by the presence of the separator). All of the ion transport properties depend on salt concentration, as indicated in Eq. 6.12. During an experiment, the average salt concentration of the electrolyte, m_{av}, is controlled. The molality profile predicted by Eq. 6.12 must be averaged from $x = 0$ to $x = L$ to ensure that the model predicted average concentration is equal to m_{av}.

The relationship between the electric potential within an electrolyte/separator composite to the measurable transport properties is given by

$$\Phi(x) = -Fz_-v_- \int_{m(x=L)}^{m(x=0)} \frac{c(m)D_s(m)}{mt_{+,id}(m)\kappa_s(m)t_-^0(m)}\,dm \tag{6.13}$$

where $t_{+,id}$ is the ideal transference number (unaffected by the presence of the separator) and κ_s is the conductivity of the electrolyte/separator composite. In this paper, equations 6.12 and 6.13 were solved numerically using MATLAB for the relevant parameters.

6.3 Results and Discussion

The ionic conductivity, κ, salt diffusion coefficient, D, and the ideal transference number, $t_{+,id}$ were determined through three independent experiments as described in the Experimental and Theoretical Details section. The three aforementioned transport parameters are shown in Fig. 6.3 as a function of average salt concentration, c_{av}, measured at room temperature. The open circuit potential is plotted as a function of ln(m_{av}) due to it's appearance as $\frac{dU}{d\ln m}$ in Eq. 6.10 to calculate the thermodynamic factor, T_f. The red upward triangles are data collected for mixtures of LiFSI and PC and the blue upside-down triangles represent data collected for binary mixtures of $LiPF_6$ and PC. The solid red curves are fits through the data for LiFSI and PC and the blue curves are fits through the data for $LiPF_6$ and PC. Parameters for the fitting functions for κ, D, and $t_{+,id}$ are listed in Table 6.3 for both binary mixtures.

Table 6.3 The best-fit polynomial equations for all transport properties in LiFSI + PC and $LiPF_6$ + PC electrolytes.

$$P\ (\text{LiX}) = k_0 + k_1 c + k_2 c^2 + k_3 c^3$$

P (LiX)	k_0	k_1	k_2	k_3
κ (LiFSI)	8.67 x 10^{-4}	1.30 x 10^{-2}	-9.28 x 10^{-3}	3.14 x 10^{-3}
D (LiFSI)	1.15 x 10^{-6}	-1.41 x 10^{-6}	1.37 x 10^{-6}	-4.42 x 10^{-7}
$t_{+,id}$ (LiFSI)	0.276	-0.567	0.426	-9.29 x 10^{-2}
κ ($LiPF_6$)	9.52 x 10^{-5}	1.63 x 10^{-2}	-1.36 x 10^{-2}	3.14 x 10^{-3}
D ($LiPF_6$)	1.18 x 10^{-6}	-2.05 x 10^{-6}	1.73 x 10^{-6}	-3.93 x 10^{-7}
$t_{+,id}$ ($LiPF_6$)	4.79 x 10^{-2}	-0.146	0.164	-4.57 x 10^{-2}

Fig. 4a plots conductivity as a function of c_{av} for both LiFSI and $LiPF_6$ based electrolytes. At low concentrations, the conductivities of LiFSI and $LiPF_6$ electrolytes are very similar. The behavior qualitatively changes at higher salt concentrations. The conductivity of LiFSI/PC goes through a maximum of 6.13 x 10^{-3} ± 8.50 x 10^{-6} S/cm at c_{av} = 1.00 M and that of $LiPF_6$/PC goes through a maximum of 5.96 x 10^{-3} ± 1.61 x 10^{-5} S/cm at c_{av} = 0.75 M. Between 0.75 M ≤ c_{av} ≤ 1.75 M, LiFSI has a higher conductivity than that of $LiPF_6$, whereas κ of $LiPF_6$ is greater than LiFSI between 1.75 M < c_{av} ≤ 2.00 M. The measured conductivity values are quantitatively and qualitatively similar to values published elsewhere.[139,145] The salt diffusion coefficient for LiFSI, shown in Fig. 6.3b, decreases with increasing salt concentration following the polynomial fit shown in Table 6.4. For $LiPF_6$, D is a non-monotonic function of increasing salt concentration, also shown in Fig. 6.3b. The salt diffusion coefficient for $LiPF_6$ goes through a shallow minimum around c_{av} = 0.75 M. The behavior of D as a function of salt concentration for $LiPF_6$ shown here is qualitatively different from other reported values. In work published by Nishida *et al.*, D is constant with salt concentration, while in Hou and Monroe, D decreases with increasing salt concentration.[139,146] The salt diffusion coefficient measured in this work for $LiPF_6$ is on the

same order of magnitude as measured in those two studies. The ideal transference number, $t_{+,id}$, is plotted as a function of c_{av} in Fig. 6.4c, and is a non-monotonic function of salt concentration for both LiFSI and $LiPF_6$. LiFSI exhibits a higher $t_{+,id}$ than $LiPF_6$ for all salt concentrations that were studied. Notably, $t_{+,id}$ ranges between 0.04 and 0.16 for LiFSI and between 0.01 and 0.05 for $LiPF_6$. This is considerably different from literature reported $t_{+,id}$ values for nonaqueous liquid electrolytes, where $t_{+,id}$ ranges between 0.20 and 0.40.[147–149] However, these reports use the initial current as measured by the potentiostat rather than the initial current calculated by Ohm's law (see Eq. 6.1) to calculate $t_{+,id}$. By using the initial current from the potentiostat in the calculation, $t_{+,id}$ is often greater than if Ohm's law is used for the initial current.[150] In addition, an unstable interfacial resistance over the course of the applied potential can cause an improper calculation of $t_{+,id}$. In Fig. 6.4, R_i is plotted as a function of c_{av} for both LiFSI and $LiPF_6$ before and after dc polarization. Interfacial resistance for LiFSI before and after dc polarization is shown in Fig. 6.4a, and R_i of $LiPF_6$ before and after polarization is shown in Fig. 6.4b. The interfacial resistance before and after polarization is approximately constant for both LiFSI and $LiPF_6$ electrolytes. Fig. 6.3d is the open circuit potential, measured using concentration cells, as a function of the natural log of molality for LiFSI and $LiPF_6$. The open circuit potential is zero when both sides of the *U*-cell contain the reference electrolyte ($m_{av,LiFSI}$ = 0.92 mol/kg, $m_{av,LiPF_6}$ = 0.87 mol/kg). A polynomial fit to the open circuit potential for LiFSI is shown as a red, solid curve and follows the equation:

$$U_{LiFSI}(m) = -7.294(\ln m)^3 - 27.87(\ln m)^2 - 80.48 \ln m - 6.010. \quad (6.14)$$

A polynomial fit to the open circuit potential for $LiPF_6$ is shown as a blue, solid curve and follows the equation:

$$U_{LiPF_6}(m) = -12.10(\ln m)^3 - 41.34(\ln m)^2 - 89.21 \ln m - 10.09. \quad (6.15)$$

The open circuit potentials for LiFSI and $LiPF_6$ are similar to one another when the measured molality is close to m_{ref}, but the two deviate from one another when the measured *m* is further from m_{ref}. The differences in potential may be due to a difference in solvation environments of LiFSI in PC and $LiPF_6$ in PC.[151–153]

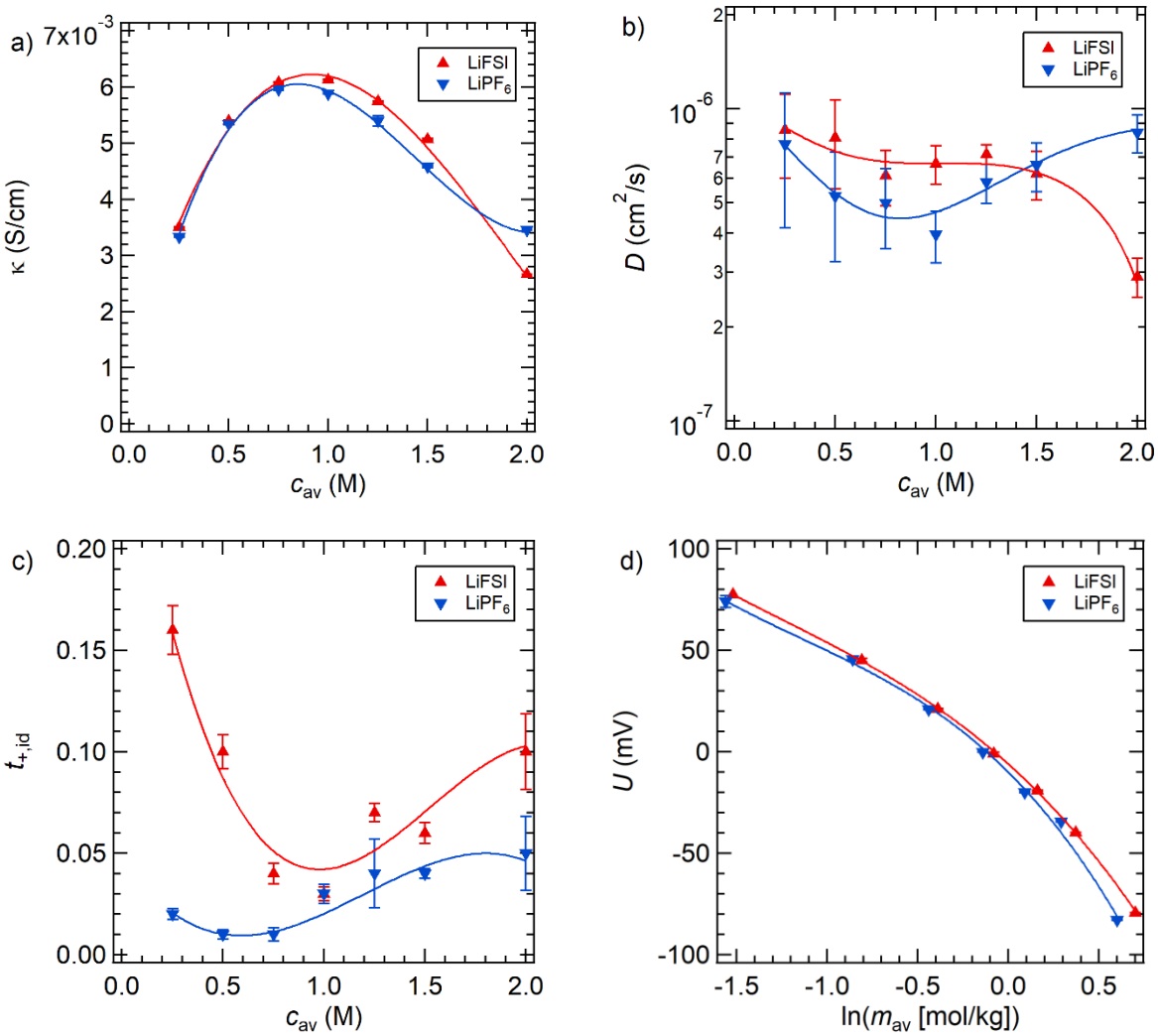

Figure 6.3 Electrochemical properties of the electrolytic phase of PC/LiFSI and PC/$LiPF_6$. The solid red curves are fits through the data for LiFSI/PC and the solid blue curves are fits through the data for $LiPF_6$/PC (Table 6.4). a) Conductivity as measured using a conductivity probe, b) salt diffusion coefficient measured using the restricted diffusion method, and c) ideal transference number as measured by the steady-state current method all as a function of average salt concentration, c_{av}. d) Open circuit potential obtained using concentration cells with reference $m_{av,LiFSI}$ = 0.92 mol/kg and $m_{av,LiPF_6}$ = 0.87 mol/kg as a function of the natural log of average molality. The solid, red curve is a fit through the LiFSI/PC data (Eq. 6.14) and the solid, blue curve is a fit through the $LiPF_6$/PC data (Eq. 6.15).

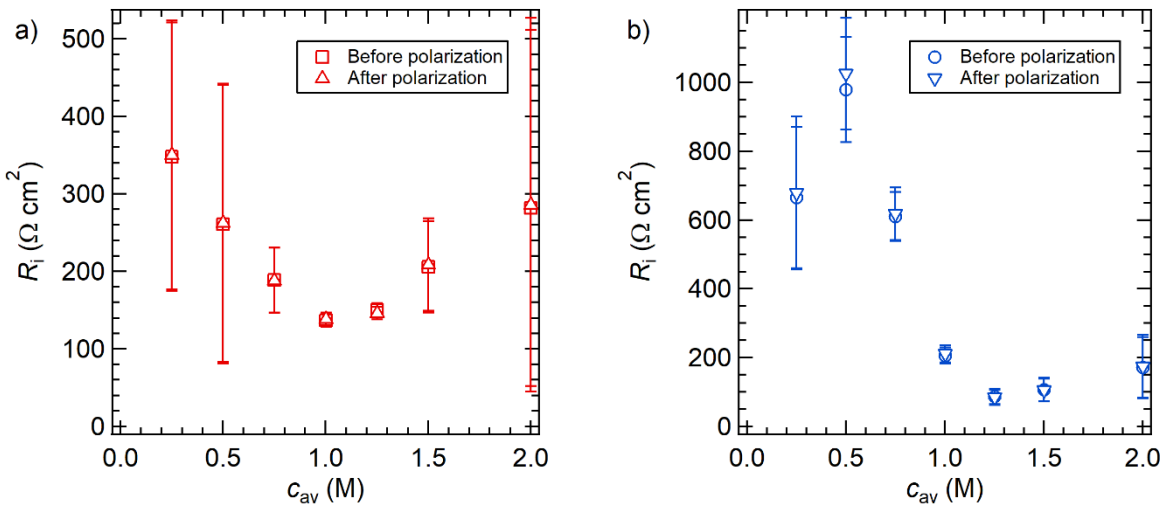

Figure 6.4 Resistance of the electrolyte/lithium interface before and after dc polarization during the steady-state current experiment for a) LiFSI/PC and b) $LiPF_6$/PC.

The thermodynamic factor, $1 + \frac{d \ln \gamma_{\pm}}{d \ln m}$, calculated using Eq. 6.10, the fits to the data shown in Fig. 6.3, and Table 6.4, is shown in Fig. 6.5 as a function of c_{av}. The thermodynamic factor for LiFSI/PC is a non-monotonic function of concentration, and goes through a shallow minimum at c_{av} = 1.00 M, after which T_f increases rapidly. As for $LiPF_6$/PC, T_f increases monotonically with increasing concentration. Using T_f, along with the data from Fig. 6.3, the cation transference number relative to the solvent velocity, t_+^0, is calculated and shown in Fig. 6.6. For mixtures of LiFSI/PC, t_+^0 begins positive as the lowest salt concentration, becomes negative at higher values, and rises back to 0.03 at c_{av} = 2.00 M. The trend in t_+^0 with increasing concentration for $LiPF_6$/PC is more complex, but is negative in the entire range that was studied. The measured values for $LiPF_6$/PC are highly negative, and may be due to errors that have propagated from the four independent measurements that are needed, as shown in Eq. 6.9. It would be valuable to obtain t_+^0 using electrophoretic NMR, which can directly measure t_+^0, and compare to the results obtained using the Balsara-Newman method.[154] Electrophoretic NMR has been applied to a few electrolytes to obtain t_+^0, but the values have not yet been used to predict electrolyte potential drop or limiting currents.[86,155–157]

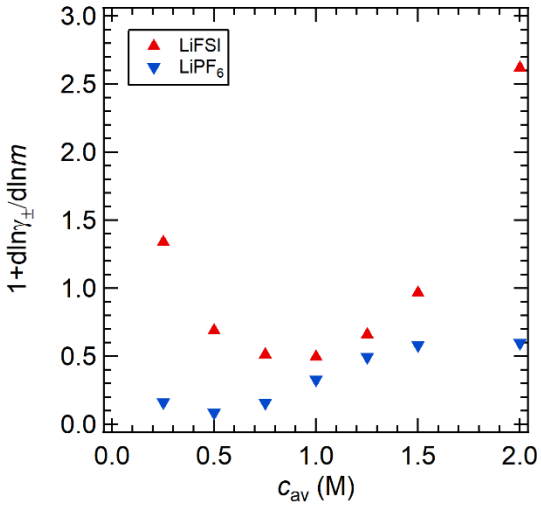

Figure 6.5 The thermodynamic factor as a function of salt concentration for LiFSI/PC and $LiPF_6$/PC.

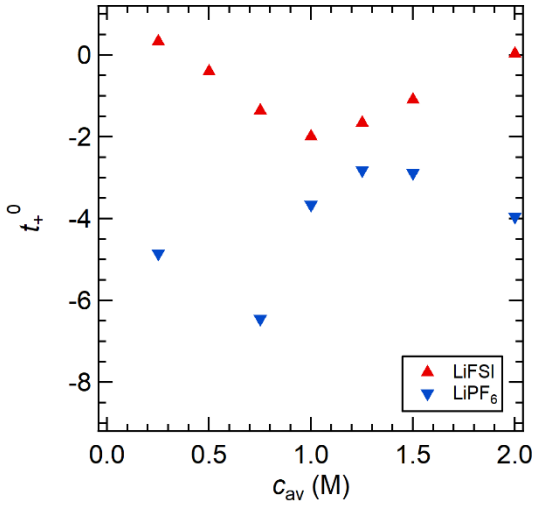

Figure 6.6 Transference number, t_+^0, based on concentrated solution theory for LiFSI/PC and $LiPF_6$/PC. The rest of the paper will focus on data for LiFSI/PC.

In the remaining chapter, we will focus on mixtures of LiFSI/PC. Using the electrochemical data for LiFSI/PC, we can predict the steady-state potential behavior of the electrolyte in Li symmetric cells and compare with experimental results as a function of normalized current density, $i_{ss}L$, and average salt concentration. To calculate the concentration profile within an electrolyte given an i_{ss} and L, the transport parameters on the left-hand-side of Eq. 6.12 were fit as a continuous function of salt concentration. Fig. 6.7a shows an exponential plus constant fit to the product on the left-hand-side of Eq. 6.12

$$\frac{c(m)D_s(m)}{mt_-^0(m)} = a_0 \exp(\Gamma m) + a_1 \tag{6.16}$$

with fitting parameters

$$a_0 = 4.700\text{x}10^{-9} \quad a_1 = 2.673\text{x}10^{-10} \quad \Gamma = -6.157$$

where c is in mol/cm^3, D_s is the salt diffusion coefficient of the separator/electrolyte composite, and $t_-^0 = 1 - t_+^0$. The steady-state concentration profiles must be obtained in order to ensure that the space averaged predicted concentration equals the starting average concentration of m_{av}. In Fig. 6.7b, we show a double exponential fit to the product on the left-hand-side of Eq. 6.13 in order to predict the electrolyte potential:

$$\frac{c(m)D_s(m)}{mt_{+,id}\kappa_s t_-^0(m)} = b_0 \exp(\tau_0 m) + b_1 \exp(\tau_1 m) \tag{6.17}$$

with fitting parameters

$$b_0 = 1.192\text{x}10^{-6} \quad b_1 = 9.016\text{x}10^{-7}$$
$$\tau_0 = -0.1700 \quad \tau_1 = -7.239$$

where κ_s is the conductivity of the separator/electrolyte composite.

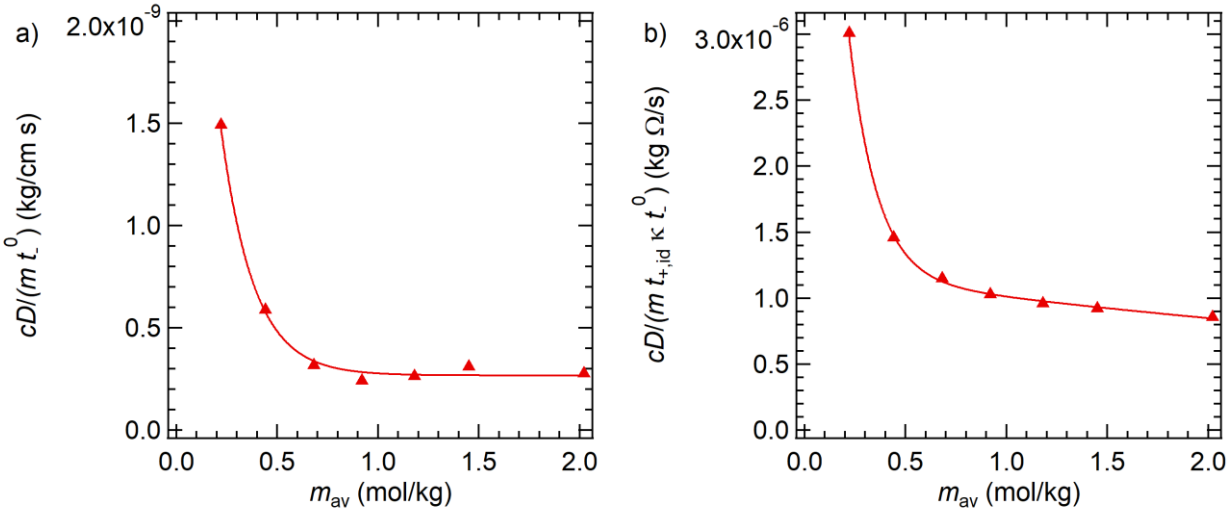

Figure 6.7 Fits of the integrand term of a) Eq. 6.12, $\frac{cD_s}{mt_-^0}$, given by Eq. 6.16 and b) Eq. 6.13, $\frac{cD_s}{mt_{+,id}\kappa_s t_-^0}$, given by Eq. 6.17.

Fig. 6.8a shows the model predicted concentration profiles for a normalized current density, $i_{ss}L$, of 0.0016 mA/cm for three average concentrations of c_{av} = 0.50, 1.00, and 1.50 M. At this normalized current density, the salt concentration gradients for all three concentrations are small and approximately linear. Fig. 6.8b is the predicted potential, ϕ, for the same normalized current density and concentration gradient. Interestingly, the predicted potential drop is the largest for the concentration with the greatest conductivity, c_{av} = 1.00 M.

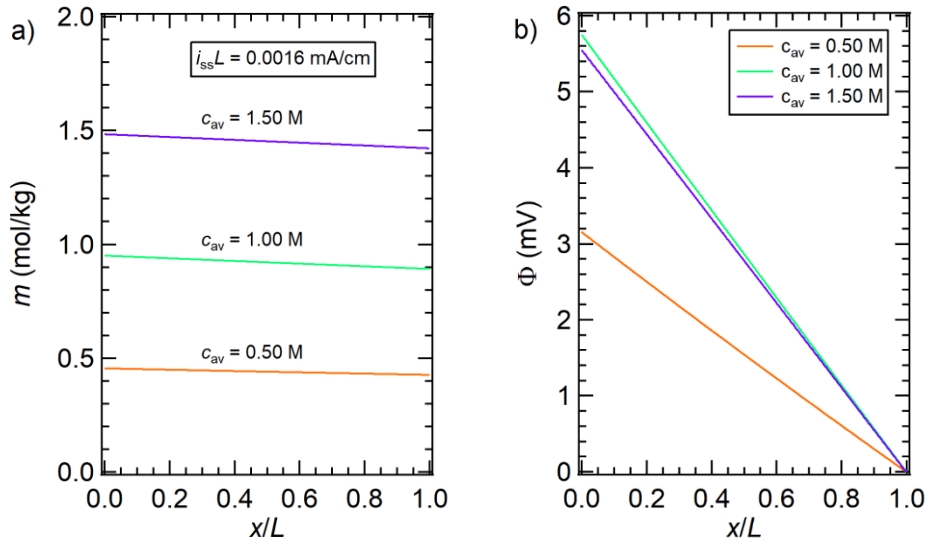

Figure 6.8 Model predicted a) salt concentration and b) potential profiles for mixtures of LiFSI/PC with c_{av} = 0.50, 1.00, and 1.50 M at $i_{ss}L$ = 0.0016 mA/cm.

The experimentally applied potential drop, Φ_{exp}/L, for the electrolyte with c_{av} = 1.00 M (see Table 6.1 to convert c_{av} to m_{av}) is plotted as a function of i_{ss} in Fig. 6.9a. The experimental potential drop is corrected for the lithium/electrolyte interfacial impedance using Eq. 6.11. Also shown in Fig. 6.9a is the predicted potential drop, Φ_0/L, calculated from Fig. 6.8 for c_{av} = 1.00M. Both theory and experiment indicate that Φ/L increases with increasing i_{ss}. For the range of i_{ss} studied, the model under predicts Φ_{exp}/L. The deviation between experiments and theory remains approximately constant with increasing current density. Further work is needed to resolve this discrepancy. In Fig. 6.9b, we plot Φ_{exp}/L against c_{av} for i_{ss} = 0.04 mA/cm^2 and find that Φ_{exp}/L is a strong function of c_{av}. Theoretical predictions, also shown in Fig. 6.9b, support this observation. Both the experimental and theoretical potential drops exhibit a maximum at c_{av} = 1.00 M, at the same concentration that κ is maximized. The model predicts that the lowest potential drop within the electrolyte would occur at c_{av} = 0.50 M, then increases until c_{av} = 1.00 M, followed by a shallow decline. Experimentally, the potential drop is observed to be lowest at c_{av} = 1.50 M, however the experimental error is also the largest at that concentration. While the theoretical predictions generally lie below the experimental data, they agree qualitatively with the experimental observations.

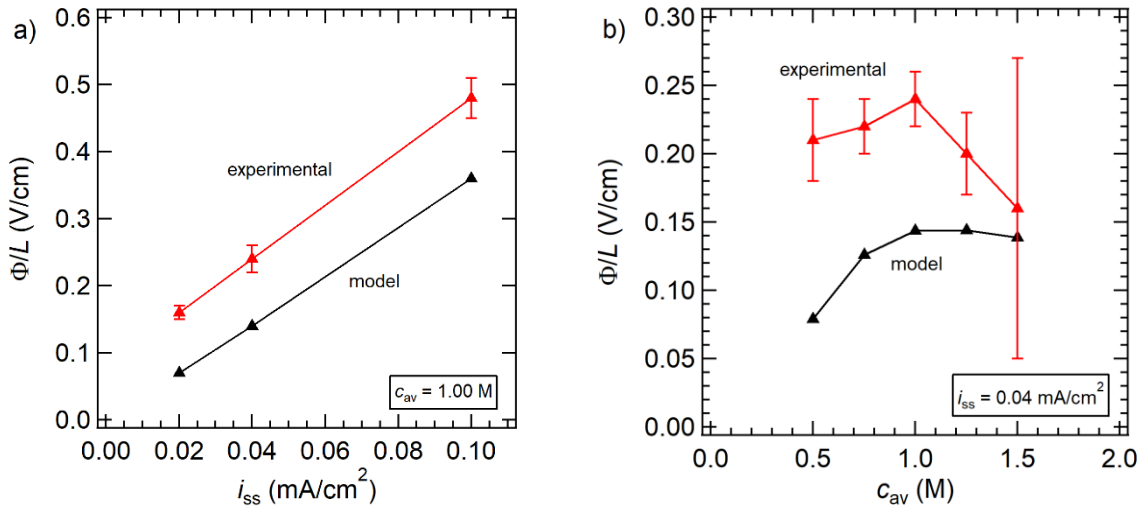

Figure 6.9 Experimental (red) and model predicted (black) potential as a function of a) i_{ss} for a concentration of c_{av} = 1.00 M and b) c_{av} for i_{ss} = 0.04 mA/cm^2.

6.4 Conclusion

In this work, a complete set of ion transport parameters, as a function of salt concentration, were measured for mixtures of LiFSI and PC and $LiPF_6$ and PC at room temperature. These parameters include conductivity, κ, salt diffusion coefficient, D, as measured by the restricted diffusion technique, ideal transference number, $t_{+,id}$, measured using the steady-state current method, and the thermodynamic factor, T_f, using concentration cells combined with the aforementioned transport properties. These four measurements were combined to calculate the cation transference number with reference to the velocity of the solvent, t_+^0, based in Newman's concentrated solution theory. The cation transference number for $LiPF_6$/PC was significantly more negative at all salt concentrations compared to that of LiFSI/PC. However, the calculation of t_+^0 is highly dependent on measurements of κ, D, $t_{+,id}$, and T_f. Further work is necessary to directly measure t_+^0, using methods such as electrophoretic NMR, in order to compare results with those presented in this work.

The dc potential across a lithium symmetric cell containing LiFSI/PC was measured experimentally as a function of applied current density and salt concentration. The results were compared to theoretical results based in Newman's concentrated solution theory. The predicted potential drop of the electrolyte within the Li symmetric cell was lower than the experimental behavior at all i_{ss} and c_{av}. The model predicted results qualitatively captured the experimental potential behavior. Both experiment and theory showed an increase in electrolyte potential drop between 0.50 and 1.00 M and a decrease from 1.00 to 1.5 M. There was a maximum in the electrolyte potential drop at 1.00 M, which is the same concentration that conductivity is maximized for mixtures of LiFSI and PC. In order to fully understand the ohmic drop of an electrolyte, ion transport properties beyond conductivity must be measured. Our approach enables comparing theory with experiment with no adjustable parameters.

6.5 Acknowledgements

This work was sponsored in part by Robert Bosch LLC through Bosch Energy Research Network Grant no. 12.1 0.BS.15.

6.6 Nomenclature

A	Active surface area of electrode (cm^2)
a, b	Fit parameters in Eq. 6.3
c	Concentration (mol/cm^3 or mol/L)
c_{av}	Average concentration (mol/cm^3 or mol/L)
D	Salt diffusion coefficient of electrolytic phase (cm^2/s)
D_s	Salt diffusion coefficient of electrolyte in separator (cm^2/s)
F	Faraday's constant (96,485 C/mol)
I_{ss}	Steady-state current (mA)
I_Ω	Initial current calculated using Ohm's law (mA)
i_{ss}	Steady-state current density (mA/cm^2)
k_0	Offset voltage (mV)
L	Thickness of electrolyte/separator (cm)
m_{av}	Average molality (mol/kg)
m	Molality (mol/kg)
R	Ideal gas constant (J/mol K)
R_i	Resistance of the electrolyte/electrode interface (Ω)
$R_{i,0}$	Resistance of electrolyte/electrode interface initially, prior to polarization (Ω)
$R_{i,ss}$	Resistance of solvent/electrode interface when Iss reached (Ω)
R_T	Total resistance of cell (R_s + $R_{i,0}$) (Ω)
T	Temperature (K)
T_f	Thermodynamic factor
t_+^0	Cation transference number relative to the solvent velocity. Obtained using the Balsara and Newman method
t_-^0	Anion transference number relative to the solvent velocity; $t_-^0 = 1 - t_+^0$
$t_{+,id}$	Ideal transference number using steady-state current method
x	Position (cm)
U	Open-circuit voltage (mV)
z^+	Cation charge
$1 + \frac{dln\gamma_\pm}{dlnm}$	Thermodynamic factor

Greek

α	Nondimensional time
$\gamma_\pm$	Mean molal activity coefficient of the salt
κ	Conductivity of the electrolytic phase (S/cm)
κ_s	Conductivity of the electrolyte and separator combined (S/cm)
v	Stoichiometric parameter = 2 for univalent salts ($= v^+ + v^-$)

v^i	Number of cations/anions per molecule of salt ($i = +$ or $-$)
ΔV	Dc polarization potential (mV)
ρ	Density (g/mL)
τ	Tortuosity of the separator
Φ	Electrolyte potential (mV)
$\Phi_{measured}$	Measured cell potential (mV)
ϕ_c	Volume fraction of conducting phase in separator

7 Conclusion

Liquid electrolytes are an integral component to current lithium-ion batteries. The development of next-generation lithium based batteries is predicated on understanding and improving upon the ion transport limitations of current-day electrolytes. In this work, we aim to understand the factors that govern ion transport in novel and conventional electrolytes by implementing concentrated solution theory for a variety of salt and solvent mixtures.

In chapter 2, we studied liquid perfluorether solvents which varied only in molecular weight, C6-DMC and C8-DMC. We produced binary electrolyte mixtures of LiFSI, LiTFSI, and LiBETI in C6-DMC and C8-DMC. The anions of the three salts were imide-based and varied in ion size only (FSI^- < $TFSI^-$ < $BETI^-$). The solubility limit of the three salts ranged between 25 – 35 wt% for all three salts in C8-DMC and C6-DMC, with the exception of LiTFSI in C6-DMC, which was soluble to 4.4 wt% in C6-DMC. The conductivity, κ, as measured by ac impedance spectroscopy, and ideal transference number, $t_{+,id}$, measured using the steady-state current method, were determined for a range of salt concentrations. The optimal mixture was determined by the product of κ and $t_{+,id}$, which acts as a modified Ohm's law for binary electrolytes.[150] The optimal electrolyte was found to be a mixture of C8-DMC with LiFSI.

In chapter 3, we characterized mixtures of C8-DMC and LiFSI using Newman's concentrated solution theory, and compared the experimental ion transport properties to those obtained using methods based in dilute solution theory. In addition to the conductivity and ideal transference number, the salt diffusion coefficient, as measured by restricted diffusion, and open circuit potential, determined using concentration cells, were reported. The combination of the four experiments allowed for the calculation of the cation transference number with respect to solvent velocity, t_+^0. The calculation of t_+^0, developed by Balsara and Newman, is based in concentrated solution theory and does not require assumptions on electrolyte ideality.[70] A third transference number was measured using pulsed field gradient NMR (PFG-NMR), $t_{+,NMR}$. If the electrolyte was ideal, the three transference numbers would be equivalent to one another. Instead, all three measured transference numbers were quantitatively and qualitatively different from one another. The rigorous transference number, t_+^0, was found to be negative at all salt concentrations, whereas $t_{+,id}$ was positive and decreased monotonically with increasing salt concentration. Over the same salt concentration, $t_{+,NMR}$ remained constant and positive. The difference in these measured transference numbers suggest that this perfluorinated solvent is highly non-ideal.

In chapter 4, the ion transport properties obtained in chapter 3 were utilized in a model to predict limiting current and potential behavior of LiFSI/C8-DMC electrolytes in lithium symmetric cells. Salt concentration profiles for a range of applied current densities and starting salt concentrations, m_{av}, were modeled using Newman's concentrated solution theory. The modeled salt concentration profiles were used to predict the maximum dc current draw the electrolyte could support, which is also known as the limiting current. The model considered Li^+ depletion at the electrolyte/cathode interface, as well as salt solubility limitations at the electrolyte/anode interface in order to predict the limiting current. Dilute solution theory was also used to predict the limiting current of these electrolytes. Both of these results were compared to experimental measurements of limiting current and it was found that the model predicted values based in concentrated solution theory was in quantitative and qualitative agreement with experiments,

whereas dilute solution theory largely over predicted the electrolyte's limiting current. In addition, concentrated solution theory was used to predict the electrolyte potential behavior, both transient and at steady-state. This was compared to experimental potential behavior and good agreement was found.

In chapter 5, a complete set of ion transport properties were reported for mixtures of tetraglyme and LiTFSI at two temperatures, 30 and 90 °C. We utilized the Newman concentrated solution theory framework in obtaining the complete set of ion transport properties. We found that κ and D are lower at 30 °C than at 90 °C at all salt concentrations. The ideal transference number, $t_{+,id}$, is greater at 30 °C than at 90 °C within the full experimental salt concentration window. At 30 °C, t_+^0 was calculated to be greater at concentrations below m_{av} = 4 mol/kg when compared to 90 °C. We used the full set of ion transport data obtained at 90 °C to compute salt concentration profiles as a function of current density and starting salt concentration. The predicted concentration gradients became increasingly nonlinear with increasing current density and m_{av}. This is likely due to a local minimum in t_+^0 at high m_{av} and a decreasing trend in D with increasing m_{av}. The modeled salt concentration profiles were used to predict the limiting current, and the results were compared to dilute solution theory predictions and experiments. Both dilute and concentrated solution theory failed to adequately capture the experimental limiting current results. It is important to note that the magnitude of the salt concentration difference between the anode side and m_{av} is much greater than the difference between the cathode side and m_{av} in the limit of high current densities. This suggests that the electrolyte may fail due to salt solubility limitations at the anode surface rather than lithium depletion on the cathode surface. Further work is necessary to measure the solubility limit of LiTFSi in tetraglyme and to predict the limiting current due to solubility limitations.

In chapter 6, we turn our attention to a conventional, carbonate electrolyte, propylene carbonate (PC). Here, we apply Newman's framework to elucidate ion transport properties of binary mixtures of LiFSI and PC and $LiPF_6$ and PC at room temperature. The necessary four parameters are measured: κ, $t_{+,id}$, D, and open circuit potential, U, using concentration cells for both mixtures. Conductivity, the salt diffusion coefficient, and U are similar for mixtures of both LiFSI/PC and $LiPF_6$/PC. However, $t_{+,id}$ is greater for LiFSI/PC than $LiPF_6$/PC at all salt concentrations. The measured properties were used to calculate t_+^0 for both sets of electrolytes and it was found that t_+^0 for $LiPF_6$/PC was much more negative than that of LiFSI/PC at all salt concentrations. The transport properties for LiFSI/PC were used to model the steady-state potential behavior for a range of salt concentrations and current densities. The predicted electrolyte potential drop was lower than that of the experimental values at all current densities and salt concentrations. However, the qualitative behavior was the same for both cases. Interestingly, at c_{av} = 1.00 M of LiFSI in PC, conductivity is maximized, but both the model and experimental behavior show a maximum in the electrolyte potential drop. Further work is necessary to ensure that the calculated values of t_+^0 in this chapter accurately represent the bulk electrolyte properties. Electrophoretic NMR may be one avenue to rigorously measure t_+^0 independently of the four parameters that were directly measured here. However, the qualitative agreement in both theory and experiment are further evidence that complete electrochemical characterization of conventional electrolytes is necessary in order to understand the underlying principles of ion transport, and thus predict cell behavior.

Liquid electrolytes are integral to today's lithium-ion batteries and will continue to be used for the foreseeable future. This work characterized the ion transport properties of both novel and conventional electrolytes and used those parameters to model lithium symmetric cell behavior under constant current conditions. We find that electrolytes, even in the dilute regime, should not be treated as ideal, and rather complete electrochemical characterization is necessary to adequately model electrolyte behavior.

References

(1) IPCC, 2014: *Climate Change 2014: Synthsis Report. Contribution of Working Groups I, II and III to the Fifth Assessment Report of the Intergovernmental Panel on Climate Change* [Core Writing Team, R. K. Pachauri, and L. A. Meyer (eds.)]. IPCC, Geneva, Switzerland, 151 pp.

(2) Environmental Protection Agency. *Inventory of U.S. Greenhouse Gas Emissions and Sinks: 1990-2005*; **2020**, Washington, D.C.

(3) Deloitte Center for Energy Solutions. *Supercharged: Challenges and Opportunities in Global Battery Storage Markets*. **2018**.

(4) Harlow, J. E.; Ma, X.; Li, J.; Logan, E.; Liu, Y.; Zhang, N.; Ma, L.; Glazier, S. L.; Cormier, M. M. E.; Genovese, M.; Buteau, S.; Cameron, A.; Stark, J. E.; Dahn, J. R. A Wide Range of Testing Results on an Excellent Lithium-Ion Cell Chemistry to be used as Benchmarks for New Battery Technologies. *J. Electrochem. Soc.* **2019**, *166* (13), A3031–A3044.

(5) United States Department of Energy. *Solving Challenges in Energy Storage*; **2019**, Washington, D.C.

(6) Xu, K. Electrolytes and Interphases in Li-Ion Batteries and Beyond. *Chem. Rev.* **2014**, *114* (23), 11503–11618.

(7) Xu, K. Nonaqueous Liquid Electrolytes for Lithium-Based Rechargeable Batteries. *Chem. Rev.* **2004**, *104* (10), 4303–4417.

(8) Goodenough, J. B.; Park, K. S. The Li-Ion Rechargeable Battery: A Perspective. *J. Am. Chem. Soc.* **2013**, *135* (4), 1167–1176.

(9) Janek, J.; Zeier, W. G. A Solid Future for Battery Development. *Nat. Energy* **2016**, *1* (9), 1–4.

(10) Balsara, N. P.; Newman, J. Comparing the Energy Content of Batteries, Fuels, and Materials. *J. Chem. Educ.* **2013**, *90* (4), 446–452.

(11) Volvo Car. *The State of Electric Vehicles in America*; 2019.

(12) Stewart, S. G.; Srinivasan, V.; Newman, J. Modeling the Performance of Lithium-Ion Batteries and Capacitors during Hybrid-Electric-Vehicle Operation. *J. Electrochem. Soc.* **2008**, *155* (9), A664–A671.

(13) Doyle, M.; Fuller, T. F.; Newman, J. The Importance of the Lithium Ion Transference Number in Lithium/Polymer Cells. *Electrochim. Acta* **1994**, *39* (13), 2073–2081.

(14) Srinivasan, V.; Newman, J. Discharge Model for the Lithium Iron-Phosphate Electrode. *J. Electrochem. Soc.* **2004**, *151* (10), A1517–A1529.

(15) Diederichsen, K. M.; McShane, E. J.; McCloskey, B. D. Promising Routes to a High Li^+ Transference Number Electrolyte for Lithium Ion Batteries. *ACS Energy Lett.* **2017**, *2* (11), 2563–2575.

(16) Clé, R. J.; Lun, Z.; Ceder, G. Cation-Disordered Rocksalt Transition Metal Oxides and Oxyfluorides for High Energy Lithium-Ion Cathodes. *Energy Environ. Sci* **2020**, *13* (2), 345–373.

(17) Liu, D.; Zhu, W.; Trottier, J.; Gagnon, C.; Barray, F.; Guerfi, A.; Mauger, A.; Groult, H.; Julien, C. M.; Goodenough, J. B.; Zaghib, K. Spinel Materials for High-Voltage Cathodes in Li-Ion Batteries. *RSC Adv.* **2014**, *4* (1), 154–167.

(18) Okada, S.; Sawa, S.; Egashira, M.; Yamaki, J. I.; Tabuchi, M.; Kageyama, H.; Konishi, T.; Yoshino, A. Cathode Properties of Phospho-Olivine $LiMPO_4$ for Lithium Secondary Batteries. *J. Power Sources* **2001**, *97–98*, 430–432.
(19) Ruffo, R.; Huggins, R. A.; Mari, C. M.; Piana, M.; Weppner, W. Phosphate Materials for Cathodes in Lithium Ion Secondary Batteries. **2005**, *11* (3-4), 213–219.
(20) Pesko, D. M.; Jung, Y.; Hasan, A. L.; Webb, M. A.; Coates, G. W.; Miller, T. F.; Balsara, N. P. Effect of Monomer Structure on Ionic Conductivity in a Systematic Set of Polyester Electrolytes. *Solid State Ion.* **2016**, *289*, 118–124.
(21) Zheng, Q.; Pesko, D. M.; Savoie, B. M.; Timachova, K.; Hasan, A. L.; Smith, M. C.; Miller, T. F.; Coates, G. W.; Balsara, N. P. Optimizing Ion Transport in Polyether-Based Electrolytes for Lithium Batteries. *Macromolecules* **2018**, *51* (8), 2847–2858.
(22) Choi, N. S.; Han, J. G.; Ha, S. Y.; Park, I.; Back, C. K. Recent Advances in the Electrolytes for Interfacial Stability of High-Voltage Cathodes in Lithium-Ion Batteries. *RSC Adv.* **2015**, *5* (4), 2732–2748.
(23) *X-CEL: EXtreme Fast Charge Cell Evaluation of Lithium-Ion Batteries*; 2019.
(24) Zhao, Q.; Zhang, Y.; Sun, G.; Cong, L.; Sun, L.; Xie, H.; Liu, J. Binary Mixtures of Highly Concentrated Tetraglyme and Hydrofluoroether as a Stable and Nonflammable Electrolyte for Li−O 2 Batteries. *ACS Appl. Matter. Interfaces* **2018**, *10* (31), 26312–26319.
(25) Amanchukwu, C.; Yu, Z.; Kong, X.; Qin, J.; Cui, Y.; Bao, Z.; Amanchukwu, C. V. A New Class of Ionically Conducting Fluorinated Ether Electrolytes with High Electrochemical Stability. *J. Am. Chem. Soc.* **2020**, *142* (16), 7393–7403.
(26) Fan, X.; Chen, L.; Borodin, O.; Ji, X.; Chen, J.; Hou, S.; Deng, T.; Zheng, J.; Yang, C.; Liou, S. C.; Amine, K.; Xu, K.; Wang, C. Non-Flammable Electrolyte Enables Li-Metal Batteries with Aggressive Cathode Chemistries. *Nat. Nanotechnol.* **2018**, *13* (8), 715–722.
(27) Azimi, N.; Xue, Z.; Rago, N. D.; Takoudis, C.; Gordin, M. L.; Song, J.; Wang, D.; Zhang, Z. Fluorinated Electrolytes for Li-S Battery: Suppressing the Self-Discharge with an Electrolyte Containing Fluoroether Solvent. *J. Electrochem. Soc.* **2015**, *162* (1), 64–68.
(28) Zu, C.; Azimi, N.; Zhang, Z.; Manthiram, A. Insight into Lithium-Metal Anodes in Lithium-Sulfur Batteries with a Fluorinated Ether Electrolyte. *J. Mater. Chem. A* **2015**, *3* (28), 14864–14870.
(29) Zheng, J.; Ji, G.; Fan, X.; Chen, J.; Li, Q.; Wang, H.; Yang, Y.; DeMella, K. C.; Raghavan, S. R.; Wang, C. High-Fluorinated Electrolytes for Li–S Batteries. *Adv. Energy Mater.* **2019**, *9* (16), 1–9.
(30) Achiha, T.; Nakajima, T.; Ohzawa, Y.; Koh, M.; Yamauchi, A.; Kagawa, M.; Aoyama, H. Thermal Stability and Electrochemical Properties of Fluorine Compounds as Nonflammable Solvents for Lithium-Ion Batteries. *J. Electrochem. Soc.* **2010**, *157* (6), A707–A712.
(31) Wong, D. H. C.; Thelen, J. L.; Fu, Y.; Devaux, D.; Pandya, A. A.; Battaglia, V. S.; Balsara, N. P.; DeSimone, J. M. Nonflammable Perfluoropolyether-Based Electrolytes for Lithium Batteries. *Proc. Natl. Acad. Sci.* **2014**, *111* (9), 3327–3331.
(32) Feng, Y.; Chen, X.; Wei, H.; Pei, Y.; Tang, X. Chloroethoxy-Terminated Perfluoropolyether Electrolytes with High Lithium Ion Transference Number for Lithium Battery Applications. *Polymer* **2019**, *178*, 121596.

(33) Shi, P.; Fang, S.; Huang, J.; Luo, D.; Yang, L.; Hirano, S. A Novel Mixture of Lithium Bis(oxalato)borate, Gamma-Butyrolactone and Non-Flammable Hydrofluoroether as a Safe Electrolyte for Advanced Lithium Ion Batteries. *J. Mater. Chem. A* **2017**, *5* (37), 19982–19990.
(34) Suo, L.; Borodin, O.; Gao, T.; Olguin, M.; Ho, J.; Fan, X.; Luo, C.; Wang, C.; Xu, K. "Water-in-Salt" Electrolyte Enables High-Voltage Aqueous Lithium-Ion Chemistries. *Science* **2015**, *350* (6263), 938–943.
(35) Yang, C.; Chen, J.; Qing, T.; Fan, X.; Sun, W.; von Cresce, A.; Ding, M. S.; Borodin, O.; Vatamanu, J.; Schroeder, M. A.; Eidson, N.; Wang, C.; Xu, K. 4.0 V Aqueous Li-Ion Batteries. *Joule* **2017**, *1* (1), 122–132.
(36) Wang, J.; Yamada, Y.; Sodeyama, K.; Chiang, C. H.; Tateyama, Y.; Yamada, A. Superconcentrated Electrolytes for a High-Voltage Lithium-Ion Battery. *Nat. Commun.* **2016**, *7* (1), 12032.
(37) Yamada, Y.; Wang, J.; Ko, S.; Watanabe, E.; Yamada, A. Advances and Issues in Developing Salt-Concentrated Battery Electrolytes. *Nat. Energy* **2019**, *4*, 269–280.
(38) Onsager, L. Theories and Problems of Liquid Diffusion. *Ann. N. Y. Acad. Sci.* **1945**, *46* (5), 241–265.
(39) Newman, J.; Thomas-Alyea, K. E. *Electrochemical Systems*, third; John Wiley & Sons, Inc., Hoboken, New Jersey, **2004**.
(40) Goodenough, J. B.; Kim, Y. Challenges for Rechargeable Li Batteries. *Chem. Mater.* **2010**, *22* (3), 587–603.
(41) Aurbach, D.; Zinigrad, E.; Cohen, Y.; Teller, H. A Short Review of Failure Mechanisms of Lithium Metal and Lithiated Graphite Anodes in Liquid Electrolyte Solutions. *Solid State Ion.* **2002**, *148* (3–4), 405–416.
(42) Eshkenazi, V.; Peled, E.; Burstein, L.; Golodnitsky, D. XPS Analysis of the SEI Formed on Carbonaceous Materials. *Solid State Ion.* **2004**, *170* (1–2), 83–91.
(43) Kraytsberg, A.; Ein-Eli, Y.; Kraytsberg, A.; Ein-Eli, Y. Higher, Stronger, Better ... A Review of 5 Volt Cathode Materials for Advanced Lithium-Ion Batteries. *Adv. Energy Mater.* **2012**, *2* (8), 922–939.
(44) Yang, L.; Ravdel, B.; Lucht, B. L. Electrolyte Reactions with the Surface of High Voltage $LiNi_{0.5}Mn_{1.5}O_4$ Cathodes for Lithium-Ion Batteries. *Electrochem. Solid-State Lett.* **2010**, *13* (8), A95–A97.
(45) Zhang, Z.; Hu, L.; Wu, H.; Weng, W.; Koh, M.; Redfern, P. C.; Curtiss, L. A.; Amine, K. Fluorinated Electrolytes for 5 V Lithium-Ion Battery Chemistry. *Energy Environ. Sci.* **2013**, *6* (6), 1806–1810.
(46) Chintapalli, M.; Timachova, K.; Olson, K. R.; Mecham, S. J.; Devaux, D.; Desimone, J. M.; Balsara, N. P. Relationship between Conductivity, Ion Diffusion, and Transference Number in Perfluoropolyether Electrolytes. *Macromolecules* **2016**, *49* (9), 3508–3515.
(47) Wong, D. H. C.; Vitale, A.; Devaux, D.; Taylor, A.; Pandya, A. A.; Hallinan, D. T.; Thelen, J. L.; Mecham, S. J.; Lux, S. F.; Lapides, A. M.; Resnick, P. R.; Meyer, T. J.; Kostecki, R. M.; Balsara, N. P.; DeSimone, J. M. Phase Behavior and Electrochemical Characterization of Blends of Perfluoropolyether, Poly(Ethylene Glycol), and a Lithium Salt. *Chem. Mater.* **2015**, *27* (2), 597–603.
(48) Timachova, K.; Chintapalli, M.; Olson, K. R.; Mecham, S. J.; DeSimone, J. M.; Balsara, N. P. Mechanism of Ion Transport in Perfluoropolyether Electrolytes with a Lithium Salt. *Soft Matter* **2017**, *13* (32), 5389–5396.

(49) Olson, K. R.; Wong, D. H. C.; Chintapalli, M.; Timachova, K.; Janusziewicz, R.; Daniel, W. F. M.; Mecham, S.; Sheiko, S.; Balsara, N. P.; DeSimone, J. M. Liquid Perfluoropolyether Electrolytes with Enhanced Ionic Conductivity for Lithium Battery Applications. *Polymer* **2016**, *100*, 126–133.
(50) Berger, R.; Resnati, G.; Metrangolo, P.; Weber, E.; Hulliger, J. Organic Fluorine Compounds: A Great Opportunity for Enhanced Materials Properties. *Chem. Soc. Rev.* **2011**, *40* (7), 3496–3508.
(51) Cznotka, E.; Jeschke, S.; Grünebaum, M.; Wiemhöfer, H.-D. Highly-Fluorous Pyrazolide-Based Lithium Salt in PVDF-HFP as Solid Polymer Electrolyte. *Solid State Ion.* **2016**, *292*, 45–51.
(52) Watanabe, M.; Nagano, S.; Sanui, K.; Ogata, N. Estimation of Li^+ Transport Number in Polymer Electrolytes by the Combination of Complex Impedance and Potentiostatic Polarization Measurements. *Solid State Ion.* **1988**, *30*, 911–917.
(53) Bruce, P. G.; Vincent, C. A. Steady State Current Flow in Solid Binary Electrolyte Cells. *J. Electroanal. Chem.* **1987**, *225* (1–2), 1–17.
(54) Evans, J.; Vincent, C. A.; Bruce, P. G. Electrochemical Measurement of Transference Numbers in Polymer Electrolytes. *Polymer* **1987**, *28* (13), 2324–2328.
(55) Lascaud, S.; Perrier, M.; Vallee, a; Besner, S.; Prudhomme, J.; Armand, M. Phase-Diagrams and Conductivity Behavior of Poly(Ethylene Oxide) Molten-Salt Rubbery Electrolytes. *Macromolecules* **1994**, *27* (25), 7469–7477.
(56) Gorecki, W.; Jeannin, M.; Belorizky, E.; Roux, C.; Armand, M. Physical Properties of Solid Polymer Electrolyte PEO(LiTFSI) Complexes. *J. Phys. Condens. Matter* **1995**, *7* (34), 6823–6832.
(57) Vallee, A.; Besner, S.; Prud'Homme, J. Comparative Study of Poly(Ethylene Oxide) Electrolytes Made with $LiN(CF_3SO_2)_2$, $LiCF_3SO_3$ and $LiClO_4$: Thermal Properties and Conductivity Behaviour. *Electrochim. Acta* **1992**, *37* (9), 1579–1583.
(58) Pożyczka, K.; Marzantowicz, M.; Dygas, J. R.; Krok, F. Ionic Conductivity and Lithium Transference Number of Poly(Ethylene Oxide):LiTFSI System. *Electrochim. Acta* **2017**, *227*, 127–135.
(59) O'Hagan, D. Understanding Organofluorine Chemistry. An Introduction to the C-F Bond. *Chem. Soc. Rev.* **2008**, *37* (2), 308–319.
(60) Teran, A. A.; Tang, M. H.; Mullin, S. A.; Balsara, N. P. Effect of Molecular Weight on Conductivity of Polymer Electrolytes. *Solid State Ionics* **2011**, *203* (1), 18–21.
(61) Zhou, J.; Fedkiw, P. S. Ionic Conductivity of Composite Electrolytes Based on Oligo(Ethylene Oxide) and Fumed Oxides. *Solid State Ion.* **2004**, *166* (3–4), 275–293.
(62) Peled, E. The Electrochemical Behavior of Alkali and Alkaline Earth Metals in Nonaqueous Battery Systems—The Solid Electrolyte Interphase Model. *J. Electrochem. Soc.* **1979**, *126* (12), 2047–2051.
(63) Verma, P.; Maire, P.; Novák, P. A Review of the Features and Analyses of the Solid Electrolyte Interphase in Li-Ion Batteries. *Electrochim. Acta* **2010**, *55* (22), 6332–6341.
(64) Appetecchi, G. B.; Passerini, S. Poly(Ethylene Oxide)-$LiN(SO_2CF_2CF_3)_2$ Polymer Electrolytes II. Characterization of the Interface with Lithium. *J. Electrochem. Soc.* **2002**, *149* (7), A891–A897.
(65) Zhang, H.; Liu, C.; Zheng, L.; Xu, F.; Feng, W.; Li, H.; Huang, X.; Armand, M.; Nie, J.; Zhou, Z. Lithium Bis(Fluorosulfonyl)Imide/Poly(Ethylene Oxide) Polymer Electrolyte. *Electrochim. Acta* **2014**, *133*, 529–538.

(66) Xu, C.; Sun, B.; Gustafsson, T.; Edström, K.; Brandell, D.; Hahlin, M. Interface Layer Formation in Solid Polymer Electrolyte Lithium Batteries: An XPS Study. *J. Mater. Chem. A* **2014**, *2* (20), 7256–7264.
(67) Doyle, M.; Newman, J. Analysis of Transference Number Measurements Based on the Potentiostatic Polarization of Solid Polymer Electrolytes. *J. Electrochem. Soc.* **1995**, *142* (10), 3465–3468.
(68) Devaux, D.; Bouchet, R.; Glé, D.; Denoyel, R. Mechanism of Ion Transport in PEO/LiTFSI Complexes: Effect of Temperature, Molecular Weight and End Groups. *Solid State Ion.* **2012**, *227*, 119–127.
(69) Maitra, A.; Heuer, A. Cation Transport in Polymer Electrolytes: A Microscopic Approach. *Phys. Rev. Lett.* **2007**, *98* (22), 227802.
(70) Balsara, N. P.; Newman, J. Relationship between Steady-State Current in Symmetric Cells and Transference Number of Electrolytes Comprising Univalent and Multivalent Ions. *J. Electrochem. Soc.* **2015**, *162* (14), A2720–A2722.
(71) Aurbach, D.; Markovsky, B.; Shechter, A.; Ein-Eli, Y.; Cohen, H. A Comparative Study of Synthetic Graphite and Li Electrodes in Electrolyte Solutions Based on Ethylene Carbonate-Dimethyl Carbonate Mixtures. *J. Electrochem. Soc.* **1996**, *143* (12), 3809–3820.
(72) Fong, R.; Sacken, U. von; Dahn, J. R. Studies of Lithium Intercalation into Carbons Using Nonaqueous Electrochemical Cells. *J. Electrochem. Soc.* **1990**, *137* (7), 2009–2013.
(73) Guyomard, D.; Tarascon, J. M. Rechargeable $Li_{1+x}Mn_2O_4$/Carbon Cells with a New Electrolyte Composition: Potentiostatic Studies and Application to Practical Cells. *J. Electrochem. Soc.* **1993**, *140* (11), 3071–3081.
(74) Tarascon, J. M.; Guyomard, D. New Electrolyte Compositions Stable over the 0 to 5 V Voltage Range and Compatible with the $Li_{1+x}Mn_2O_4$/Carbon Li-Ion Cells. *Solid State Ion.* **1994**, *69* (3–4), 293–305.
(75) Baik, J. H.; Kim, D. G.; Lee, J. H.; Kim, S.; Hong, D. G.; Lee, J. C. Nonflammable and Thermally Stable Gel Polymer Electrolytes Based on Crosslinked Perfluoropolyether (PFPE) Network for Lithium Battery Applications. *J. Ind. Eng. Chem.* **2018**, *64*, 453–460.
(76) Shah, D. B.; Olson, K. R.; Karny, A.; Mecham, S. J.; DeSimone, J. M.; Balsara, N. P. Effect of Anion Size on Conductivity and Transference Number of Perfluoroether Electrolytes with Lithium Salts. *J. Electrochem. Soc.* **2017**, *164* (14), A3511–A3517.
(77) Markevich, E.; Salitra, G.; Rosenman, A.; Talyosef, Y.; Chesneau, F.; Aurbach, D. Fluoroethylene Carbonate as an Important Component in Organic Carbonate Electrolyte Solutions for Lithium Sulfur Batteries. *Electrochem. Commun.* **2015**, *60*, 42–46.
(78) McMillan, R.; Slegr, H.; Shu, Z. X.; Wang, W. Fluoroethylene Carbonate Electrolyte and Its Use in Lithium Ion Batteries with Graphite Anodes. *J. Power Sources* **1999**, *81-82*, 20–26.
(79) Lin, Y. M.; Klavetter, K. C.; Abel, P. R.; Davy, N. C.; Snider, J. L.; Heller, A.; Mullins, C. B. High Performance Silicon Nanoparticle Anode in Fluoroethylene Carbonate-Based Electrolyte for Li-Ion Batteries. *Chem. Commun.* **2012**, *48* (58), 7268–7270.
(80) Ma, Y.; Doyle, M.; Fuller, T. F.; Doeff, M. M.; De Jonghe, L. C.; Newman, J. The Measurement of a Complete Set of Transport Properties for a Concentrated Solid Polymer Electrolyte Solution. *J. Electrochem. Soc.* **1995**, *142* (6), 1859–1868.

(81) Gladysz, J. A.; Curran, D. P.; Horvath, I. T. *Handbook of Fluorous Chemistry*; Wiley Online Library, Weinheim, Germany, **2004**.
(82) Villaluenga, I.; Wujcik, K. H.; Tong, W.; Devaux, D.; Wong, D. H. C.; DeSimone, J. M.; Balsara, N. P. Compliant Glass-Polymer Hybrid Single Ion-Conducting Electrolytes for Lithium Batteries. *Proc. Natl. Acad. Sci.* **2016**, *113* (1), 52–57.
(83) Valøen, L. O.; Reimers, J. N. Transport Properties of $LiPF_6$-Based Li-Ion Battery Electrolytes. *J. Electrochem. Soc.* **2005**, *152* (5), A882-A891.
(84) Nyman, A.; Behm, M.; Lindbergh, G. Electrochemical Characterisation and Modelling of the Mass Transport Phenomena in $LiPF_6$-EC-EMC Electrolyte. *Electrochim. Acta* **2008**, *53* (22), 6356–6365.
(85) Noda, A.; Hayamizu, K.; Watanabe, M. Pulsed-Gradient Spin-Echo ^{1}H and ^{19}F NMR Ionic Diffusion Coefficient, Viscosity, and Ionic Conductivity of Non-Chloroaluminate Room-Temperature Ionic Liquids. *J. Phys. Chem. B* **2001**, *105* (20), 4603–4610.
(86) Gouverneur, M.; Schmidt, F.; Schönhoff, M. Negative Effective Li Transference Numbers in Li Salt/Ionic Liquid Mixtures: Does Li Drift in the "Wrong" Direction? *Phys. Chem. Chem. Phys.* **2018**, *20* (11), 7470–7478.
(87) Buss, H. G.; Chan, S. Y.; Lynd, N. A.; McCloskey, B. D. Nonaqueous Polyelectrolyte Solutions as Liquid Electrolytes with High Lithium Ion Transference Number and Conductivity. *ACS Energy Lett.* **2017**, *2* (2), 481–487.
(88) Joost, M.; Kunze, M.; Jeong, S.; Schönhoff, M.; Winter, M.; Passerini, S. Ionic Mobility in Ternary Polymer Electrolytes for Lithium-Ion Batteries. *Electrochim. Acta* **2012**, *86*, 330–338.
(89) Landesfeind, J.; Hattendorff, J.; Ehrl, A.; Wall, W. A.; Gasteiger, H. A. Tortuosity Determination of Battery Electrodes and Separators by Impedance Spectroscopy. *J. Electrochem. Soc.* **2016**, *163* (7), A1373–A1387.
(90) Devaux, D.; Chang, Y. H.; Villaluenga, I.; Chen, X. C.; Chintapalli, M.; Desimone, J. M.; Balsara, N. P. Conductivity of Carbonate- and Perfluoropolyether-Based Electrolytes in Porous Separators. *J. Power Sources* **2016**, *323*, 158–165.
(91) Pesko, D. M.; Webb, M. A.; Jung, Y.; Zheng, Q.; Miller, T. F.; Coates, G. W.; Balsara, N. P. Universal Relationship between Conductivity and Solvation-Site Connectivity in Ether-Based Polymer Electrolytes. *Macromolecules* **2016**, *49* (14), 5244–5255.
(92) Thompson, S.; Newman, J. Differential Diffusion Coefficients of Sodium Polysulfide Melts. *J. Electrochem. Soc.* **1989**, *136* (11), 3362–3369.
(93) Ehrl, A.; Landesfeind, J.; Wall, W. A.; Gasteiger, H. A. Determination of Transport Parameters in Liquid Binary Lithium Ion Battery Electrolytes. *J. Electrochem. Soc.* **2017**, *164* (4), A826–A836.
(94) Villaluenga, I.; Pesko, D. M.; Timachova, K.; Feng, Z.; Newman, J.; Srinivasan, V.; Balsara, N. P. Negative Stefan-Maxwell Diffusion Coefficients and Complete Electrochemical Transport Characterization of Homopolymer and Block Copolymer Electrolytes. *J. Electrochem. Soc.* **2018**, *165* (11), A2766–A2773.
(95) Pesko, D. M.; Timachova, K.; Bhattacharya, R.; Smith, M. C.; Villaluenga, I.; Newman, J.; Balsara, N. P. Negative Transference Numbers in Poly(Ethylene Oxide)-Based Electrolytes. *J. Electrochem. Soc.* **2017**, *164* (11), E3569–E3575.
(96) Ehrl, A.; Landesfeind, J.; Wall, W. A.; Gasteiger, H. A. Determination of Transport Parameters in Liquid Binary Electrolytes: Part II. Transference Number. *J. Electrochem. Soc.* **2017**, *164* (12), A2716–A2731.

(97) Alexej, J.; Norbert, M. Suppression of Convection Artifacts in Stimulated-Echo Diffusion Experiemnts. Double-Stimulated-Echo Experiments. *J. Magn. Reson.* **1997**, *375* (125), 372–375.
(98) Diederichsen, K. M.; Fong, K. D.; Terrell, R. C.; Persson, K. A.; McCloskey, B. D. Investigation of Solvent Type and Salt Addition in High Transference Number Nonaqueous Polyelectrolyte Solutions for Lithium Ion Batteries. *Macromolecules* **2018**, *51* (21), 8761–8771.
(99) Sinnaeve, D. The Stejskal-Tanner Equation Generalized for Any Gradient Shape - An Overview of Most Pulse Sequences Measuring Free Diffusion. *Concepts Magn. Reson. Part A* **2012**, *40A* (2), 39–65.
(100) Vanag, V. K.; Epstein, I. R. Cross-Diffusion and Pattern Formation in Reaction-Diffusion Systems. *Phys. Chem. Chem. Phys.* **2009**, *11* (6), 897–912.
(101) Barthel, J.; Krienke, H.; Kunz, W. *Physical Chemistry of Electrolyte Solutions –Modern Aspects*; Springer, Steinkopff, Darmstadt, **1998**.
(102) Hartley, G. S. Theory of the Velocity of Diffusion of Strong Electrolytes in Dilute Solution. *London, Edinburgh, Dublin Philos. Mag. J. Sci.* **1931**, *12* (77), 473–488.
(103) Dey, A. N.; Sullivan, B. P. The Electrochemical Decomposition of Propylene Carbonate on Graphite. *J. Electrochem. Soc.* **1970**, *117* (2), 222–224.
(104) Hong, J.; Maleki, H.; Al Hallaj, S.; Redey, L.; Selman, J. R. Electrochemical-Calorimetric Studies of Lithium-Ion Cells. *J. Electrochem. Soc.* **1998**, *145* (5), 1489–1501.
(105) Achiha, T.; Nakajima, T.; Ohzawa, Y.; Koh, M.; Yamauchi, A.; Kagawa, M.; Aoyama, H. Electrochemical Behavior of Nonflammable Organo-Fluorine Compounds for Lithium Ion Batteries. *J. Electrochem. Soc.* **2009**, *156* (6), A483-A488.
(106) Wang, C.; Tang, S.; Zuo, X.; Xiao, X.; Liu, J.; Nan, J. 3-(1,1,2,2-Tetrafluoroethoxy)-1,1,2,2-Tetrafluoropropane as a High Voltage Solvent for $LiNi_{1/3}Co_{1/3}Mn_{1/3}O_2$/Graphite Cells. *J. Electrochem. Soc.* **2015**, *162* (10), A1997–A2003.
(107) Park, J. W.; Yoshida, K.; Tachikawa, N.; Dokko, K.; Watanabe, M. Limiting Current Density in Bis(Trifluoromethylsulfonyl)Amide-Based Ionic Liquid for Lithium Batteries. *J. Power Sources* **2011**, *196* (4), 2264–2268.
(108) Lee, S. I.; Jung, U. H.; Kim, Y. S.; Kim, M. H.; Ahn, D. J.; Chun, H. S. A Study of Electrochemical Kinetics of Lithium Ion in Organic Electrolytes. *Korean J. Chem. Eng.* **2002**, *19* (4), 638–644.
(109) Doeff, M. M.; Edman, L.; Sloop, S. E.; Kerr, J.; De Jonghe, L. C. Transport Properties of Binary Salt Polymer Electrolytes. *J. Power Sources* **2000**, *89* (2), 227–231.
(110) Georén, P.; Lindbergh, G. Characterisation and Modelling of the Transport Properties in Lithium Battery Polymer Electrolytes. *Electrochim. Acta* **2001**, *47* (4), 577–587.
(111) Pesko, D. M.; Feng, Z.; Sawhney, S.; Newman, J.; Srinivasan, V.; Balsara, N. P. Comparing Cycling Characteristics of Symmetric Lithium-Polymer-Lithium Cells with Theoretical Predictions. *J. Electrochem. Soc.* **2018**, *165* (13), 3186–3194.
(112) Shah, D. B.; Nguyen, H. Q.; Grundy, L. S.; Olson, K. R.; Mecham, S. J.; Desimone, J. M.; Balsara, N. P. Difference between Approximate and Rigorously Measured Transference Numbers in Fluorinated Electrolytes. *Phys. Chem. Chem. Phys.* **2019**, *21* (15), 7857–7866.
(113) Maslyn, J. A.; Loo, W. S.; McEntush, K. D.; Oh, H. J.; Harry, K. J.; Parkinson, D. Y.; Balsara, N. P. Growth of Lithium Dendrites and Globules through a Solid Block

Copolymer Electrolyte as a Function of Current Density. *J. Phys. Chem. C* **2018**, *122* (47), 26797–26804.
(114) Barai, P.; Higa, K.; Srinivasan, V. Lithium Dendrite Growth Mechanisms in Polymer Electrolytes and Prevention Strategies. *Phys. Chem. Chem. Phys.* **2017**, *19* (31), 20493–20505.
(115) Bai, P.; Li, J.; Brushett, F. R.; Bazant, M. Z. Transition of Lithium Growth Mechanisms in Liquid Electrolytes. *Energy Environ. Sci.* **2016**, *9* (10), 3221–3229.
(116) Ellabban, O.; Abu-Rub, H.; Blaabjerg, F. Renewable Energy Resources: Current Status, Future Prospects and Their Enabling Technology. *Renew. Sustain. Energy Rev.* **2014**, *39*, 748–764.
(117) Yang, Z.; Liu, J.; Baskaran, S.; Imhoff, C. H.; Holladay, J. D. Enabling Renewable Energy-and the Future Grid-with Advanced Electricity Storage. *JOM* **2010**, *62* (9), 14–23.
(118) Su, W.; Eichi, H.; Zeng, W.; Chow, M. Y. A Survey on the Electrification of Transportation in a Smart Grid Environment. *IEEE Trans. Ind. Informat.* **2012**, *8* (1), 1–10.
(119) Xue, Z.; He, D.; Xie, X. Poly(Ethylene Oxide)-Based Electrolytes for Lithium-Ion Batteries. *J. Mater. Chem. A* **2015**, *3* (38), 19218–19253.
(120) Borodin, O.; Smith, G. D. Molecular Dynamics Simulations of Poly(Ethylene Oxide)/LiI Melts. 1. Structural and Conformational Properties. *Macromolecules* **1998**, *31* (23), 8396–8406.
(121) Shi, J.; Vincent, C. A. The Effect of Molecular Weight on Cation Mobility in Polymer Electrolytes. *Solid State Ion.* **1993**, *60* (1–3), 11–17.
(122) Perrier, M.; Besner, S.; Paquette, C.; Vallée, A.; Lascaud, S.; Prud'homme, J. Mixed-Alkali Effect and Short-Range Interactions in Amorphous Poly(Ethylene Oxide) Electrolytes. *Electrochim. Acta* **1995**, *40* (13–14), 2123–2129.
(123) Hayamizu, K.; Akiba, E.; Bando, T.; Aihara, Y. ^{1}H, ^{7}Li, and ^{19}F Nuclear Magnetic Resonance and Ionic Conductivity Studies for Liquid Electrolytes Composed of Glymes and Polyetheneglycol Dimethyl Ethers of $CH_3O(CH_2CH_2O)NCH_3$ (n = 3 - 50) Doped with $LiN(SO_2CF_3)_2$. *J. Chem. Phys.* **2002**, *117* (12), 5929–5939.
(124) Tobishima, S.; Morimoto, H.; Aoki, M.; Saito, Y.; Inose, T.; Fukumoto, T.; Kuryu, T. Glyme-Based Nonaqueous Electrolytes for Rechargeable Lithium Cells. *Electrochim. Acta* **2004**, *49* (6), 979–987.
(125) Hirayama, H.; Tachikawa, N.; Yoshii, K.; Watanabe, M.; Katayama, Y. Ionic Conductivity and Viscosity of Solvate Ionic Liquids Composed of Glymes and Excess Lithium Bis(Trifluoromethylsulfonyl)Amide. *Commun. Electrochem.* **2015**, *83* (10), 824–827.
(126) Capiglia, C.; Imanishi, N.; Takeda, Y.; Henderson, W. A.; Passerini, S. Poly(Ethylene Oxide) $LiN(SO_2CF_2CF_3)_2$ Polymer Electrolytes. *J. Electrochem. Soc.* **2003**, *150* (4), A525–A531.
(127) Armand, M. B. Polymer Electrolytes. *Annu. Rev. Mater. Sci.* **1986**, *16*, 246–261.
(128) Lightfoot, P.; Mehta, M. A.; Bruce, P. G. Crystal Structure of the Polymer Electrolyte Poly(Ethylene Oxide)$_3$:$LiCF_3SO_3$. *Science* **1993**, *262* (5135), 883–885.
(129) Fetters, L. J.; Lohse, D. J.; Milner, S. T.; Graessley, W. W. Packing Length Influence in Linear Polymer Melts on the Entanglement, Critical, and Reptation Molecular Weights. *Macromolecules* **1999**, *32* (20), 6847–6851.

(130) Jeon, D. H.; Baek, S. M. Thermal Modeling of Cylindrical Lithium Ion Battery during Discharge Cycle. *Energy Convers. Manag.* **2011**, *52* (8–9), 2973–2981.
(131) Shah, D.; Kim, H. K.; Nguyen, H. Q.; Srinivasan, V.; Balsara, N. P. Comparing Measurements of Limiting Current of Electrolytes with Theoretical Predictions up to the Solubility Limit. *J. Phys. Chem. C* **2019**, *123* (39), 23872–23881.
(132) Hiller, M. M.; Joost, M.; Gores, H. J.; Passerini, S.; Wiemhöfer, H. D. The Influence of Interface Polarization on the Determination of Lithium Transference Numbers of Salt in Polyethylene Oxide Electrolytes. *Electrochim. Acta* **2013**, *114*, 21–29.
(133) Craig, N.; Mullin, S. A.; Pratt, R.; Crane, G. B. Determination of Transference Number and Thermodynamic Factor by Use of Anion-Exchange Concentration Cells and Concentration Cells. *J. Electrochem. Soc.* **2019**, *166* (13), 2769–2775.
(134) Gribble, D. A.; Frenck, L.; Shah, D. B.; Maslyn, J. A.; Loo, W. S.; Mongcopa, K. I. S.; Pesko, D. M.; Balsara, N. P. Comparing Experimental Measurements of Limiting Current in Polymer Electrolytes with Theoretical Predictions. *J. Electrochem. Soc.* **2019**, *166* (14), A3228–A3234.
(135) Pan, X.; Liu, T.; Kautz, D. J.; Mu, L.; Tian, C.; Long, T. E.; Yang, P.; Lin, F. High-Performance N-Methyl-N-Propylpiperidinium Bis(Trifluoromethanesulfonyl)Imide/Poly(Vinylidene Fluoride-Hexafluoropropylene) Gel Polymer Electrolytes for Lithium Metal Batteries. *J. Power Sources* **2018**, *403*, 127–136.
(136) Richardson, P. M.; Voice, A. M.; Ward, I. M. Pulsed-Field Gradient NMR Self Diffusion and Ionic Conductivity Measurements for Liquid Electrolytes Containing $LiBF_4$ and Propylene Carbonate. *Electrochim. Acta* **2014**, *130*, 606–618.
(137) Ding, M. S.; Xu, K.; Zhang, S. S.; Amine, K.; Henriksen, G. L.; Jow, T. R. Change of Conductivity with Salt Content, Solvent Composition, and Temperature for Electrolytes of $LiPF_6$ in Ethylene Carbonate-Ethyl Methyl Carbonate. *J. Electrochem. Soc.* **2002**, *148* (10), A1196–A1204.
(138) Murmann, P.; Niehoff, P.; Schmitz, R.; Nowak, S.; Gores, H.; Ignatiev, N.; Sartori, P.; Winter, M.; Schmitz, R. Investigations on the Electrochemical Performance and Thermal Stability of Two New Lithium Electrolyte Salts in Comparison to $LiPF_6$. *Electrochim. Acta* **2013**, *114*, 658–666.
(139) Hou, T.; Monroe, C. W. Composition-Dependent Thermodynamic and Mass-Transport Characterisation of Lithium Hexafluorophosphate in Propylene Carbonate. *Electrochim. Acta* **2019**, *332*, 135085.
(140) Landesfeind, J.; Gasteiger, H. A. Temperature and Concentration Dependence of the Ionic Transport Properties of Lithium-Ion Battery Electrolytes. *J. Electrochem. Soc.* **2019**, *166* (14), A3079–A3097.
(141) Georén, P.; Lindbergh, G. Characterisation and Modelling of the Transport Properties in Lithium Battery Gel Electrolytes: Part I. The Binary Electrolyte PC/$LiClO_4$. *Electrochim. Acta* **2004**, *49* (21), 3497–3505.
(142) Lundgren, H.; Behm, M.; Lindbergh, G. Electrochemical Characterization and Temperature Dependency of Mass-Transport Properties of $LiPF_6$ in EC:DEC. *J. Electrochem. Soc.* **2015**, *162* (3), 413–420.
(143) Jeon, H.; Jin, S. Y.; Park, W. H.; Lee, H.; Kim, H. T.; Ryou, M. H.; Lee, Y. M. Plasma-Assisted Water-Based Al_2O_3 Ceramic Coating for Polyethylene-Based Microporous

Separators for Lithium Metal Secondary Batteries. *Electrochim. Acta* **2016**, *212*, 649–656.
(144) Jin, S. Y.; Manuel, J.; Zhao, X.; Park, W. H.; Ahn, J. H. Surface-Modified Polyethylene Separator via Oxygen Plasma Treatment for Lithium Ion Battery. *J. Ind. Eng. Chem.* **2017**, *45*, 15–21.
(145) Kondo, K.; Sano, M.; Hiwara, A.; Omi, T.; Fujita, M.; Kuwae, A.; Iida, M.; Mogi, K.; Yokoyama, H. Conductivity and Solvation of Li^+ Ions of $LiPF_6$ in Propylene Carbonate Solutions. *J. Phys. Chem. B* **2000**, *104* (20), 5040-5044.
(146) Nishida, T.; Nishikawa, K.; Fukunaka, Y. Diffusivity Measurement of $LiPF_6$, LiTFSI, $LiBF_4$ in PC. *ECS Trans.* **2008**, *6* (18), 1–14.
(147) Zugmann, S.; Fleischmann, M.; Amereller, M.; Gschwind, R. M.; Wiemhöfer, H. D.; Gores, H. J. Measurement of Transference Numbers for Lithium Ion Electrolytes via Four Different Methods, a Comparative Study. *Electrochim. Acta* **2011**, *56* (11), 3926–3933.
(148) Mauro, V.; D'Aprano, A.; Croce, F.; Salomon, M. Direct Determination of Transference Numbers of $LiClO_4$ Solutions in Propylene Carbonate and Acetonitrile. *J. Power Sources* **2005**, *141* (1), 167–170.
(149) Zhao, J.; Wang, L.; He, X.; Wan, C.; Jiang, C. Determination of Lithium-Ion Transference Numbers in $LiPF_6$-PC Solutions Based on Electrochemical Polarization and NMR Measurements. *J. Electrochem. Soc.* **2008**, *155* (4), 292–296.
(150) Galluzzo, M. D.; Maslyn, J. A.; Shah, D. B.; Balsara, N. P. Ohm's Law for Ion Conduction in Lithium and beyond-Lithium Battery Electrolytes. *J. Chem. Phys.* **2019**, *151* (2), 020901.
(151) Self, J.; Fong, K. D.; Persson, K. A. Transport in Superconcentrated $LiPF_6$ and $LiBF_4$ /Propylene Carbonate Electrolytes. *ACS Energy Lett.* **2019**, *4*, 2843–2849.
(152) Smith, J. W.; Lam, R. K.; Sheardy, A. T.; Shih, O.; Rizzuto, A. M.; Borodin, O.; Harris, S. J.; Prendergast, D.; Saykally, R. J. X-Ray Absorption Spectroscopy of $LiBF_4$ in Propylene Carbonate: A Model Lithium Ion Battery Electrolyte. *Phys. Chem. Chem. Phys.* **2014**, *16* (43), 23568–23575.
(153) Reddy, V. P.; Smart, M. C.; Chin, K. B.; Ratnakumar, B. V; Surampudi, S.; Hu, J.; Yan, P.; Prakash, G. K. S. ^{13}C NMR Spectroscopic, CV, and Conductivity Studies of Propylene Carbonate-Based Electrolytes Containing Various Lithium Salts. *Electrochem. Solid-State Lett.* **2005**, *8* (6), A294–A298.
(154) Timachova, K.; Newman, J.; Balsara, N. P. Theoretical Interpretation of Ion Velocities in Concentrated Electrolytes Measured by Electrophoretic NMR. *J. Electrochem. Soc.* **2019**, *166* (2), 264–267.
(155) Rosenwinkel, M. P.; Schönhoff, M. Lithium Transference Numbers in PEO/LiTFSA Electrolytes Determined by Electrophoretic NMR. *J. Electrochem. Soc.* **2019**, *166* (10), A1977–A1983.
(156) Dai, H.; Zawodzinski, Jr., T. A. Determination of Lithium Ion Transference Numbers by Electrophoretic Nuclear Magnetic Resonance. *J. Electrochem. Soc.* **1996**, *143* (6), L107–L109.
(157) Brinkkötter, M.; Giffin, G. A.; Moretti, A.; Jeong, S.; Passerini, S.; Schönhoff, M. Relevance of Ion Clusters for Li Transport at Elevated Salt Concentrations in [Pyr_{12O1}][FTFSI] Ionic Liquid-Based Electrolytes. *Chem. Commun.* **2018**, *54* (34), 4278–4281.

(158) Newman, J.; Chapman, T. W. Restricted Diffusion in Binary Solutions. *AIChE J.* **1973**, *19* (2), 343–348.
(159) Li, W.; Yao, H.; Yan, K.; Zheng, G.; Liang, Z.; Chiang, Y.; Cui, Y. The Synergetic Effect of Lithium Polysulfide and Lithium Nitrate to Prevent Lithium Dendrite Growth. *Nat. Commun.* **2015**, *6* (1), 7436.
(160) Weber, R.; Genovese, M.; Louli, A. J.; Hames, S.; Martin, C.; Hill, I. G.; Dahn, J. R. Long Cycle Life and Dendrite-Free Lithium Morphology in Anode-Free Lithium Pouch Cells Enabled by a Dual-Salt Liquid Electrolyte. *Nat. Energy*. **2019**, *4* (8), 683–689.

Appendix A – MATLAB Programs for Data Analysis

A.1 Steady-state current

This program allows for high throughput analysis of multiple ".txt" files from steady-state current measurements used to calculate the ideal transference number. The program will take two different file inputs. The first file must be a ".txt" file that is from an open circuit voltage (OCV) step in EC-lab; column 1 must be time, in seconds, and column 2 must be potential, in voltage. The second file must be from the chronoamperometry (CA) step, with column 1 being time, in seconds, column 2 as the applied potential, in units of voltage, and column 3 as current, in mA. There should be the same number of files selected between the OCV and CA files. The output of the program is a ".txt" file with 5 columns. Column 1 is the file name, column 2 is the OCV averaged over some time that is defined by the user, column 3 is the averaged applied potential on the lithium-symmetric cell by the potentiostat over the course of the measurement, column 4 is the initial current, and column 5 is the averaged steady-state current over some time as defined by the user. The user defined time should be the same for the OCV and steady-state current averages. Example output of the program is shown in Table A.1.

Table A.1: Example table output of the program.

File Name	OCV (mV)	EWE (mV)	I0 (mA)	Iss (mA)
Li-407_2_TfRD_5mV_08292019_02_OCV.txt	-0.075979	5.0208	0.010713	0.008053

The OCV files that are to be analyzed are imported using the line "[Filenames_OCV, filepath_OCV] = uigetfile({'*02_OCV*.txt; *08_OCV*.txt'}, 'Select OCV file(s): ','MultiSelect', 'on');" where the colored text acts as filters and should be adjusted based on the users' file naming convention. The steady-state current files that are to be analyzed are imported using line "Filenames_EWE = uigetfile({'*03_CA*.txt; *09_CA*.txt'}, 'Select CA file(s): ', 'MultiSelect', 'on');" and the colored text should be adjusted based on the users' naming convention. The main program calls the function file named "EWE". Both programs are below and the MATLAB color scheme was unchanged to help with readability.

Main program

```
%{
The goal of the program is to speed up data analysis on steady-state
current transference number measurements. Only for use on Li symmmetric
cell data. The program will output the average OCV after the last 5 minutes
during a rest step. It will also average EWE over the entire time of
measurement. And will pull out initial current and steady-state current,
averaged over 5 minutes choosen by user in EWE function file.
%}

clc
clear
close all
```

```
%Program for calculating OCV
%Files do not have to be in the same directory as this program, but do have
%to be in the same directory as one another
%Export EC-Lab files into text files without saving the header. Export time
%(s) and then EWE (V)

[Filenames_OCV, filepath_OCV]  = uigetfile({'*02_OCV*.txt; *08_OCV*.txt'}, 'Select OCV
file(s): ','MultiSelect', 'on');
addpath(filepath_OCV);

[OCV, I_OCV, iss_OCV] = EWE(Filenames_OCV, 300); %sending all filenames; sending time
= 300 s

%Turn OCV into mV
OCV = OCV*1000;

%Obtain average polarization, V. Export CA files in following order:
%time(s), EWE(V), and I(mA)
Filenames_EWE = uigetfile({'*03_CA*.txt; *09_CA*.txt'}, 'Select CA file(s): ', 'MultiSelect',
'on');
%returns average applied V, initial current and steady state current over last five minutes
[V, I_CA0, I_CAss] = EWE(Filenames_EWE, 1);
V = V*1000; %turn to mV units
%add data to text file
File = fopen('B33 VMP300 01-15-20.txt', 'wt');
OCVname = string(Filenames_OCV);
dat = [OCVname; OCV; V; I_CA0; I_CAss];
fprintf(File, 'File Name\tOCV (mV)\tEWE (mV)\tI0 (mA)\tIss (mA)\n');
fprintf(File, '%s\t%f\t%f\t%f\t%f\n', dat);
fclose(File);
```

Function EWE

```
function [ V, i0, iss ] = EWE( Names, time )
%{
Function serves to determine how many files were opened and how to handle
them for an average. It also allows you to determine how much time the
file should be averaged over.
%}
char_file = char(Names); %turns files into character files
j = size(char_file, 1); %determines size of first dimension, if single file selected, N = 1, else N =
length
if j == 1
   N = 1;
else
   N = length(Names);
```

```
end

%Calculate average OCV over last specificied 'time'
if N == 1
    A = dlmread(Names, '', 1, 0);
    s = length(A(:,1)); %cacluate time in file
    if time == 1
        start = 1;
        i0 = A(2,3); %return initial current
        iss = mean(A(s-300:s,3)); %Obtain Iss for t=15 to 20 min, 900:1200. If wanting last five
minutes, limits: s-300:s
        V = mean(A(start:s, 2)); %calculate applied V over first 20 min, start:1200. If want over all,
use limit start:s
    else
        start = s-time;
        i0 = 'DNE';
        iss = 'DNE';
        V = mean(A(start:s, 2)); %Calculate OCV over last five minutes
    end
   % V = mean(A(start:s, 2)); %calculate avg V over first 20 min. Otherwise
   % use limit start:s. Use this if using same limits for analysis, i.e.
   % over last five minutes for both OCV and V calculation
else
    V = zeros(1, N);
    for i=1:N
        File = char(Names(i));
        A = dlmread(File, '', 1, 0);
        s = length(A(:,1)); %determine amount of time in file
        if time == 1
            start = 1;
            i0(i) = A(2,3);
            iss(i) = mean(A(s-300:s,3)); %obtain Iss for each file for last five min
            V(i) = mean(A(start:s, 2)); %Obtain applied V for entire time
        else
            start = s-time; %average over the last 5 minutes
            i0 = 'DNE';
            iss = 'DNE';
            V(i) = mean(A(start:s, 2)); %average OCV over last five min
        end
        %V(i) = mean(A(start:s, 2)); %average V over the first 20 min
    end
end

end
```

A.2 Restricted diffusion

This program is used to expedite the calculation of the salt diffusion coefficient using the restricted diffusion method, as developed by Chapman and Newman and extended by Ma *et al.*[80,158] The parameter, "alpha," is adjustable within the program to better the electrolyte being studied. Traditionally, a value of 0.05 is used, as determined by Thompson and Newman.[92] However, values as low as 0.03 can be used for alpha and the salt concentration profiles should still be linear, so long as the applied dc polarization prior to the open circuit potential step was small. The program iteratively solves for the salt diffusion coefficient until the "alpha" criteria is met.

The file type fed into the code must be a ".txt" file. Column 1 should be time, in seconds, and column 2 should be the open circuit voltage (OCV), in units of voltage and the headline should not be exported from EC-Lab. "Sample_t" and "analysis_time" are both adjustable and dependent on the structure of the program as well as relaxation time for the electrolyte. The former is in units of seconds and the latter in minutes. The thickness of the electrolyte is stored in "L" and can be any sized 1D column vector, in units of mm, but it has to be the same number as the number of OCV files that will be studied. The OCV files that are to be analyzed are imported using the line "[Filenames_OCV, filepath_OCV]= uigetfile({'*06_OCV*.txt; *12_OCV*.txt'}, 'Select OCV file(s): ', 'MultiSelect', 'on');" where the colored text acts as filters and should be adjusted based on the users' file naming convention.

The output of the code will be in the form of a figure with the raw OCV data as well as an exponential fit, as shown in Fig. A.1. It will also output a ".txt" file using the line "File = fopen('05-27-2020.txt', 'wt');" where the colored text determines the name of the file.

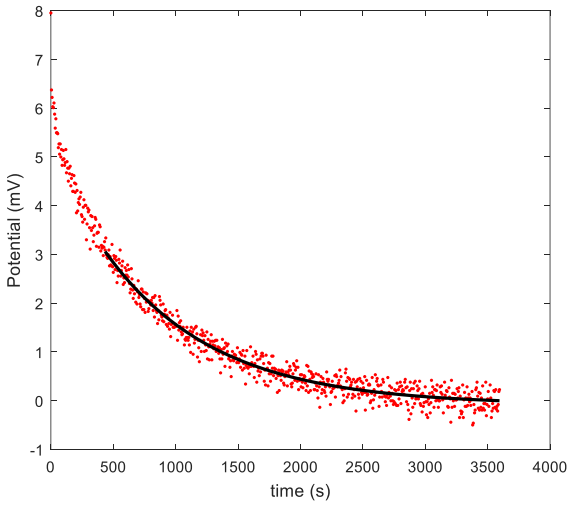

Figure A.1 Example of the program output. Raw OCV data with respect to time shown as red points and an exponential plus constant shown as the black curve.

Example of the ".txt" output file is shown below in Table A.2; the file name, salt diffusion coefficient, and the final alpha value are all outputted from the program.

Table A.2 Example table output of the program.

File Name	D (cm^2/s)	Alpha
HN-Li-49_2_TfandRD_40mV_040218_long_06_OCV_C01.txt	1.87E-08	0.050329

Below here is the raw code, and the MATLAB color scheme was left intact for readability.

Main program

```
%{
The goal of this program is to speed up data analysis for restricted
diffusion measurements. Only for use on Li symmetric cell data.

The program will take in OCV vs time data, plot and fit it to an
exponential plus constant model, eveluate the minimum time required and
then calculated the restricted diffusion coeff. EC-Lab data should be
exported as a text file without a header in order of time (s) and EWE (V).
%}

clc
clear
close all
%%

%{
sample_t is the sampling time for the OCV file in seconds

alpha is a non-dimensional diffusion coefficientand can be varied.
Typically use 0.05, based on work by Thompson and Newman.

L is an array meant to represent the thickness of the electrolyte used in
each file. In units of mm and later converted to cm.
%}

%Begin editing values
sample_t = 5; %sampling time for OCV, in seconds
alpha = 0.05; %define alpha value
analysis_time = 60; %number of minutes to study in each file

%L should be same size as number of OCV files selected
L = [
0.127
]'; %thickness of electrolyte in mm; keep as row column

%end changing values
%%
L = L/10; %convert mm to cm
```

```
analysis_t_index = ceil(analysis_time*60/sample_t); %convert analsysis time into an index
value. This is used to dictate how much of EWE vs. t is analyzed

%%
%{
This section allows the user to select N number of files from any folder
(all files selected must be in the same folder). The inputs within
uigetfile allow the user to add filters so that only files with specified
names show up.
%}

%Content in {} can be changed to reflect file names. It filters files based
%on the name shown in {}
[Filenames_OCV, filepath_OCV]= uigetfile({'*06_OCV*.txt; *12_OCV*.txt'}, 'Select OCV
file(s): ', 'MultiSelect', 'on');
addpath(filepath_OCV);

%%
%begin program to fit and analyze OCV relaxation
char_file = char(Filenames_OCV); %Turns files into character files
j = size(char_file, 1); %determines size of first dimension
%if single file selected, N = 1, else N = length
if j==1
   N = 1;
else
   N = length(Filenames_OCV);
   Diff = zeros(1,N);
   Alpha_f = zeros(1,N);
end

%%
%{
If only one file is selected, the program will go into this 'if' function.
The code reads the earlier selected file data and drops it into array Z.
The time vector is held in t = Z(:,1) in units of seconds; the EWE vector
is held in EWE = Z(:,2)*1000 in units of mV. The time is reset to 0 with t
= t - t(1). An exponential + constant fit is created and is fit to the
intial data. An initial diffusion coefficient, Diff_i, is calculated, which
is used to calculate the amount of time that should not be considered in
the fit, which is based on the set alpha value from earlier. This value is
t_min, and it returns an integer index value, which is then used as the
inequality in the while loop. Logic for the while loop:
As long as the time is less than t_min, the index counter n will increase
by 1, until it calculates a t_min that fulfills the alpha value.
Alternatively, can increase the index counter, n, by n = t_min + x, where x
is any integer value. This will analyze data faster, and is a good approach
```

```
for long relaxation times. The former is good if relaxation times on the
order of minutes rather than hours.
%}

%calculate D (cm^2/s) and alpha (dimensionless)

if N == 1
   Z = dlmread(Filenames_OCV, '', 1, 0);
   t = Z(:,1);

   t = t(1:analysis_t_index);
   t = t-t(1);

   %setting a counter for t in order to use in while loop
   n=1;
   EWE = Z(:,2)*1000; %units of mV
   EWE = EWE - sum(EWE(analysis_t_index-
36:analysis_t_index))/length(EWE(analysis_t_index-36:analysis_t_index)); %subtract out OCV
from last 3 minutes

   %Match range to be equal to t range
   EWE = EWE(1:analysis_t_index);

   %exponential + constant fit
   model = @(b, t) b(1).*exp(-b(2).*t(:))+b(3);
   initial = [0,0,0];

   %initial fit using above defined fittype from t(n) to end
   fi = fitnlm(t(1:end), EWE(1:end), model, initial);
   coeff = fi.Coefficients.Estimate; %returns column vector of fit coefficient values
   Diff_i = coeff(2)*L^2/pi()^2; %extract initial diffusion coefficient value
   t_min = ceil(alpha*L^2/Diff_i/sample_t); %calculate minimum number in time index for fit
rounded up

   %while loop to do fits until the values fit are at time greater than
   %t_min

   while(t(n)<=t(t_min))
      n=n+1; %increase index counter by 1 in t
      t_new = t(n:end)-t(n); %determine new time vector to do fit
      EWE_new = EWE(n:end);
      f_n = fitnlm(t_new, EWE(n:end), model, initial);
      coeff_n = f_n.Coefficients.Estimate;
      Diff_n = coeff_n(2)*L^2/pi()^2;
      t_min = ceil(alpha*L^2/Diff_n/sample_t);
      alpha_n = Diff_n*t(n)/L^2;
```

```
    end

    Diff = Diff_n;
    Alpha_f = alpha_n;
    %make x and y vector of fit
    f_n_x = linspace(t_new(1), t_new(end), 1000);
    f_n_y = model(coeff_n, f_n_x);
    figure
    plot(t, EWE, '.r', f_n_x+t(n), f_n_y, '-k', 'LineWidth', 2)
    xlabel('time (s)')
    ylabel('Potential (mV)')

%%
%Same as above, but for all files selected, from 1 to N, as well as 1 to
%length(L)

else
    for i = 1:N
        File = char(Filenames_OCV(i));
        Z = dlmread(File, '', 1, 0);

        t = Z(:,1);
        t = t(1:analysis_t_index);
        t = t-t(1); %start time at zero

        n=1; %setting a counter for t in order to use in while loop

        EWE = Z(:,2)*1000; %units of mV
        EWE = EWE - sum(EWE(analysis_t_index-
36:analysis_t_index))/length(EWE(analysis_t_index-36:analysis_t_index)); %subtract out
average OCV from last 3 minutes
        EWE = EWE(1:analysis_t_index);

        model = @(b, t) b(1).*exp(-b(2).*t(:))+b(3); %exponential + constant fit
        initial = [0,0,0];
        fi = fitnlm(t(1:end), EWE(1:end), model, initial); %initial fit using above defined fittype
from t(n) to end
        coeff = fi.Coefficients.Estimate; %returns column vector of fit coefficient values
        Diff_i = coeff(2)*L(i)^2/pi()^2; %extract initial diffusion coefficient value
        t_min = ceil(alpha*L(i)^2/Diff_i/sample_t); %calculate minimum number in time index for
fit rounded up

        %while loop to do fits until the values fit are at time greater than
        %t_min
        while(t(n)<=t(t_min))
            n=n+1; %increase index value by 1
```

```
        t_new = t(n:end)-t(n); %determine new time vector to do fit
        EWE_new = EWE(n:end);
        f_n = fitnlm(t_new, EWE(n:end), model, initial);
        coeff_n = f_n.Coefficients.Estimate;
        Diff_n = coeff_n(2)*L(i)^2/pi()^2;
        t_min = ceil(alpha*L(i)^2/Diff_n/sample_t);
        alpha_n = Diff_n*t(n)/L(i)^2;
    end

    Diff(i) = Diff_n;
    Alpha_f(i) = alpha_n;
    %make x and y vector of fit
    f_n_x = linspace(t_new(1), t_new(end), 1000);
    f_n_y = model(coeff_n, f_n_x);
    figure
    plot(t, EWE, '.r', f_n_x+t(n), f_n_y, '-k', 'LineWidth', 2)
    xlabel('time (s)')
    ylabel('Potential (mV)')
  end
end
%%
%{
Write data to file. Will record, in columns, the file name, final diffusion
coefficient, and final alpha value.
%}
File = fopen('05-27-2020.txt', 'wt'); %Name file
OCVname = string(Filenames_OCV);
dat = [OCVname; Diff; Alpha_f];
fprintf(File, 'File Name\tD (cm^2/s)\tAlpha\n');
fprintf(File, '%s\t%E\t%f\n', dat);
fclose(File);

%below code is for plotting fits of above data
%{
File1 = fopen('EC-40 fit.txt', 'wt'); %name file
dat1 = [f_n_x+t(n); f_n_y'];
fprintf(File1, 't(s)\tOCV fit(mV)\n');
fprintf(File1, '%f\t%f\n', dat1);
%}
```

A.3 Modeling salt concentration and potential profiles in electrolytes

This program allows for the calculation of the steady-state salt concentration and potential profiles for a given applied current density. The values “i_ss” and “L” can be adjusted to the user’s needs. The average salt concentration, shown as “m_av,” in the code, are the starting salt

concentrations of the electrolytes that the user wants to study. The lower limit of the salt concentrations studied should be inputted into "m_model," and in this model's case, the lower limit was 0.28 mo/kg. If the user's lower limit is different from 0.28 mol/kg, it should also be changed within the "pos_conc_array_PFPE" and "calc_mav_PFPE" function files. The program calls upon multiple function files which should all be stored in the same directory. The function "eval_x_PFPE" is the curve of best fit for concentration shown in Fig. 4.2 and Eq. 4.9. The function "eval_phi_PFPE" is the curve of best fit for potential shown in Fig. 4.8 and Eq. 4.12. Parameters for both functions should be edited to match the electrolyte that is being modeled.

The program's output is a ".txt" file for each "m_av" with three columns. Column 1 is the normalized distance between the anode and cathode, column 2 is the predicted salt concentration at each position in units of mol/kg, and column 3 is the predicted electrolyte potential at each position in units of mV. The program will also output two figures with the predicted concentration and potential profiles. Below are the programs with the MATLAB default color scheme left intact for readability.

Main program

```
clear
clc
close all

%{
Use of this program is to calculate the concentration of salt in a Li symmetric cell using
fully characterized electrolytes
%}

%%
%defining constants
L = 0.00254; %cm; thickness of separator

%%
%Experimental values
i_ss = 0.8/1000; %In units of A/cm2
m_av = [0.60, 0.94, 1.30, 1.78]; %0.28 s the lowest molality, so we can't model that value

%%
%find upper bound at x/L = 0 for concentration
j = 1; %Initialize counter for legendinfo
for i=1:length(m_av)
   m_model = linspace(m_av(end), 0.28, 10000); %create vector of 10000 points between
m=1.78 to m=0.28

   m_theo_avg = 0.000; %initialize m_theo_avg

   k = 1; %counter for while loop
```

```
   while round(m_theo_avg, 3) ~= round(m_av(i), 3) && m_theo_avg ~=-1 %keep going
through while loop until r_av_model = r_av_real or until the program realizes it can't be solved
      m_theo_avg = calc_mav_PFPE(m_model(k), i_ss, L);
      k = k+1;
      if k > length(m_model)
         m_theo_avg =-1; %stop the while loop if the counter increases beyond the bounds given,
ensures that program stays within known values
      end
   end

   %%
   %determine x/L and r vectors
   if m_theo_avg ~=-1

      m0 = m_model(k-1); %Concentration at x/L = 0
      %Feed function m0, have it calculate all x values, remove x values
      %greater than L

      [x_L, m] = pos_conc_array_PFPE(m0, i_ss, L );
      phi = phi_conc_array_PFPE( m(end), m(1), length(m)); %calculate potential at all points
and pass size of x_L to ensure phi same size
      hold on
      subplot(1,2,1)
      plot(x_L, m)
      axis([0 1 0 2.1])
      xlabel('x/L')
      ylabel('m (mol Li/kg)')
      legendinfo{j} = ['m_a_v = ' num2str(m_av(i))];
      j = j+1;
      hold on
      subplot(1,2,2)
      plot(x_L, phi)
      axis([0 1 0 350])
      xlabel('x/L')
      ylabel('phi (mV)')


      %write each solution to text file
      file = fopen(sprintf('i_ss = %.2fmA_cm2, m_av = %.3f, L = %.4f.txt', i_ss*1000, m_av(i),
L), 'wt');
      dat = [x_L; m; phi];
      fprintf(file, 'i_ss = %.2f mA/cm2\tm_av = %.3f\n', i_ss*1000, m_av(i));
      fprintf(file, 'x/L\tm(x/L)(mol Li/kg)\tphi(x/L)(mV)\n');
      fprintf(file, '%.5f\t%.5f\t%.5f\n', dat);
      fclose(file);
   end
```

```
end
i_ssL{:} = ['i_s_sL = ' num2str(round(i_ss*1000*L, 2, 'significant')) ' mA/cm']; %string that will
write i_ss*L to the plot
legend(legendinfo)
subplot(1,2,1)
text(0.1, 2, i_ssL)
```

Function calc_mav_PFPE

```
function [ m_theo_av ] = calc_mav_PFPE( upper, i_ss, L )
%Use of this function to calculate the upper bound of m
%   This function will call eval_x_PFPE and solve for x and will keep
%   solving until m_av_real = m_av_theoretical

m_model = linspace(upper, 0.28, 1000);



x = eval_x_PFPE(i_ss, m_model) - eval_x_PFPE(i_ss, upper); %calculate all x positional values

N = length(x);

for i=1:N
   if x(i)/L <= 1
      m_model(i)= m_model(i);
   elseif x(i)/L > 1
      m_model(i)=0;
   end
end
%concoctinate matrix to number of non-zero elements for m_model and reduce
%size of both m_model and x to that size
n0 = nnz(m_model);
x = x(1:n0);
m_model = m_model(1:n0);

m_theo_av = trapz(x, m_model)/L; %calculate theoretical average m
end
```

Function eval_x_PFPE

```
function [ x ] = eval_x_PFPE(i_ss, m0)
%solve for x for PEO5K
%   values for polynomial expression for C8-DMC/LiFSI
%   Values below were determined after properly evaluating phi
F = 96485; %C/mol


a = 1.850E-11;
```

```
b = -8.565E-11;
c = 1.387E-10;
d = -9.717E-11;
e = 4.358E-11;

x = -F/i_ss*(a/5*m0.^5+b/4*m0.^4+c/3*m0.^3+d/2*m0.^2+e*m0);

end
```

Function eval_phi_PFPE

```
function [ phi ] = eval_phi_PFPE( m )
%Calculate potential drop for one m or multiple m
%   returns values in V
F = 96485; %C/mol

%{
Below are the bulk values to calculate phi
A1 = 4.1073E-5;
A2 = 1.1030E-6;
tau_1 = -8.2333;
tau_2 = 0.0557;
%}
%separator values to calc phi using a double exponential
A1 = 1.8019E-6;
A2 = 8.5662E-5;
tau_1 = 0.15413;
tau_2 = -8.5246;
phi = F.*(A1/tau_1.*exp(tau_1.*m) + A2/tau_2.*exp(tau_2.*m));

end
```

Function pos_conc_arry_PFPE

```
function [ x, m ] = pos_conc_array_PFPE( upper, i_ss, L )
%This function will provide the postional and concentration vectors
%   Feed this function the already calculated upper bound for
%   concentration, the set value for the steady state current, and the
%   thickness. The program will then call eval_x_PEO to determine all
%   values of x

m_model = linspace(upper, 0.28, 10000);

x_all = eval_x_PFPE(i_ss, m_model) - eval_x_PFPE(i_ss, upper); %calculate all x positional
values

for i=1:length(x_all)
    if x_all(i)/L < 1
```

```
        x(i) = x_all(i)/L;
        m(i) = m_model(i);
    end
end
x;
m;
end
```

Function phi_conc_array_PFPE

```
function [ phi_all ] = phi_conc_array_PFPE( mL, m0, differential)
%Determines the potential drop in electrolyte between x/L = 1 and x/L = 0
%   returns in mV

m_model = linspace(m0, mL, differential);

phi_all = (eval_phi_PFPE(m_model)-eval_phi_PFPE(mL))*1000; %return units in mV, should
evaluate phi from x/L = 0 to x/L = 1
end
```

A.4 Predicting limiting currents in electrolytes

This program is used to predict limiting currents within electrolytes. The program operates very similarly to that shown in section A.3, and calls many of the same functions. This program will predict the concentration profile of a specific electrolyte at varying current densities. The thickness, "L," the steady-state current density, "i_ss," and the average electrolyte concentration, "m_av," can all be changed to the necessary values. Once the program predicts the concentration profiles at differing values of "i_ss," the concentration at the anode side ("x_L" = 0) and the concentration at the cathode side ("x_L" = 1) are placed into an array as a function of "i_ss." These values are then plotted on a single graph with the normalized limiting current density, $i_{ss}L$, on the x-axis and m on the y-axis. These values are also outputted into a ".txt" file and a polynomial fit can be used to predict the limiting current due to cation depletion on the anode or solubility constraints on the cathode. This analysis procedure is outlined in chapter 4.

Main program

```
clear
clc
close all

%{
Use of this program is to approximate the limiting current of C8-DMC/LiFSI
%}

%%
%defining constants
L = 0.00254; %cm; thickness of separator
```

```
%%
%Experimental values
i_ss = linspace(0.01, 1, 50)/1000; %In units of A/cm2
m_av = 0.88; %values possible for m_av: (0.28, 1.78)(bound by those two values)

%%
%find upper bound at x/L = 0 for concentration
j = 1; %Initialize counter for legendinfo for x/L = 1
k = 1; %initialize counter for legendinfo for x/L = 0
for i=1:length(i_ss)
   m_model = linspace(1.78, 0.28, 1000); %create vector of 1000 points between m_av=1.78 to
m_av=0.28

   m_theo_avg = 0.000; %initialize r_theo_avg

   k = 1; %counter for while loop
   while round(m_theo_avg, 3) ~= round(m_av,3) && m_theo_avg ~=-1 %keep going through
while loop until r_av_model = r_av_real or until the program realizes it can't be solved
      m_theo_avg = calc_mav_PFPE(m_model(k), i_ss(i), L);
      k = k+1;
      if k > length(m_model)
         m_theo_avg =-1; %stop the while loop if the counter increases beyond the bounds given,
ensures that program stays within known values
      end
   end

   %%
   %determine x/L and r vectors
   if m_theo_avg ~=-1

      m0 = m_model(k-1); %Concentration at x/L = 0
      %Feed function r0, have it calculate all x values, remove x values
      %greater than L

      [x_L, m] = pos_conc_array_PFPE(m0, i_ss(i), L );
      if m(end)>= 0.280
         m_L(j) = m(end);
         i_ssL(j) = i_ss(i)*1000*L; %convert to mA/cm
         m_x0(j) = m0;
         j = j+1;
      end
    end

end
file = fopen(sprintf('limiting current, m_av = %.3f, L = %.4f.txt', m_av, L), 'wt');
```

```
dat = [m_L; m_x0; i_ssL];
fprintf(file, 'm_av = %.3f\n', m_av);
fprintf(file, 'm_L (at x/L = 1)\tm_x0 (at x/L = 0)\ti_ss*L\n');
fprintf(file, '%.5f\t%.5f\t%.5f\n', dat);
fclose(file);
plot(i_ssL, m_L, 'o', i_ssL, m_x0, 'd')
xlabel('i_s_sL(mA/cm)')
ylabel('m (mol/kg)')
legend('@ x/L = 1', '@x/L = 0', 'Location', 'best')
```

Appendix B – Dual Salts in Propylene Carbonate

Multicomponent electrolyte mixtures (greater than 3 components) are often utilized in the hopes that they can improve upon battery performance.[4,137,159,160] However, as the number of components, *n*, increases, more transport parameters are required to fully model electrolyte behavior. Onsager reciprocal relations tell us that we require $n(n-1)/2$ properties, and these can take the place of Stefan-Maxwell diffusion coefficients.[38,39] For a system comprised of 4 components, 6 different Stefan-Maxwell diffusion coefficients are required, but are experimentally hard to measure.

Herein, we systematically study the effect of two lithium salts, lithium bis(fluorosulfonyl)imide (LiFSI) and lithium hexafluorophosphate ($LiPF_6$), dissolved in propylene carbonate (PC) as a function of salt concentration and salt molar ratios (n = 4). The solvent and salt structures are shown in Fig. B.1. We study ion transport properties as a function of salt concentrations ranging from 0.25 M to 2.00 M and LiFSI:$LiPF_6$ molar ratios of 25:75, 50:50, and 75:25. In Tables B.1, B.2, and B.3, we list the salt wt%, average molality, m_{av}, and average salt concentration, c_{av}, of the electrolytes that were studied for molar LiFSI:$LiPF_6$ ratios of 25:75, 50:50, and 75:25, respectively.

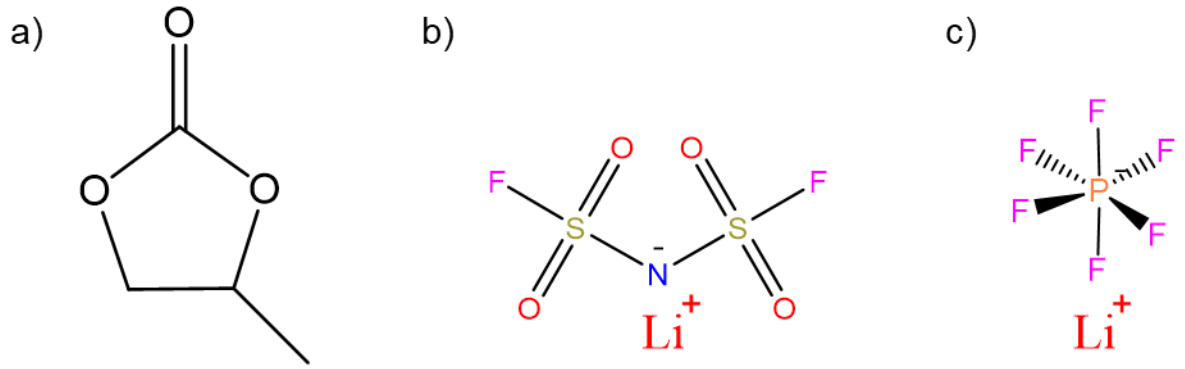

Figure B.1 a) PC, b) LiFSI, and c) $LiPF_6$

Table B.1 Values of salt wt%, molality, and calculated concentration for electrolytes of PC mixed with a 25:75 molar ratio of LiFSI:$LiPF_6$.

Salt wt% (25:75)	m_{av} (mol/kg)	c_{av} (mol/L)
3.38	0.21	0.25
6.42	0.43	0.50
12.33	0.65	0.75
13.32	0.87	1.00
15.11	1.11	1.25
17.85	1.35	1.50
23.03	1.86	2.00

Table B.2 Values of salt wt%, molality, and calculated concentration for electrolytes of PC mixed with a 50:50 molar ratio of LiFSI:$LiPF_6$.

Salt wt% (50:50)	m_{av} (mol/kg)	c_{av} (mol/L)
3.46	0.21	0.25
6.77	0.43	0.50
9.95	0.65	0.75
13.02	0.88	1.00
15.98	1.12	1.25
18.84	1.37	1.50
24.32	1.90	2.00

Table B.3 Values of salt wt%, molality, and calculated concentration for electrolytes of PC mixed with a 75:25 molar ratio of LiFSI:$LiPF_6$.

Salt wt% (75:25)	m_{av} (mol/kg)	c_{av} (mol/L)
3.66	0.21	0.25
7.18	0.43	0.50
10.55	0.66	0.75
13.80	0.90	1.00
16.95	1.14	1.25
19.98	1.40	1.50
25.80	1.95	2.00

The density, ρ, for select salt concentrations was obtained by filling a differential scanning calorimetry (DSC) sample pan (TA Instruments) with a known volume of 40 uL and measuring the mass of the electrolyte at room temperature inside an argon filled glovebox. The density was interpolated for unmeasured electrolytes using a curve of best fit, as shown in Figs. B.2a, B.2b, and B.2c for LiFSI:$LiPF_6$ molar ratio mixtures of 25:75, 50:50, and 75:25 in PC, respectively. The density was used to calculate c_{av} for a given salt wt%.

The conductivity, κ, salt diffusion coefficient, D, ideal transference number, $t_{+,id}$, and open circuit potential via concentration cells, U, were measured following the experimental procedure detailed in Chapter 6 of this dissertation and were measured at room temperature. All four measurements are shown in Fig. B.3 as a function of salt concentration and for three molar salt compositions of LiFSI:$LiPF_6$ of 25:75 (red), 50:50 (blue), 75:25 (green). In Fig. B.3a, κ is plotted as a function of c_{av}, where the symbols represent experimental data, and the solid curves are best-fit polynomials whose functions are shown in Table B.4. In general, the conductivity increases with increasing salt concentration, reaches a maximum at c_{av} = 1 M, and decreases at

higher salt concentration. Conductivity is mostly independent of the molar ratio of LiFSI:$LiPF_6$. Fig. B.3b is the salt diffusion coefficient as a function of c_{av}, and we find that D is mostly independent of salt concentration and the molar ratio of LiFSI:$LiPF_6$. The ideal transference number, $t_{+,id}$, is plotted as a function of c_{av} in Fig. B.3c. For molar salt ratios of 25:75 and 50:50, we observe a general decrease in $t_{+,id}$ with increasing salt concentration, a shallow minimum at c_{av} = 0.75M, which is followed by an increase at higher salt concentrations. For electrolytes with molar ratios of LiFSI:$LiPF_6$ of 50:50, the behavior is more complex, where $t_{+,id}$ increases, decreases and increases again with increasing salt concentration. In Fig. B.3d, the open circuit potential, U, as measured by concentration cells, is plotted as a function of the natural log of molality. The open circuit potential is equal to zero when both sides of the U-cell are filled with the reference electrolyte. The reference electrolyte concentrations had the same molar salt ratios as the electrolyte they were being used to study, and were m_{ref} = 0.87, 0.88, and 0.90, for molar salt ratios of 25:75, 50:50, and 75:25, respectively. With increasing m_{av}, U decreases for all three molar salt ratios, and U is quantitatively similar at a given salt concentration for each molar ratio studied. The solid curves are best-fit polynomials whose functions are shown in Table B.5.

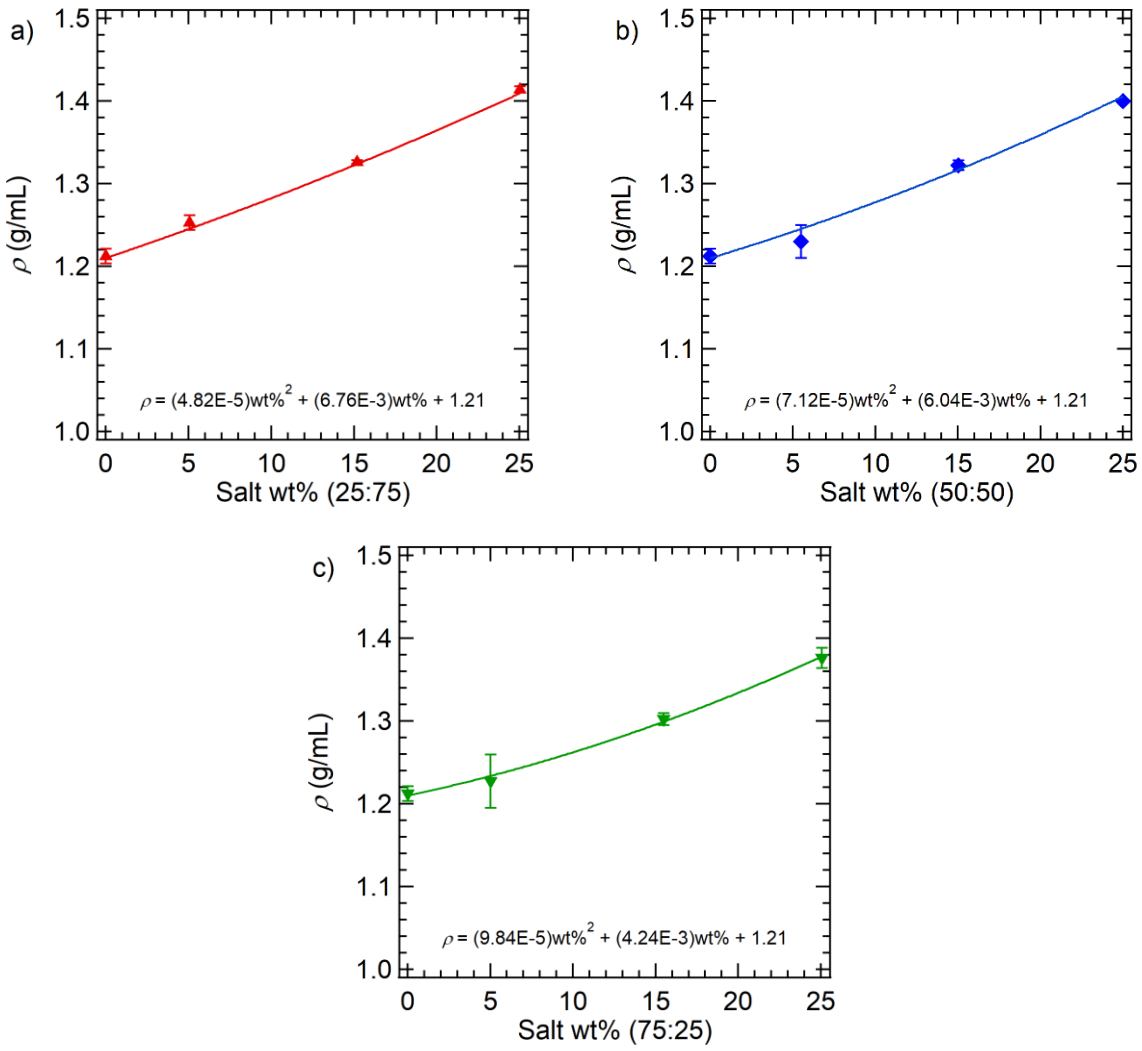

Figure B.2 Density as a function of salt wt% for LiFSI:$LiPF_6$ molar ratios of a) 25:75, b) 50:50, and c) 75:25 for select electrolytes. The solid curves represent curves of best fit to interpolate missing electrolyte densities.

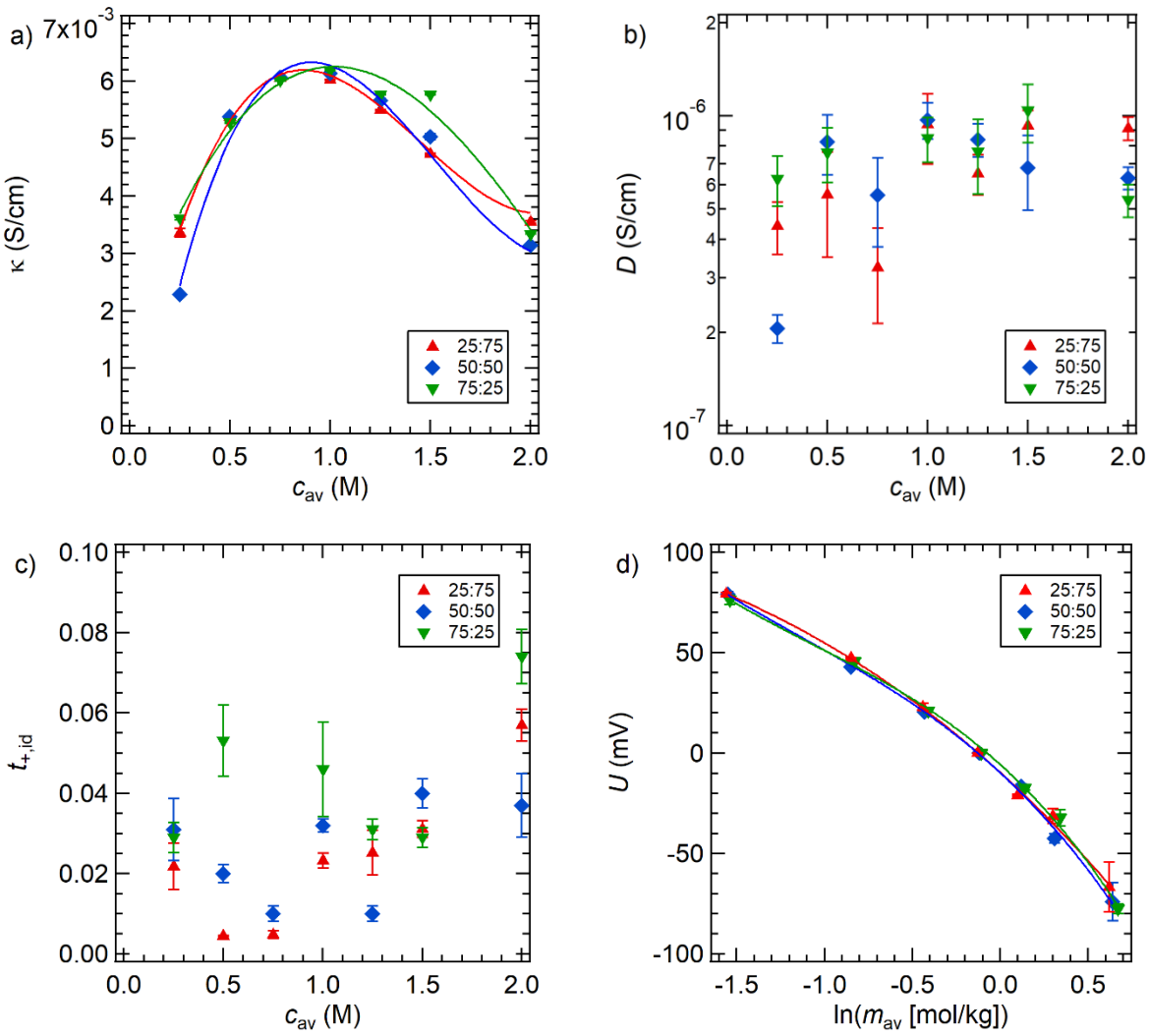

Figure B.3 Electrochemical properties of the electrolytic phase of LiFSI:$LiPF_6$/PC. Molar salt ratios of 25:75, 50:50, and 75:25 were used for LiFSI:$LiPF_6$. a) Conductivity as measured using a conductivity probe as a function of c_{av}. The solid curves are polynomial fits, which are shown in Table B.4. b) Salt diffusion coefficient measured using the restricted diffusion method as a function of c_{av} and c) ideal transference number as measured by the steady-state current method all as a function of c_{av}. d) Open circuit potential obtained using concentration cells with $m_{av,ref}$ = 0.87 mol/kg for 25:75 mixtures, $m_{av,ref}$ = 0.88 mol/kg for 50:50 mixtures, and $m_{av,ref}$ = 0.90 mol/kg for 75:25 mixtures as a function of the natural log of average molality. The solid, red, blue, and green curves are fits through the data for electrolytes with salt molar ratios of 25:75, 50:50, and 75:25 and the functions are shown in Table B.5.

Table B.4 Best-fit polynomial equations for conductivity for molar ratios of LiFSI:$LiPF_6$/PC mixtures at room temperature as a function of molar salt concentration, c.

$\kappa\ (\mathrm{LiFSI:LiPF_6}) = k_0 + k_1 c + k_2 c^2 + k_3 c^3$				
κ (LiFSI:$LiPF_6$)	k_0	k_1	k_2	k_3
κ (25:75)	6.92 x 10^{-5}	1.65 x 10^{-2}	-1.36 x 10^{-2}	3.13 x 10^{-3}
κ (50:50)	-1.84 x 10^{-3}	2.10 x 10^{-2}	-1.65 x 10^{-2}	3.61 x 10^{-3}
κ (75:25)	1.56 x 10^{-3}	1.00 x 10^{-2}	-6.08 x 10^{-3}	7.71 x 10^{-4}

Table B.5 Best-fit polynomial equations for the open circuit potential for molar ratios of LiFSI:$LiPF_6$/PC mixtures at room temperature as a function of molality, m.

$U\ (\mathrm{LiFSI:LiPF_6}) = a_0 + a_1 \ln(m) + a_2 \ln(m)^2 + a_3 \ln(m)^3$				
U (LiFSI:$LiPF_6$)	a_0	a_1	a_2	a_3
U (25:75)	-9.665	-79.68	-16.23	-1.145
U (50:50)	-9.795	-80.95	-28.15	-8.274
U (75:25)	-5.684	-79.12	-32.42	-10.18

Further work is needed to determine the six Stefan-Maxwell diffusion coefficients that would be required to predict behavior in these electrolytes. However, future work should also focus on measuring the electrolyte potential drop within lithium symmetric cells as a function of salt concentration, molar salt ratios, and current density. These experimental results should be compared to results given by Newman's concentrated solution theory, but simplified with the assumption that the ternary mixtures can be treated as binary mixtures.